Edge Artificial Intelligence for Real-Time Target Monitoring

Università di Genova

Ammar Mohanna

DITEN - Department of Electrical, Electronics and Telecommunication Engineering and Naval Architecture

University of Genova, Italy

Supervisor

Prof. Maurizio Valle

A thesis presented for the degree of Doctor of Philosophy

February 16, 2023

إِنَما يَخْشَى الله مِنْ عِبَادِهِ الْعُلَمَاءُ

It's those who have knowledge among **Allah (S.W.T)** worshippers, that truly fear Him

- Al-Quran, Surah Fatir (Verse 14)

I hereby declare that the work I have submitted is entirely original to me, and that, to the best of my knowledge and belief, it does not contain any passages that have been previously published or written by someone else, nor does it contain passages that have been largely approved for the award of any other degree or diploma from the University or another institution of higher learning, with the exception of those instances where appropriate citation has been made in the text.

Ammar Mohanna

February 16, 2023

Abstract

The key enabling technology for the exponentially growing cellular communications sector is location-based services. The need for location-aware services has increased along with the number of wireless and mobile devices. Estimation problems, and particularly parameter estimation, have drawn a lot of interest because of its relevance and engineers' ongoing need for higher performance. As applications expanded, a lot of interest was generated in the accurate assessment of temporal and spatial properties.

In the thesis, two different approaches to subject monitoring are thoroughly addressed. For military applications, medical tracking, industrial workers, and providing location-based services to the mobile user community, which is always growing, this kind of activity is crucial.

In-depth consideration is given to the viability of applying the Angle of Arrival (AoA) and Receiver Signal Strength Indication (RSSI) localization algorithms in real-world situations. We presented two prospective systems, discussed them, and presented specific assessments and tests. These systems were put to the test in diverse contexts (e.g., indoor, outdoor, in water...). The findings showed the localization capability, but because of the low-cost antenna we employed, this method is only practical up to a distance of roughly 150 meters. Consequently, depending on the use-case, this method may

or may not be advantageous. An estimation algorithm that enhances the performance of the AoA technique was implemented on an edge device.

Another approach was also considered. Radar sensors have shown to be durable in inclement weather and bad lighting conditions. Frequency Modulated Continuous Wave (FMCW) radars are the most frequently employed among the several sorts of radar technologies for these kinds of applications. Actually, this is because they are low-cost and can simultaneously provide range and Doppler data. In comparison to pulse and Ultra Wide Band (UWB) radar sensors, they also need a lower sample rate and a lower peak to average ratio. The system employs a cutting-edge surveillance method based on widely available FMCW radar technology. The data processing approach is built on an ad hoc-chain of different blocks that transforms data, extract features, and make a classification decision before cancelling clutters and leakage using a frame subtraction technique, applying DL algorithms to Range-Doppler (RD) maps, and adding a peak to cluster assignment step before tracking targets. In conclusion, the FMCW radar and DL technique for the RD maps performed well together for indoor use-cases. The aforementioned tests used an edge device and Infineon Technologies' Position2Go FMCW radar tool-set.

Acknowledgements

In the Name of **Allah (S.W.T)**, the Most Merciful, the Most Compassionate. All praises belongs to Almighty **Allah (S.W.T)**, the Lord of the worlds. Prayers and peace be upon Muhammad His servant and messenger.

First and foremost, I must acknowledge my limitless thanks to **Allah (S.W.T)**, the Ever-magnificent, the Ever-Thankful, for His help and bless by giving me the opportunity, courage, health and enough energy to carry out and complete the entire thesis work.

Secondly, I would like to thank my direct supervisor Prof. Maurizio Valle for his extensive assistance and support over the last three years. Thank you for the quick chats, the long discussions, and for always being there when I needed an extra hand. He encouraged me to trust my own judgement and make independent decisions, whilst always leaving his doors open.

In addition I would also like to extend my gratitude to the industrial colleagues from MYWAI S.R.L and especially Mr. Fabrizio Cardinali for his excellent help and support throughout the project.

Moreover, I extend my gratitude to all the members of the COSMIC laboratory for being there for me whenever I needed consultations and support.

Finally, without the loving support from my wife, my sisters and the strong educational roots planted decades ago by my parents, my grandparents and my teachers, I could not have completed this work.

Preface

- The following is the publication status of the chapters presented in this thesis;
  - The content of Chapter 3.5 have been published in Springer - Sensors and Microsystems Proceedings of AISEM 2021 (Italian National Conference of Sensors and Microsystems)
  - The content of Chapter 3.6 have been published in the 28th IEEE International Conference on Electronics, Circuits, and Systems ICECS 2021
  - The content of Chapter 4.4 have been published in MDPI - Sensors journal 2021
  - The content of Chapter 4.5 have been submitted to IEEE Transactions on Industrial Informatics journal 2022
- The work presented in this thesis was funded by;
  - Research grant (Assegno di ricerca) from the Liguria region under the SCOONER project, in collabortation with the industrial advisor Knowhedge S.R.L. The grant was titled “Development of an intelligent management system for shipwrecks at sea through the integration of IoT, Machine learning, artificial intelligence and Edge computing on board ship and at sea”. The grant’s duration was two years starting September 2019 and ended in September 2021.

– Research grant (Assegno di ricerca) from the university of Genova. The grant was titled: “Prognostic Maintenance of Industrial and Medical Machinery using Artificial Neural Networks on Chip DLT networks and IoT sensors on Edge computing devices”, the duration of this grant was from November 2021 till August 2022. This grant was in the scientific-disciplinary sector ING-INF/01 ELETTRONICA at the DIME department.

Contents

List of Figures

List of Tables

Nomenclature

AoA Angle of Arrival

BLE Bluetooth Low Energy

CNN Convolutional Neural Networks

DB DataBase

DF Direction finding

DL Deep Learning

DNN Deep Neural Network

DoA Direction of Arrival

DSP Digital Signal Processing

EPR Energy Precision Ratio

FMCW Frequency-Modulated Continuous-Wave

FoV Field of View

GNSS Global Navigation Satellite Systems

GPS Global Positioning System

IoT Internet of Things

LIDAR Light Detection and Ranging

LoS Line of Sight

LWIR Long-Wave Infrared

MCU MicroController Unit

MEMS Micro-electromechanical systems

ML Machine Learning

PRT Pulse Repetition Time

RD Range Doppler

RF Radio Frequency

RTLS Real-Time Localization Services

STFT Short-Time Fourier Transform

ToA Time of Arrival

UCA Uniform Circular Array

ULA Uniform Linear Array

UWB Ultra-Wide Band

UWB Ultra-Wide Bandwidth

WLAN Wireless Local Area Network

WSN Wireless Sensor Network

Chapter 1

Introduction

Location-based services are the primary enabling technology in the wireless communications industry, which is expanding at an exponential rate. From short-range Bluetooth and ad-hoc to long-range telecom networks, location-based services (LBS) are available. In a broad sense, location-based services are thought to give users of the services the most basic information about their whereabouts by exploiting the location of wireless devices within the network. The latter is the most important factor for the device's unique identification.

As the number of mobile and wireless devices has expanded, so has the demand for location-aware services. For instance, in the area of medical science, patient management and movement [1; 2; 3], concept of smart spaces that enable physical space and human interaction [4; 5; 6], in the area of logistics for the transportation of goods [7; 8], inventory management and warehousing [9; 10], environmental monitoring services use sensor networks for real-time weather predictions and to determine the source of pollutants that are present in air and water [11], and content sharing using social media platforms [12; 13].

A device that uses logic and arithmetic-based processes, computers were created in the past 70 years thanks to advancements in electronics. Powerful com-

puter systems that could do computations in logic and arithmetic faster than humans were made possible by further development. Artificial intelligence, one of the fields of computer science, researches how to create intelligent systems that might decide based on input parameters and prior information. The development of semi- and fully autonomous decision-making systems has been made feasible by advances in artificial intelligence during the past 15 years. One of these systems is an automated surveillance system that can find nearby objects, classify them, and estimate their properties.

One of the more sophisticated automatic surveillance systems allows for the automatic classification of targets to determine the type of object. Such a system conducts surveillance simultaneously for numerous target situations over broad areas. For instance, it may predict traffic conditions, determine the number and location of people within buildings, open doors automatically, turn on lights, alert the community to an invasion, and more. Sensory equipment is used to "sense" or comprehend the environment. Some sensors, such as radar sensors, are more sensitive than human senses, making them ideal for robotic surveillance.

The developments in a number of application scenarios, such as subsurface prospection [14; 15; 16], non-destructive testing [17; 18], and transportation infrastructure monitoring [19], also significantly contribute to the creation of new systems. The most promising technologies for use in these systems now are optical and radar sensors [20]. The energy of optical light is measured by optical sensors. These inexpensive sensors are capable of recreating images experienced by the human eye. In good lighting, it facilitates object recognition and removes obstructions. A wide vision, short-range surveillance system or a limited view, far-field surveillance system could be built using camera sensors. Good performance, however, can only be attained in favorable weather. Rain or fog could make them less effective.

Moreover, processing huge amounts of data necessitates the use of powerful gear. Contrarily, radar sensors rely on the reflection of electromagnetic waves. With the use of precise distance measurements, it is able to estimate the target's radial velocity in the highfrequency range. Radar sensors also operate in practically all weather and lighting conditions, and their capacity to pass through objects and have a vast range of operation are also advantages.

Short-range radars [21] are particularly intriguing within this framework due to their resistance to inclement weather and insensitivity to lighting issues [22], which can have a significant negative impact on video-based devices [23]. Applications for target detection and categorization used a variety of radar types.

1.1 Motivations

Due to its applicability and the engineers' constant need for better performance, estimation problems, and specifically parameter estimation, have attracted a lot of attention. The precise estimation of temporal and geographical characteristics attracted a lot of interest as applications grew. Sensor array processing has been an area of active research during the past decade because of the requirement to gather data from all sensors to provide an estimation. The processing of an array sensor depends on prior knowledge of the shape, properties, and quantity of the array's elements. The most regarded achievement of this method is the source location estimation using radars and sonars.

The classical beamformer approach is one of the early angle of arrival (AoA) techniques that was proposed in 1961 [24]. According to the core idea behind this technique, each antenna element should be given an equal amount of weighting when creating the steering vector [25].

Many efforts and attempts have been done to improve performance and in-

crease resolution of the conventional methods that requires environment-specific fine tuning. Short-range radars [21; 26] are particularly intriguing in this context because to their resistance to bad weather and insensitivity to illumination issues [22; 27], which can have a significant negative impact on antenna or video-based devices. Applications for target detection and categorization used a variety of radar types.

In particular, the FMCW radar technology has been widely adopted in the production of cost-effective and compact systems for several applications. On the one hand, unlike monostatic pulsed radars, these radars do not have the severe blind range problems that they often do [28]. On the other hand, they are typically less expensive and have a wider field of view than LIDAR and long-wave infrared (LWIR) sensors [22]. They can also deliver both range and velocity at the same time. Such information can be obtained through different processing schemes, e.g., by using a 2D FFT technique [29]. Moreover, unlike pulse and Ultra-Wide Band (UWB) radars, FMCW systems require lower sampling rates and lower peak-to-average power ratio to detect the distance and speed of multiple moving targets [30; 31].

1.2 Aims, Objectives and Contributions

The aim of this research is to make a system-level contribution to the analysis, design, and implementation of system components for tracking devices that can be utilized to improve location-based services and the user or asset location estimation. The angle estimation technique and the FMCW radar method are the system level components that are the subject of this work. Objectives identified towards this aim were to:

- **Objective 1** - Review and comprehend the uses of location-aware services

as well as their significance

- **Objective 2** - Model and simulate current estimate strategies while comprehending the parameter estimation challenge
- **Objective 3** - Contribute new techniques that enhance the capability of the chosen localization frameworks
- **Objective 4** - Design a novel processing chain for multi-target classification

The major contributions of this work are

- An overview of localization-aware services is presented in Chapter 2
- An experimental evaluation for moving target localization method using the Angle of Arrival and RSSI signal is presented in Chapter 3.5
- A new system that uses the Angle of Arrival signal estimation technique for localizing targets in a maritime environment is proposed in Chapter 3.6. Simulations and measurements have been carried out to evaluate the performance of the proposed system and the results prove that the proposed system can indeed localize targets under some known limitations
- A novel CNN based method for discriminating shadowed targets using an FMCW radar is presented in Chapter 4.4. The proposed solution is based on a CNN model that classifies the spectrogram images, obtained after a time-frequency analysis of the radar data, among one of two classes: One Target vs. Two Targets. The proposed solution achieves an accuracy of 92.2%
- An edge multi class action recognition system based on DL is also discussed in Chapter 4.5. This method used sequences of range-Doppler maps

extracted from a low-cost FMCW radar. The results showed that the model achieved the best accuracy (93.2%) in the 5-class classification case. Moreover, the same model distinguished fall from non-fall actions with an accuracy of 96.8% and a false-negative rate of 5.5%.

1.3 Outline of the Thesis

The thesis is structured as follows:

- Chapter 2 provides an introduction of the location based services. It describes the different positioning systems, including indoor positioning systems. Then a brief review of the used systems is provided
- Chapter 3 depicts the proposed localization system that uses the received Angle of Arrival signal. An experimental assessment for moving targets using AoA and RSSI in section 3.5. A maritime localization system that is based on IoT is proposed in section 3.6. Finally, in section 3.7, the patent claims and the proof of concept product are detailed
- Chapter 4 explains the proposed real-time target monitoring system that uses the FMCW radar. A CNN based method for discriminating shadowed targets is explained in section 4.4. In section 4.5, an edge multi-class action recognition system based on DL is proposed
- Chapter 5 summarizes the thesis and provides the outcomes of this research. This chapter discusses the findings drawn from each chapter and how the work may be expanded

Chapter 2

State of the Art

2.1 Introduction

To safeguard oneself from outside disturbance, knowledge and comprehension of our environment are crucial. For many years, people have built defense mechanisms to safeguard their possessions. Monitoring the environment around us is a crucial component of defense because it enables guardians to be ready for any unwelcome intrusion into their domain. There may be a wide range of civil applications for surveillance systems. For instance, knowing the amount of people inside buildings and their placements can help prevent and put out fires more effectively. Additionally, automatic door-opening and light-switching devices that use sensors could conserve resources. Drivers may be able to avoid collisions by paying attention to road conditions. However, the "human factor" may lead human-performed monitoring to be inexact "which might have unpredicted effects. Furthermore, a person's ability to perceive their environment is constrained. The "human element" auxiliary gadgets or assistance systems may help to lessen this.

A device that uses logic and arithmetic-based operations, computers were

created in the past 70 years thanks to advancements in electronics. Powerful computing systems that could perform computations in logic and arithmetic faster than humans were made possible by further development. Artificial intelligence, one of the fields of computer science, researches how to create intelligent systems that could decide based on input parameters. The development of semi- and fully autonomous decision-making systems has been made possible by advances in artificial intelligence during the past 30 years. One of these systems is an automatic surveillance system that can find nearby objects, classify them, and estimate their properties.

One of the more sophisticated automatic surveillance systems allows for the automatic classification of targets to determine the type of object. Such a system conducts surveillance simultaneously for numerous target situations over broad areas. For instance, it may predict traffic conditions, determine the number and location of people within buildings, open doors automatically, turn on lights, alert the community to an invasion, and more. Sensory equipment is used to "sense" or comprehend the environment. Some sensors, such as radar sensors, are more sensitive than human senses, making them ideal for robotic surveillance.

The creation of dependable monitoring and surveillance tools for use in urban settings and near-critical zones has recently attracted increased focus [32; 33; 34; 35]. For instance, the development of autonomous driving automobiles and continual improvements in the technology of autonomous vehicles sparked study into the creation of a pedestrian detection system to protect the safety of pedestrians [36; 37; 38; 39]. Additionally, the threat of domestic terrorism and criminal activity is currently seen as the primary impetus for researchers to create more dependable surveillance systems to be put in metropolitan locations [32].

The developments in a number of application scenarios, such as subsurface prospection [14; 15; 16], non-destructive testing [17; 18], and transportation in-

frastructure monitoring [19; 40; 41], also significantly contribute to the creation of new systems. The most promising technologies for use in these systems now are optical and radar sensors [20]. The energy of optical light is measured by optical sensors. These inexpensive sensors are capable of recreating images experienced by the human eye. In good lighting, it facilitates object recognition and removes obstructions. A wide vision, short-range surveillance system or a limited view, far-field surveillance system could be built using camera sensors. Good performance, however, can only be attained in favorable weather. Rain or fog could make them less effective.

Additionally, Wireless Sensor Network (WSN) continues to draw the interest of the telecom industry. They promise a wide range of potential uses, including traffic control and surveillance. Data collected by sensors for the majority of these applications should be linked to sensor placements because it is useless without knowledge of where it came from [42]. For the implementation of a WSN, precise node localisation is essential. In addition to being an essential component of the sensory context, positional information is also necessary for the localization of mobile radio nodes that use static nodes as a reference, as detailed in [43].

WSN is made up of numerous tiny sensor nodes with computing power, communication abilities, and sensing capabilities. Each sensor node is capable of detecting a variety of physical phenomena, including temperature, vibration, light, electromagnetic strength, humidity, and others, and transmitting the sensed data to the sink node via a network of numerous intermediary nodes. The WSN has been extensively utilized in numerous fields, including military operations, healthcare, and environmental inspection, due to its strong and functional capabilities. In many applications, in addition to the sensed data, the sensor node's location information is desirable. Additionally, routing efficiency can be increased by using the deployed sensor nodes' locations.

Thus, one of the most important problems in WSNs is how to locate or determine the placements of sensor nodes [44]. Our interaction with the physical environment has been facilitated by the development of WSNs. A WSN is made up of numerous widely dispersed sensor nodes, each of which has limited resources and is typically inexpensive. The network is frequently set up so that there must be several hops in order for the sensor nodes and base stations to communicate. Without knowing the locations of the corresponding sensor nodes, the data acquired in many WSN applications, such as monitoring and tracking, is useless [45].

Due to the enormous dimensions of directional antennas, Angle of Arrival (AoA) algorithms are rarely taken into account for WSNs; however, several system configurations are researched that can be easily implemented in pocket-size wireless devices. Finding the AOA of various multipath components is highly helpful since it enables antenna radiation pattern optimization and can be used to find and track phones that are active in a specific cell. Similar to this, understanding the AOA permits the design of antennas with optimized radiation patterns for on-body communications. This allows for determining the position of the antennas in relation to one another. The multipath impact can be reduced if diversity reception is used at one or both of the terminals. Using well-known methods like ESPRIT and MUSIC, as well as Ray-tracing techniques, the AOA may be calculated from the measured diversity data [46]. There haven't been any attempts, though, to use this for on-body AOA estimate using RSSI.

2.2 Angle of Arrival

The distance between two WSN nodes is estimated using the Received Signal Strength Indicator (RSSI), which displays the signal strength at the receiving end. As an overview, localization's core concept is as follows. The fixed anchor nodes are able to detect the beacon signal that is emitted by a tracked node with an unknown location. The received signal strength (RSS), time of arrival (ToA), or angle of arrival (AoA) of the received signal are the three characteristics that the anchor nodes measure [45]. An algorithm that identifies the general location of the tracked node uses these measurements as inputs. Each anchor node in the AoA estimates idea looks for the mobile node, or vice versa. As a result, the transmitted scanning beam must include both azimuth and elevation angles. To apply angle of arrival estimates, however, azimuth and elevation angle details were not covered in detail in earlier studies [45]. The theoretical relationship between RSSI values and distance between two nodes is inverse. Therefore, it is crucial to know the precise azimuth and elevation values, the angle between two nodes. Another study suggests a localization system that uses AoA estimates and more than one antenna for scanning and reading the RSSI value, which would raise the cost of creating the system [47; 48]. To achieve the highest RSSI value in [43; 49; 50], stepped motors are proposed. Stepped motor capable of rotating scanning beam 360 degrees. Nevertheless, the use of stepper motors increases power consumption while also raising system costs. Stepper-motor time delays also contribute to overall system inefficiency when using WSN AoA estimation algorithms.

In wireless networks, localisation based on Angle of Arrival (AoA) measurements has gained substantial popularity [51; 52; 53; 54; 55; 56]. This technique allows for the calculation of the characteristics that define the direction of radio wave propagation on the antenna array. Geodesic location or mobile geolocation

are examples of AoA uses [57]. A base station's many receivers can determine the AoA of the mobile's signal and determine the location of the mobile. Finding the position of military or spy radio transmitters is another purpose for AoA. In submarines, it is also utilized to locate objects with active or passive ranging. Additionally, interferometry in optics uses it. AoA placement is an easy technique. The base stations in mobile communications assess the AoA in relation to an absolute reference, such as north, for instance 28 [58; 59]. The user's position (xu, yu) can be estimated by transecting two lines that pass across the base stations with the measured angles, keeping in mind that the location of the base station (xb, yb) is known and the absolute angles can be measured [60].

With more space separating the positioning device from the mobile, the AoA positioning accuracy drops. As a result, AoA might not be appropriate for many positioning applications. When using Wireless Local Area Network (WLAN), access points close to the mobile device can provide precise positioning when compared to time-based solutions with a comparable signal bandwidth [61]. Angle of Arrival measurements include a number of drawbacks, including the usage of numerous sensors (microphones, antennas and ultrasonic sensors). Arrays are thought to be unsuited for integration due to their size and high cost, but as radio communications reach higher frequencies, the dimensions of the antenna get smaller and Micro-electromechanical systems (MEMS) technology advances. When array-enabled node platforms are present, integration becomes feasible. By incorporating multiple antennas in the same dimensions, a platform can be designed using four antenna elements, which does not cost very much.

2.3 Frequency Modulated Continuous Wave radar

Moreover, processing huge amounts of data necessitates the use of powerful gear. Contrarily, radar sensors rely on the reflection of electromagnetic waves. With the use of precise distance measurements, it is able to estimate the target's radial velocity in the high frequency range. Radar sensors also operate in practically all weather and lighting conditions, and their capacity to pass through objects and have a vast range of operation are also advantages.

Short-range radars [21; 26] are particularly intriguing within this framework due to their resistance to inclement weather and insensitivity to lighting issues [27], which can have a significant negative impact on video-based devices [23]. Applications for target detection and categorization used a variety of radar types. Particularly, the Frequency Modulated Continuous Wave (FMCW) radar technology has been widely used to create affordable and portable systems for a variety of applications [62; 63; 64; 65; 66].

On the one hand, unlike monostatic pulsed radars, these radars do not have the substantial blind range problems that they often do [67]. On the other hand, they are typically less expensive and have a wider field of view than LIDAR and long-wave infrared (LWIR) equipment [22]. They can also deliver both range and velocity at the same time. Such information can be acquired utilizing a variety of processing techniques, such as the 2D FFT approach [29]. Additionally, FMCW systems require lower peak-to-average power ratios and sampling rates than pulse and Ultra-Wide Band (UWB) radars to identify the distance and speed of several moving targets [31; 68].

In the literature, the shadow effect has been targeted only by a few [69; 70; 71; 72; 73; 74; 75; 76; 77; 78]. The authors proposed non-scalable solutions, thus requiring expert intervention for applying their methods in different environments. In this paper, we propose a novel solution for solving the issue of target identifi-

cation in the shadow region and we adopt Deep Learning (DL) techniques. This method is quantitatively analyzed and results are presented in Section 4.4.4. It benefits from the promising achievements presented in the literature of applying AI techniques on post-processed radar data. These techniques can help to dynamically learn suitable filters. This proposed solution is also scalable and does not need expert intervention.

In general, DL methods have proven to be very efficient in real-world image classification [79]. Moreover, DL techniques that use radar input are adopted for a wide range of applications, such as target classification [80], object tracking [23], and gesture recognition applications [81]. Among DL techniques, Convolutional Neural Networks (CNNs) are particularly suited for addressing image processing problems [82; 83]. Our proposed method uses a lightweight CNN model based on ImageNet (i.e., convolutional filters have been pre-learned based on ImageNet data [84]) to target the discrimination of shadowed targets, fine-tuning only the weights of the last layer (i.e., dense layer). The convolutional layers perform the feature extraction without any prior knowledge of the user. To validate the proposed solution, we address a two-class classification problem: one target vs. two targets. In the latter, one target is in the shadowing region of the other. Four models have been tested using the collected dataset. The best model in terms of accuracy is the MobileNet_V3 Large version; it achieves a generalization performance on the test set of 92.2%. The results encourage us to extend the adoption of CNNs in applications such as identifying and tracking more shadowed targets. In recent years, the application of radars for target detection at short and medium ranges has become ubiquitous [85]. The use of short-range Ultra-Wide-Band (UWB) and Continuous-Wave (CW) radars is becoming an attractive solution for localization purposes. Some radar systems applications include through-wall and through-fire detection [74; 86], the tracking of moving

targets during security operations [87], the detection of trapped people after an avalanche or earthquake [88], and the detection, tracking, and classification of multiple targets passing through a security gate [89].

Up to now, the bi-static radars (with at least one transmitting antenna and at least one receiving antenna) have resolved the detection and localization of a single stationary target, yet the problem of multi-stationary target detection has been less addressed. The bi-static radars are able to accurately detect targets that are closer to the radar antennas, whereas the greater the distance of the targets from the radar, the lower the accuracy of the detection [70]. This is mainly attributed to two factors. Firstly, as the transmission distance increases, the energy of the electromagnetic wave is attenuated; hence, the energy of electromagnetic waves reaching farther targets is inevitably smaller than that reaching the closest target.

Secondly, some targets, named recessive targets, can lie in the shadowed region of a dominant target (i.e., the closest to the radar). Thus, because the highest energy of the electromagnetic waves is reflected from the dominant target to the radar, the electromagnetic illumination of the recessive targets could decrease to the point where they are not detected [71]. Therefore, radar systems suffer from what is called the shadowing effect. This effect occurs when two targets stand in front of the antenna, one in the shadowing region of the other. The radar is usually not reliably capable of detecting the target that is standing in the shadow region [70]. This problem is common for most radar technologies, particularly, Ultra-Wide-Band (UWB) radar [74] and Frequency-Modulated Continuous-Wave (FMCW) radar [90]. Unlike pulse and Ultra-Wide-Band (UWB) radars, FMCW systems require lower sampling rates and lower peak-to-average power ratios to detect the distance and speed of multiple moving targets [30; 31]. Accordingly, the FMCW radar is a good solution for detection and localization purposes but performs poorly whenever the shadow effect occurs. The shadow effect is more

relevant in low-cost radars. This is due to their lower resolution compared to the high-end radars (higher range and velocity resolution) [91].

In [69], the shadow effect and its removal using PCL radar is investigated. A study on PCL radar performance under the shadowing effect is presented, when a distant, weak target echo is shadowed by strong echoes. In [70; 71], the authors outlined an origin of the shadow effect as the impact of the mutual shadowing of targets at the multiple persons tracking scenario. This explanation is confirmed by the experimental measurements. Other researchers investigated the shadowing effect for the purposes of person detection and tracking by UWB radars [72]. The results confirms the existence of additional attenuation within the shadow zones. In [73], a technique based on wavelet entropy is proposed because of the significant difference in frequency ratio components between the echo signal of the tested target and that of the masked target generated by dynamic clutter. Wavelet entropy can accurately detect multiple human targets in the presence of dynamic clutter, even if the distant human targets are in the shadow area of the closer target, as compared to the reference techniques of adaptive line enhancement and energy accumulation. In [74], a significant difference of frequency have been detected between the echo signal of the human target and that of noise in the shadowing region. The authors concluded that the target detection using the power spectrum is not effective. Therefore, an auto-correlation algorithm is applied to the pre-processed signals in order to compute the wavelet entropy. Results showed that the proposed approach is capable of detecting a shadowed target. Other application were addressed in the literature [75; 76; 77; 78]. In general, none of previous works presented a scalable solution for solving the shadowing effect. In fact, those solutions requires expert intervention for applying them in different environments.

Several works involving the use of FMCW radar has been reported in the liter-

ature. In [81], the authors introduced a novel system for dynamic continuous hand gesture recognition based on a frequency-modulated continuous wave radar sensor. They employed a recurrent 3D CNN to perform the classification of dynamic hand gestures and achieved a recognition rate of 96%. In [92], the authors proposed a prototype of a FMCW radar system for classification of multiple targets passing through a road gate. The classification covered four classes: pedestrians, motorcycles, cars, and trucks and achieved an accuracy of 88.4%. Many other applications were tackled in the literature [90; 93; 94; 95; 96; 97; 98; 99; 100]. Most of the systems presented in the aforementioned works suffer from the shadow effect. However, none of them proposed a solution for it.

Deep learning classification techniques for radar target classification has also been adopted in the literature. A practical classification of moving targets system, based on automotive radar and deep neural networks is presented in [101]. The study presents results for classification of different classes of targets using automotive radar data and different neural networks. In addition, A Human-Robot classification system based on 25 GHz FMCW radar using micro-Doppler features was introduced in [102]. The raw Range-Doppler images were directly fed a CNN resulting in a performance of 99% accuracy for identifying humans from robots. Many other applications that uses neural networks for radar problems were tackled in the literature [103; 104; 105; 106; 107].

Indoor falls are a major public health concern and the main cause of accidental death in the senior population worldwide. Timely and accurate detection permits immediate assistance after a fall and, thereby, reduces complications of fall risk [108]. Edge-based approaches are essential to support time-dependent healthcare applications [109]. Due to the advantages of portability, low cost, and availability, wearable devices are regarded as one of the key types of sensors for fall detection and have been widely studied [110; 111; 112; 113]. The main

drawback of these systems is the battery life which can limit the usability of the wearable devices. The second drawback is that the monitored subjects must always wear them, causing obvious discomfort, especially for elderly. Vision-based fall detection is another prominent method. Extensive effort in this direction has been demonstrated, showing promising results [114; 115; 116]. Although cameras are not as portable as wearable devices, they offer other advantages which deem them as decent options depending on the scenario: most static RGB cameras are not intrusive and wired, hence there is no need to worry about battery limitations. One major inconvenience of vision-based detection is the potential violation of privacy due to the levels of detail that cameras can capture, such as personal information, appearance, and visuals of the living environment. In addition, vision-based approach could introduce issues related to color bias [117]. The ambient sensors (e.g., ultrasonic, WiFi antennas, radars, etc.) provide another non-intrusive means of fall detection. Ambient sensing is drawing more attention which can be attributed to being device-free for users and can solve the problem of people's privacy and color bias. Ultrasonic sensor network systems are one of the solutions for fall detection [118]. In [119], a fall detection approach uses WiFi signals, showing impressive results in detecting falls.

Non-contact indoor monitoring using radars is getting popular in recent years [120]. In [121; 122; 123], the human action recognition is performed by a machine learning (ML) algorithm trained on hand-crafted features extracted from the radar signals. The main drawback of these techniques is the time and effort required for the processing of the data and the features extraction operation. Some other works propose deep neural networks (DNNs) to automatically extract features for human actions recognition and fall detection. In [124], stack auto-encoders (AEs) are used to automatically extract the features from the gray-scale spectrogram and to classify four activities including the fall. In [125], the

authors combine convolutional neural networks (CNNs) and AEs to classify twelve actions based on micro-Doppler signatures. In [126], two DNNs automatically extract the features from the time series corresponding to the fast time of an ultra-wideband (UWB) radar return signals and classify fall actions. In [127], bidirectional long short-term memory (LSTM) networks classify activities, in real-time, based on the fusion of data collected using radar and wearable devices. In [128], LSTMs with and without bi-directional neurons classify the activities based on the micro-Doppler spectrograms. The data are considered as a continuous temporal sequence. In [129], the authors adopt a generative adversarial network (GAN) to enrich with synthetic samples a dataset containing a low number of micro-Doppler signatures representing human actions. Using this method, the capability of generalizing on new data is increased. In [130], a DNN takes binary-masked spectrograms as input. Those are computed on the signals of the UWB radar, classifying falls. In [131], the authors propose an algorithm to extract the optimal range bin from the range-Doppler spectrograms of a moving target for the subsequent time-frequency analysis, then a DNN built upon a pre-trained model classifies the falls based on the optimal resulted spectrograms.

Chapter 3

Real-time Target Monitoring using Received Angle of Arrival Signal

3.1 Summary

This chapter is arranged as follows, in section 3.2 the Angle of Arrival method is introduced. In section 3.3, we explain the localization technology using AoA and Received Signal Strength (RSSI). In section 3.4 the hardware components used in this study are presented. In section 3.5 the experimental assessment of moving targets localization performance is detailed. In section 3.6 a maritime localization system is proposed and the results are examined. In section 3.7 we get a brief look on the patent claims. Finally, in section 3.8, this chapter is concluded.

3.2 Angle of Arrival Use Cases

The problem of determining the spatial relationship between various things is one that is receiving a lot of attention due to recent technological advancements and customer demand. Localization is the term for this process, which has several widespread uses [132; 133; 134]. Geolocation is the process of using the earth as the reference frame in localization procedures.

However, without precise transmitter node position data, the data gathered for these applications is meaningless. Future smart antenna technology will rely heavily on direction-finding algorithms because the Global Positioning System (GPS) has limitations due to the need for Line of Sight (LOS) between the satellite and the GPS receiver [135].

For both military and non-military services, these techniques are necessary to accurately predict the bearing angle on the receiver array. When it comes to the emergency response services, the accuracy of these algorithms is crucial. An increased interest in the topic of direction finding (DF) has been sparked by the significant advancement in smart antenna technology over the past ten years. Using Digital Signal Processing (DSP), numerous antenna elements can be coupled in smart antenna technology to adapt the antenna radiation pattern per neighboring channel.

Through beam steering, these intelligent antenna systems can increase the capacity of cellular wireless networks [136]. The correct estimate of the user position must be calculated in order to send the beam toward the appropriate user who is demanding access to the network resources. The authors of [137; 138; 139] have supplied comprehensive references and quantification of the effectiveness of the current localization approaches. Numerous applications, such as autonomous mobile robot navigation [140; 141; 142; 143], underwater navigation [144], public health and social media [145; 146; 147], emergency services, etc., have used

localization techniques.

3.3 Direction of Arrival Estimation Algorithms Using Antenna Arrays

The calculation of (ϕ, θ), where ϕ denotes the azimuthal angle and θ denotes the elevation angle of the impinging planar wave on an antenna or array of antennas, is related to the direction of arrival problem.

The plane wave is thought to have infinite parallel wave fronts with constant amplitudes and to have a constant frequency. The estimate problem is reduced to merely estimating the azimuthal angle ϕ in a one-dimensional plane. The expression for the plane wave impinging at point x at time t is given as follows:

$$\mathrm{S}(\mathbf{x}, \mathrm{t}) = A\mathrm{e}^{\mathrm{j}(\boldsymbol{\beta}\cdot\mathbf{x}-\omega\mathrm{t})} \tag{3.1}$$

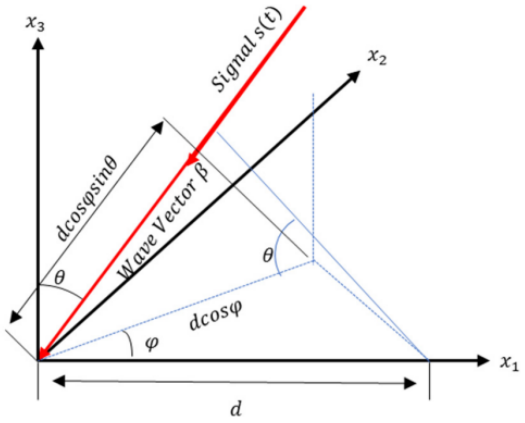

Figure 3.1: Geometry representing the DOA of the signal as an azimuth and elevation angle pair on an antenna array

where A is the peak amplitude, $\beta = \frac{2\pi}{\lambda}$ is the wave factor, $\lambda = \mathrm{c/f}$ the wavelength of frequency f, c is the speed of light and is the angular frequency

defined as $\omega = 2\pi f$.

Using the above equation 3.1, the arriving signal at an antenna located at $(x1, x2, x3)$ with origin $(0, 0, 0)$ can be defined as:

$$s(x,t) = s(\mathbf{0},t)e^{j\beta(x_1\cos\varphi\sin\theta + x_2\sin\varphi\sin\theta + x_3\cos\theta)} \tag{3.2}$$

If there are M omnidirectional isotropic antennas that have a unity gain arranged in a Uniform Linear Array (ULA) with uniform spacing d between them on the $x1-axis$ then the arriving signal at the mth element can be described as:

$$\mathrm{s_m(t)} = \mathrm{s((md,0,0),t)} = \mathrm{s}(\mathbf{0},\mathrm{t})\mathrm{a_m}(\varphi,\theta) \tag{3.3}$$

where, $\mathrm{a_m}$ is the steering factor of the mth element and is equal to:

$$\mathrm{a_m}(\varphi,\theta) = \mathrm{e}^{\mathrm{j}\beta m\ \mathrm{d}\cos\varphi\sin\theta} \tag{3.4}$$

The above equation 3.4 describes a progressive phase shift

$$\beta md\cos\varphi\sin\theta = \frac{2\pi}{\lambda}md\cos\varphi\sin\theta = 2\pi f\frac{md\cos\varphi\sin\theta}{v = f\lambda} = \omega t_d \tag{3.5}$$

Equation 3.5 represents the time $\mathrm{t_d}$ it will take the plane wave to propagate $md\cos\varphi\sin\theta$ in the direction of the incident wave. Now for the case of Uniform Circular Array (UCA) with element spacing of $\frac{2\pi R}{M}$ arranged on a circle of radius R the arriving signal at the mth element can be described as

$$\mathrm{s_m(t)} = \mathrm{s}\left(\mathrm{Re}^{\frac{\mathrm{j}2\pi\mathrm{m}}{\mathrm{M}}},\mathrm{t}\right) = \mathrm{s}(\mathbf{0},\mathrm{t})\mathrm{a_m}(\varphi,\theta) \tag{3.6}$$

where in this case, the antenna factor for the mth antenna can be described as:

$$a_m(\varphi, \theta) = e^{j\beta R \sin\theta \cos\left(\varphi - \frac{2\pi m}{M}\right)} \tag{3.7}$$

For simplicity from here onward unless otherwise stated it is assumed that the elevation angle $\theta = 90$ making $\sin\theta = 1$.

3.3.1 Interferometry

According to the interferometry principle, if a plane wave approaches an antenna array at an angle, two separate elements will receive it with a temporal delay because of the difference in the length of the path. Signals received by antennas have a phase difference as a result of this variation in travel length.

$$\Delta\varphi = \left(\frac{2\pi}{\lambda}\right) d \cos\varphi \sin\theta \tag{3.8}$$

Some baselines should be established in order to determine the angles. Three antenna elements, which can be arranged in an equilateral triangle, are required to create two baselines. The methods for measuring phases include the Fourier transform, digital, and analog methods.

In correlative interferometry, the reference phase differences for the direction-finding (DF) antenna are compared to the measured phase differences at each wave angle. The values with the highest correlation are taken into account as the measured phase angle column is passed through the matrix of reference phase angles. The angle at which the incoming signal arrives is represented by this value.

During the calibration procedure, a model is created to comprehend the behavior of the antennas, and the reference phase differences, or "array manifold," are measured. The non-ideal elements of the system must be taken into account while creating a theoretical model in order to increase the accuracy of the practi-

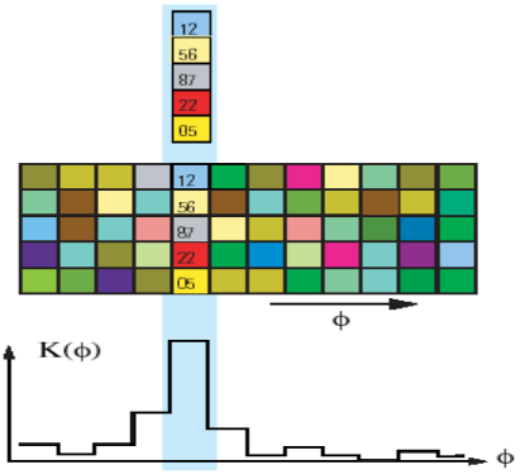

Figure 3.2: Correlative Interferometer

cal systems because the theoretical array response values may differ significantly from the practical values. Regular azimuthal and frequency stepping, along with known locations, are used to convey a signal to the receiver. A calibration table is then created using the differential phase and amplitude measurements. Figure 3.2 shows a correlative interferometry demonstration in action. The columns in the data matrix represent the direction and are utilized to create a comparison vector. The data set comes from a 5-element antenna array. The upper data vector includes the measured phase discrepancies. Each column in the reference and measurement vector matrices is correlated with the other matrix. As a result, the correct angle will be the one that has the greatest correlation with the comparison vector matrix.

3.4 Hardware components

In this section, the hardware components that are using during the following phases are presented and detailed.

The proposed systems are mainly based on the AoA Booster Pack (BOOSTXL-AoA) [148]. The Angle of Arrival BoosterPack kit (BOOSTXL-AOA) is an easy-to-use plug-in module equipped with antenna arrays suitable for evaluation of Angle of Arrival applications. The 2 orthogonal antenna arrays each consist of 3 dipole antennas tuned for operation at 2.4 GHz. The antennas are selected with RF switches and then connected to a single JSC connector. The JSC Series connector is used to connect to an AoA compatible RF receiver like the CC2640R2 LaunchPad. Figure 3.3 depicts the Texas Instruments-designed antenna, and Figure 3.4 the corresponding block diagram.

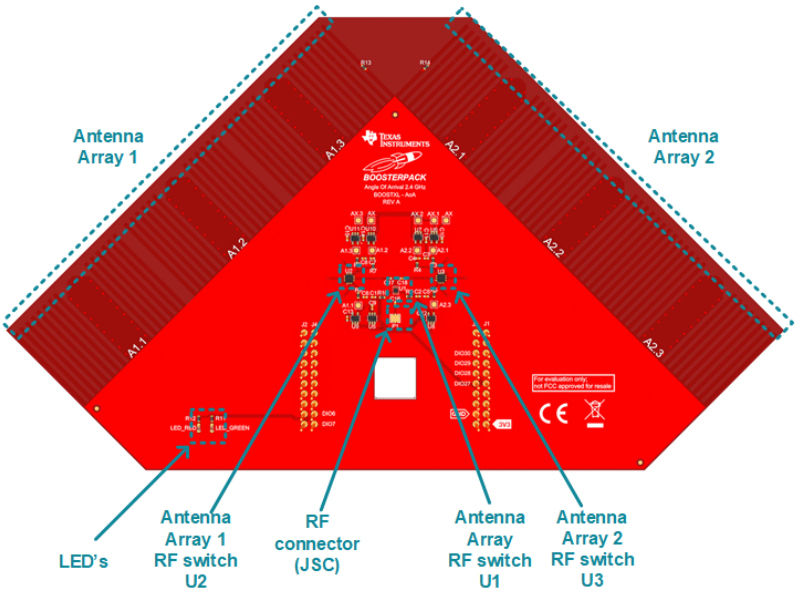

Figure 3.3: BOOSTXL AoA Antenna

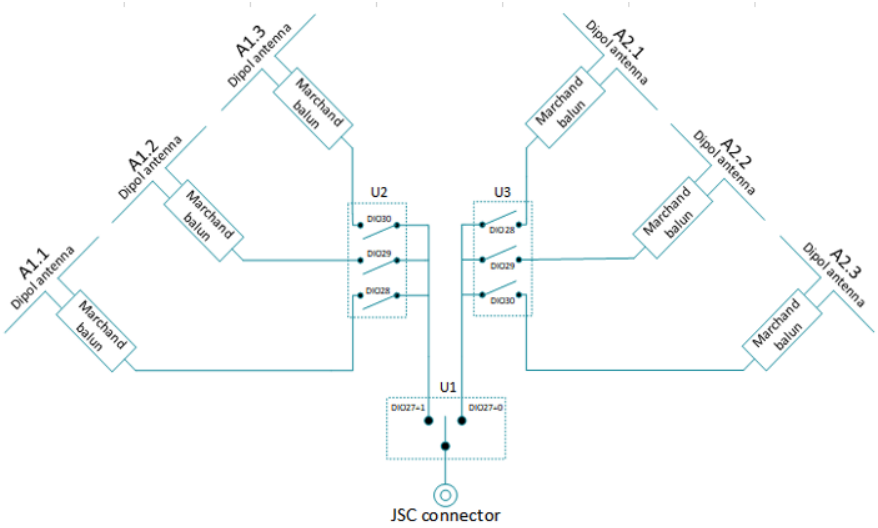

Figure 3.4: BOOSTXL AoA Antenna block diagram

The key features of this antenna are the following:

- Two antenna arrays with three 2.4 GHz dipole antennas on each side
- RF switches to switch between the different antennas
- JSC RF connector

The BOOSTXL-AoA board contains two orthogonal arrays, each with three dipole antennas. Each antenna array can theoretically cover an angle on the incoming signal up to ±90°. When using both arrays combined, a coverage of up to ±135° is achievable (The two antenna arrays overlap 45° on each side). Dipole antennas are by nature differential and needs to be fed with a balanced signal. A balanced signal is created using a marchand balun that is integrated in the PCB. The single ended side of the baluns are fed to the antenna switches (U2 and U3). The array switch, U1, is used to connect each array to the JSC connector.

This antenna is mounted on a LaunchPad that should be configured to use an external antenna. The CC2640R2 LaunchPad kit (LAUNCHXL-CC2640R2)

[149] brings easy Bluetooth low energy (BLE) connectivity to the LaunchPad ecosystem with the SimpleLink ultra-low power CC2640R2F wireless MCU.

The CC2640R2F is a wireless MCU targeting Bluetooth 5 (single-mode BLE) and proprietary applications. The CC2640R2F device contains a 32-bit ARM® Cortex®-M3 processor running at 48 MHz as the main processor, in addition to a 2nd programmable CPU ideal for ultra low-power sensor reading and data processing. It can run independently of the main ARM® Cortex®-M3 MCU and handle sensor polling using just a few µA of average current.

The CC2640R2 LaunchPad kit is supported by the SimpleLink Starter app for iOS and Android. This app connects your LaunchPad to a smartphone using Bluetooth. The Starter app supports reading the LaunchPad buttons, controlling LEDs and all I/O signals on the BoosterPack™ connectors. It also supports setting up cloud connectivity to the IBM Quickstart server or to any cloud service via MQTT. This enables a cloud view where you can control your LaunchPad from any web browser in minutes after setting it up.

The CC2640R2 LaunchPad kit can also be upgraded to the latest firmware version with the over-the-air (OTA) upgrade from the SimpleLink Starter app. Figure 3.5 shows the antenna designed by Texas Instruments.

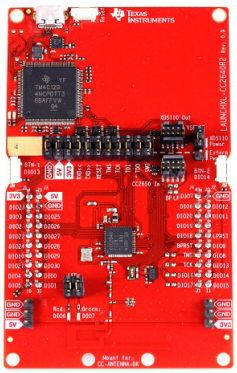

Figure 3.5: CC2640R2F LaunchPad

The key features of this LaunchPad are the following:

- Onboard emulation tool (XDS110) for flashing debugging firmware on the target CC2640R2F device
- 40-pin dual-gender BoosterPack connectors
- CC2640R2F Microcontroller device
- Access to all GPIO pins of the CC2640R2F device
- 8 Mbit serial (SPI) flash memory for firmware updates

The wireless MCU LaunchpadTM SensorTag LPSTK-CC1352R [150] is the beacon taken into account in this investigation. With integrated environmental and motion sensors, multiband wireless connectivity, and simple-to-use software, the TI LaunchPadTM SensorTag kit makes it simple to prototype connected applications. Developers may quickly construct connected apps with one kit that support Bluetooth® Low Energy, Bluetooth mesh, Zigbee, Thread, and custom protocols on both 2.4 GHz and Sub-1 GHz frequencies for versatility.

By providing a fully contained, battery-operated kit that enables rapid prototyping, this new offering enhances the TI LaunchPad ecosystem and enables IoT developers to test out new product ideas without having to create any hardware or software from scratch. With this ready-to-use hardware, designers can get started quickly with four built-in sensors, battery operation, and the option to add many more through the TI BoosterPackTM ecosystem and additional parts.

Because it is based on the CC1352R multi band wireless MCU, which is a component of the SimpleLinkTM microcontroller platform and offers all the building blocks for a secure and low-power connected topology, the LaunchPad SensorTag kit is more distinctive. Developers may easily combine hardware to build the desired topology using the LaunchPad development ecosystem and a wide range of

wireless connectivity stacks to link everything and everything. It is simple to port applications created for the LaunchPad SensorTag kit to additional SimpleLink CC13x2 and CC26x2 wireless MCUs.

Figure 3.6: LPSTK-CC1352R LaunchPad

The main features introduced by this beacon are:

- Enables the developer to operate simultaneously across several wireless stacks (Bluetooth Low Energy, Bluetooth Mesh, Sub-1 GHz, Thread, ZigBee®, and 802.15.4) with a radio that is FCC, CE, and IC certified for 2.4 GHz and Sub-1 GHz
- Supports the TI 15.4-Stack, Wireless M-Bus, MIOTY® technology, IPv6-enabled smart objects (6LoWPAN), IEEE 802.15.4g, and other proprietary technologies (Sub-1 GHz)
- Features four on-board low power sensors: accelerometer, temperature and humidity, hall effect, and ambient light (OPT3001)
- Operates off AAA batteries, with the option of adding a coin cell battery holder and using a CR2032 for applications requiring less power.

- Compatible with TI BoosterPack Ecosystem and a variety of additional hardware parts to increase capabilities to suit your design
- Demonstrates the Integrated Passive Component (IPC), which was created expressly to work with the CC1352R MCU and allows for design simplification by decreasing the number of RF passive components from 23 to 3

3.5 Experimental assessment of moving targets localization performance based on Angle of Arrival and RSSI

Localization based services are in the process of being ubiquitous, it is then essential to find a low-cost and low-energy solution for localization of moving targets. Bluetooth-based solutions for indoor localization have become increasingly popular in recent years. In addition to its availability (e.g., BLE is available on most modern smart devices), Bluetooth Low Energy technology is an economical and simple solution to the industry. To the best of our knowledge, none of the existing indoor localization systems use both Angle of Arrival and Received Signal Strength Indication. This chapter presents the experimental assessment of a single device localization system that uses Angle of Arrival and Received Signal Strength Indication for localization of moving targets using Bluetooth. The results demonstrate that the developed system is an important step towards a new generation of real-time indoor localization systems that can locate targets with high accuracy (e.g., AoA accuracy: 89.2 %), and an improvement concerning the cost of the implementation.

With the widespread of the Internet of Things (IoT), wireless localization technology is gaining importance due to its low-cost and ubiquitous availability. Because of its excellent identification ability, Global Navigation Satellite Systems (GNSS) such as Global Positioning System (GPS) have made great success in map navigation, people and objects tracking, etc. However, GNSS are unavailable when building localization systems for indoor environments because of the great attenuation of the satellite signal causing by the obstruction from buildings. Nevertheless, with the fast development of the IoT, there is a growing demand for indoor Location Based Services (LBS). Indoor LBS applications (e.g., shop-

ping navigation, and fire rescue, etc.) provide services relying on the target's location, which is the key factor for the performance, accuracy, reliability of LBS applications.

Many indoor localization methods were previously assessed, including Infrared (IR) systems, Ultrasonic (US) systems [151], and Optical-based frameworks. These systems share several common underlying properties, such as being sensitive to multipath effects, high costs, and complexity. Consequently, the focus of researchers has been shifted to Radio Frequency (RF) indoor localization technologies, including Radio-Frequency Identification (RFID) [152], ZigBee [153], Wi-Fi, Bluetooth Low Energy (BLE), and Ultra-Wide Band (UWB). Several notable factors should be considered in selecting base technology for developing an indoor localization system, such as cost, accuracy, robustness, scalability, power requirements, reliability, and coverage. Over the last few decades, there has been a significant surge of interest for BLE-based technologies, as one of the most reliable RF-based localization frameworks due to its availability, low power consumption, and low cost.

BLE [154] is a range-based localization, it performs localization by estimating the distance between a target sensor node and reference nodes. BLE has been studied intensively for localization and user tracking in recent years. Its low complexity due to the availability of Received Signal Strength Indication (RSSI) measurements [155], the low power consumption, low cost, and the ease of device deployment make it an attractive technology for localization. In addition, Angle of Arrival (AoA) localization is a nonlinear estimation problem. It determines the source position based on the propagation direction of an incident radio frequency wave from an antenna array, such as Switch Antenna Array (SAA), which has been an active research field for several decades [**?**]. Both localization methods (AoA and RSSI), generate a new localization strategy that can dynamically locate

targets.

3.5.1 Adopted localization methods

Bluetooth proximity solutions and positioning systems were used to date using signal strength to estimate distance. The new direction-finding feature in Bluetooth Core Specification v5.1 makes it possible for Bluetooth devices to determine the direction of Bluetooth signal transmission. In addition, Bluetooth 5.1 specification allows low-energy transmissions to sacrifice data rate for more range. Next, the used localization methods will be explained.

3.5.1.1 Angle of Arrival

Bluetooth 5.1 AoA measures the angle or direction a BLE transmitted signal approaches a Bluetooth receiver. To calculate the AoA, two or more antennas are required to measure the phase of an incoming signal.

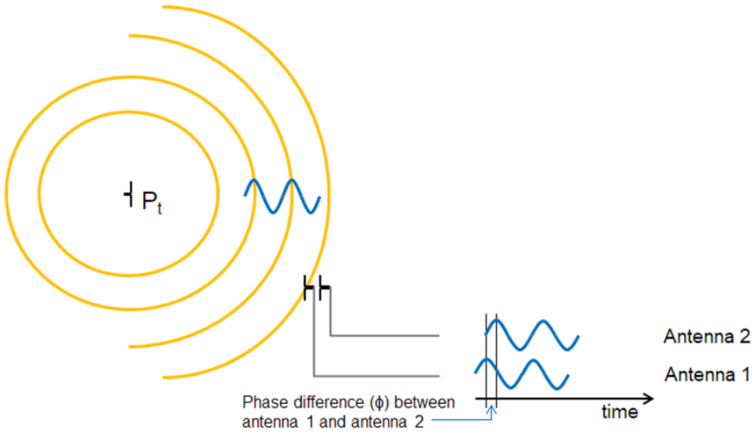

Figure 3.7: Transmitter Phase Measured by Antenna Array

Figure 3.7 explains how the phase measurements from each antenna are used to calculate the AoA and determine the direction of the transmitted signal. To calculate the AoA, the incoming RF carrier phase must be measured with minimal

impact to the signal phase of the carrier itself using two or more co-located antennas. Phase Difference (Φ) is measured by connecting at least two antennas to the same receiver sequentially (more antennas can be added). Figure 3.7 shows the constellation diagram which illustrates signal vectors from two antennas. Last step is converting the phase shift (Φ) back to AoA (θ). This way, the direction of the target will be known.

3.5.1.2 Received Signal Strength Indication

It is an estimated measure of power level that an RF client device is receiving from an access point, router, or antenna. RSSI indicates the power level being received after any possible loss at the antenna and cable level. The higher the RSSI value, the stronger the signal. When measured in negative numbers, the number that is closer to zero usually means a better signal. As an example, -50 is a pretty good signal, -75 is reasonable, and -100 is no signal at all.

Having beacons placed at fixed known location and by measuring distances based on signal strength, a smartphone can calculate a location using trilateration technique as described below. The first step is to convert the measured signal strength (RSSI value) to distance. This is usually done using the formula based on the physical property of the radio waves that their energy decreases exponentially with distance. Based on this, the distance can be calculated as:

$$d = 10((P - S)/10N) \tag{3.9}$$

Where

- d-estimated distance in meters
- P - beacon broadcast power in dBm at 1 m (Tx Power)
- S - measured signal value (RSSI) in dBm

- N - environmental factor (usually value between 2 and 4)

Once the distances to known beacons are estimated, the device can calculate its position in relation to those beacons using technique called trilateration.

3.5.1.3 Locate the target

The eligible question now is, how would it be possible to locate the target after collecting AoA and RSSI values? After measuring the phase different and converting it to anlge. The direction of the target is now known. The only missing feature is distance. This is where we convert the measured RSSI value to a distance estimation using the Equation 3.9.

3.5.2 Proposed System architecture

This testing system is based on the AoA Booster Pack (BOOSTXL-AOA) that is mounted on top of the CC26X2R board. The Booster Pack (antenna) is responsible for determining the direction (AoA) and the RSSI of the target and sending this data to the CC26X2R board. The CC26X2R board is responsible for sending the received data using USB to a Raspberry Pi board that is preprogrammed to watch the UART connection and wait for incoming data stream (from the CC26X2R board). This data is then stored and transmitted using MQTT protocol to a Mongo database for later use. On the other side, the multiband CC1352R wireless MCU Launchpad Sensor Tag kit (LPSTK-CC1352R) by Texas Instruments is used as an RF target.

The Texas Instruments Angle of Arrival Booster Pack (BOOSTXL-AoA) assesses the performance of the AoA and RSSI localization methods using BLE 5.1. The BOOSTXL-AoA board contains two orthogonal arrays, each with three dipole antennas. Each antenna array can theoretically cover an angle on the incoming signal up to $\pm 90°$. When using both arrays combined, coverage of up to

±135° is achievable (The two antenna arrays overlap 45° on each side). Dipole antennas are by nature differential and need to be fed with a balanced signal. A balanced signal is created using a march and balun that is integrated into the PCB. The single-ended side of the baluns is fed to the antenna switches (U2 and U3). The array switch, U1, is used to connect each array to the JSC connector.

3.5.3 Experimental Assessment Procedure

In this section, experiments using the antenna and several RF tags are presented. The experiments have been conducted in different scenarios to assess different aspects of the system. The accuracy of the AoA and RSSI values are the most important metrics for this system (to ensure localization quality). In addition, it is important to measure the duty cycle, latency, coverage area, and power consumption of the proposed system to prove that the proposed system is reliable. The testing protocol is presented in this section where the results are presented in the following section.

3.5.3.1 Experimental Setup

As described in the previous section, the testing setup was built as a proof of concept of the reliability of the system. As shown in Figure 3.8 below, all the components of the system were installed on a base structure and connected to a touch monitor screen to see the results in real-time.

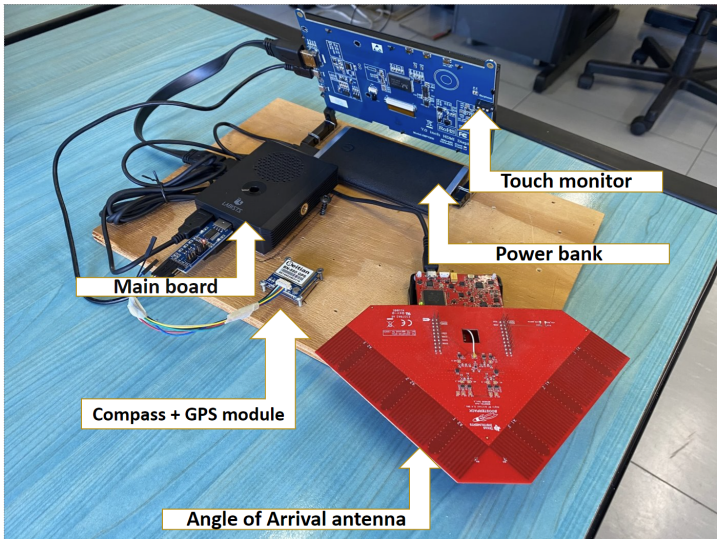

Figure 3.8: Testing Setup

3.5.3.2 Experimental methods

A testing protocol was chosen for each experiment following the specification of each measured metric. Such protocols are explained below.

Received Signal Strength Indication

To start with, a user moves away from the base station to test the maximum radio transmission range of the node, which was thirty meters. Since an RSSI value cannot be a decimal or a fraction, it cannot offer enough resolution to distinguish fine-grained changes in distances. Instead, it can only provide resolution to distinguish between distances that are large enough to cause at least a unit change in dBm of the signal power at the receiving node. Therefore, it is unnecessary to test RSSI values by using small increments in distances. In this experiment, the RSSI value is tested every meter, each test lasting for 30 seconds. By averaging all the values obtained during this time, the valid RSSI at each testing location can be calculated. There are different scenarios to be covered to fairly quantify

the performance of the antenna with what concerns the RSSI measure. For example, elevation between the antenna and the target is an important factor that certainly affects the performance of the RSSI measurement. The experiment was being carried out in a long corridor made up of two concrete walls. The testing platform was used as a base station directly connected to a 7" monitor screen via an HDMI cable to retrieve data. The RF target was mounted on three different elevations with reference to the coordinator. Both nodes operated with a full battery. No additional obstacles were standing in the communication path between the two nodes during the experiment. Thereafter, three scenarios were tested. For each scenario, we will take five measurements for each distance from one to thirty meters, equally distributed with a one-meter difference: Antenna higher than the target - Antenna lower than the target - Antenna and target on the same level. For each of the previously mentioned cases where the antenna and target are in the line of sight without additional obstacles, measures for thirty seconds were performed for each distance, and they were averaged to provide a fair result.

Angle of arrival

Measurement of AoA can be done by determining the direction of propagation of a radio-frequency wave incident on an antenna array or determined from maximum signal strength during antenna rotation. The performance of AoA was tested in an indoor situation. These tests were conducted in a large empty closed room where the AoA antenna was positioned on a table, and a set of different angles orientations of the RF tag was tested. Those tests covered the 200 degrees range of the antenna. Since an AoA value cannot be a decimal or a fraction, but only a number between minus one hundred to plus one hundred. It cannot offer enough resolution to distinguish fine-grained changes in angle. Therefore instead, it can

only provide resolution to distinguish between angles that are large enough to cause at least a unit change in angle. Therefore, it is unnecessary to test AoA values by using small increments in angle. In our experiment, the AoA value was tested every ten degrees for a five meters distance, each test lasting for 30 seconds. By averaging all the values obtained during this time, the valid AoA at each testing location was calculated. The antenna and target were in the line of sight, same elevation, and without additional obstacles.

Duty Cycle

The duty cycle is the number of localization messages that are sent/received per minute. A localization message includes AoA and RSSI measures. The measurement of this factor was assessed by counting the number of received messages for ten minutes and finally averaging them.

Coverage Area

The radius of the area that is covered by the antenna, considering that the antenna only covers a 135 degrees space. To assess the maximum coverage distance, an outdoor test was needed (large empty car parking space). A person holding the RF tag walked away from the antenna, when the connection stopped between the RF tag and the antenna, the measure between the antenna and the person holding the RF tag was measured. This test was repeated five times and the distance was eventually averaged. This value is presented in meters.

Latency

The latency is the time needed by the system to detect a new target that enters the coverage area. To test the latency, we used a large empty outdoor area (car parking space), and placed the target on a distance that is larger than the

coverage area, where is antenna cannot detect it. Then, and while the antenna was looking for targets, a person holding the RF tag entered the coverage area. The time between the RF tag entering the coverage area and its detection was calculated using a stopwatch and repeated twenty times before averaging the results. This value was represented in seconds.

Power Consumption

The amount of power used by each of the components of the system (Antenna and Raspberry™ Pi). This factor was assessed using a USB multi-meter that indicates the amount of energy consumed by the USB attached to it.

3.5.4 Experimental Results

The results of the predefined metrics are divided into two sections. The first section presents the performance of the proposed system as a localization method. The second section presents the results of the evaluation metrics that are relevant to the proposed system.

Localization

The localization method used consists of two elements: AoA and RSSI. Both elements should give a reasonable performance so that the localization system works well. Figure 3.9 shows the average RSSI received along thirty meters of the indoor range. It shows three different lines, each represents an elevation state between the antenna and the target.

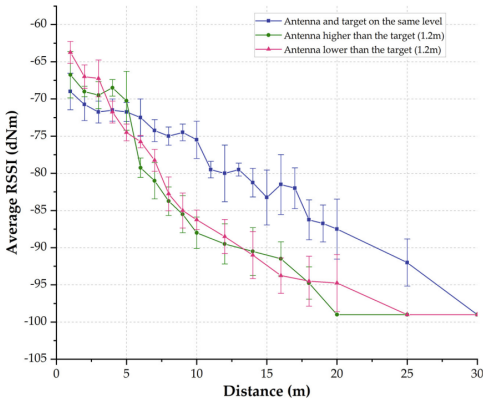

Figure 3.9: Received RSSI results

With reference to the AoA calculation, Figure 3.10 shows the AoA received with comparison to the real angle. The RF tag was placed five meters away from the antenna for each angle measurement. The RF tag was placed on the same elevation as the antenna. Each triangular point in the graph below is respective to one of the twenty-one trials that were done for different angles; the incoming stream of data was collected for thirty seconds and averaged.

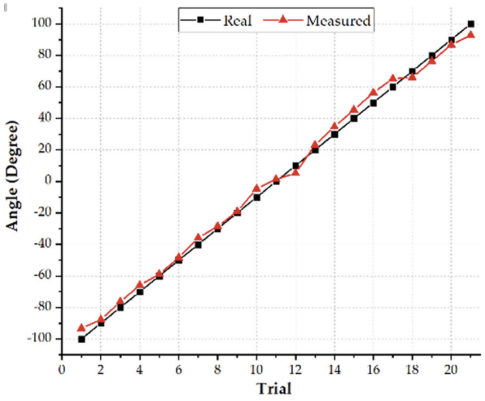

Figure 3.10: Received AoA results

Alongside the localization performance, it was important to track the performance of key metrics (latency, power consumption, scalability, etc.). The duty cycle was 4.28 seconds, which means that the system sends fourteen localization

messages every minute. With reference to the proposed method, the accuracy was between 0.5 and 1 meters for the presented scenario, the implementation cost was very low (twenty dollars for an antenna), and the system is easily scalable.

Figure 3.9 shows that the value of RSSI and the distance are inversely proportional, which is the expected pattern from an RSSI receptor. Regarding the AoA, Figure 3.10 shows that the real and incoming AoA over 21 trials (measurements) are consistent. The average accuracy per trial is around 89.2% which is reasonable [156]. Therefore, the BLE 5.1 localization technology that uses AoA and RSSI was effective under the presented circumstances and scenarios. In addition, with comparison to the state-of-the-art technologies, BLE 5.1 has a respectively lower accuracy than the Ultrasonic Based (UWB), but on the other hand, BLE 5.1 is lower in cost, has a larger coverage area, has less latency, and has a very low power consumption.

3.5.5 Conclusion

This section presented a wireless system for the indoor localization of targets using a single wireless device. The system uses new BLE 5.1 features based on AoA and RSSI methods. The time latency and accuracy of the system have been measured. The proposed system operates in real time with 1.5-2 s delay and with an accuracy of 89.2%. Although more extensive experimentation is needed to fully evaluate our system, with respect to available systems in the literature, the proposed system is reliable, has low power consumption, low-cost, scalable and covers around 100 m. The results of this study are important for future design of new indoor localization systems and scenarios. The future work will involve a finer analysis of the BLE 5.1 performance with the existence of obstacles.

3.6 Maritime localization system based on IoT

Localization-based services in the safety maritime domain are in the process of being ubiquitous, it is then essential to find a low-cost and effective solution for localization of moving targets that is efficient for indoor and outdoor scenarios. This chapter presents a maritime localization system for indoor and outdoor scenarios. The system is based on Bluetooth 5.1 and uses the incident angle of arrival and received signal strength indicator to locate a target equipped with a radio frequency tag. The system features a web service map that dynamically visualizes the radio frequency tag and the reference nodes. To demonstrate the feasibility, the system has been tested by running localization experiments. The experiments demonstrated that the system is efficient for indoor and outdoor scenarios (localization accuracy: 1.1 m for indoor localization whereas, 7.3 m for the outdoor scenario). The system is low-cost and can locate multiple moving targets while consuming 7 watts, opening interesting perspectives for efficient localization systems.

The evolution of wireless communication systems has promoted various applications that require user positions in various environments including indoor, maritime, and aerial environments. This progress also brought advances to wireless location tracking schemes for many purposes such as accident prevention, facility management, and military. The development of a safe evacuation and monitoring system of large passenger ships is a vital need for the maritime industry. Due to recent maritime disasters, a localization system that can be easily installed and monitored on both cruise ships and Search and Rescue (SAR) vessels is needed in order to simultaneously locate a larger number of passengers during emergencies. The existing rescue and localization systems that already exist in the market have many limitations e.g., localization accuracy, high power consumption, and high implementation cost.

Nevertheless, with the fast development of the IoT, there is a growing demand for indoor Location Based Services (LBS) that are also effective for outdoor scenarios. Most of the contemporary localization solutions either depend on Satellite Positioning Systems, SATNAV or passenger localization [157] or on a Wi-Fi network around the cruise ship where location data are sent in regular bursts [158]. The use of satellite positioning systems is restricted for outdoor scenarios and limited by the satellite coverage. Similarly, the use of a Wi-Fi network requires the placement of several static nodes around the cruise ship and has a limited coverage area. Other localization systems rely on risk-aware wireless positioning schemes, where the position information is required for safety [159]. Furthermore, a different approach to ensure maritime safety for ship passengers uses an overboard localization system based on measuring the Received Signal Strength Indicator (RSSI) between smart lifejacket tags and one interrogator station mounted inside an Unmanned Aerial Vehicle (UAV) [157]. Researchers also proposed an application that can localize the vessel who has launched a rescue request and to plan the most effective path for rescue assets [160]. Table 3.1 [161] presents a comparison of different localization techniques. It shows the specification of most available localization techniques.

Table 3.1: Comparison of Different Localization Techniques

Technique	Cost	Accuracy	Energy efficient	Hardware size
GPS	High	High	Less	Large
TDOA	Low	High	High	Less complex, may be large
APIT	Medium	Medium	High	Medium
RSSI	Low	Medium	High	Small
AoA	Low	Medium	Medium	Large

Many maritime localization solutions already exist in the market; however, it is important to find a low-cost and lowenergy solution for the localization of moving targets for both indoor and outdoor scenarios. Bluetooth-based (BLE)

solutions for localization have become increasingly popular in recent years. It has been studied intensively for localization and user tracking. Its low complexity due to the availability of RSSI measurements [155], low power consumption, low cost, and the ease of device deployment make it an attractive technology for localization.

In this section, a new localization system based on BLE 5.1 is presented. The system is based on measuring the Angle of Arrival (AoA) and RSSI to dynamically locate multiple targets. The system features a dynamic map visualization on a web service to monitor the target's location. In which it uses the MQTT communication protocol to transfer the localization data to the cloud database. With respect to previous systems presented in the literature [157; 159; 160] the proposed system is effective for indoor and outdoor scenarios. It is low-cost, has low power consumption, and is a standalone system that can locate multiple targets. The system could be extended to many other applications that require indoor and/or outdoor localization.

3.6.1 Localization Methods

BLE is a wireless communication protocol that covers range-based localization [154]; it is used to estimate the distance between a target sensor node and reference node(s). The new feature in BLE Core Specification version 5.1 makes it possible for BLE devices to determine the direction of an incoming BLE signal transmission (AoA); it is called the direction-finding feature. In addition, BLE 5.1 specification allows low-energy transmissions to sacrifice data rate for more range. In the current study, two localization methods are implemented.

Triangulation

Figure 3.11 illustrates the triangulation method used to locate moving and still target(s). The triangulation method is based on measuring the angles between two reference nodes and the RF tag. For that reason, it could be used only in the cases where two or more reference nodes are present in the range of the target tag.

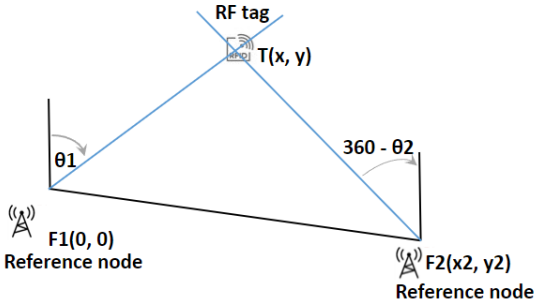

Figure 3.11: Triangulation

This method uses the Trigonometric laws to estimate the RF tag position, knowing that the reference node and the RF tag share the same elevation. The direction is known from multiple reference nodes to an RF target node. AoA is the measure of angle from the receiver (reference node) to the transmitter (RF tag). To locate the RF tag, trigonometric laws 3.10-3.11 are applied to find its coordinates x and y. Knowing the coordinates of two reference nodes F1, F2 (illustrated in Fig. 3.11) and the angles $\theta 1$ and $\theta 2$. The following equations 3.10-3.11 are used to determine the location of the RF tag.

$$y = \frac{y_2 \cdot \tan(\theta_2) - x_2}{\tan(\theta_2) - \tan(\theta_1)} \tag{3.10}$$

$$x = y \cdot \tan(\theta_1) \tag{3.11}$$

Unilateration

In the single reference node scenario (as shown in Fig. 3.12), the triangulation method is not capable of locating the target. For that reason, a new method is implemented. The unilateration method measures the AoA and RSSI from the reference node to the RF tag to locate the target. AoA is responsible for determining the target's direction. In Fig. 3.12, the AoA is θ angle, it is the difference between the orientation of the reference node (0 degrees) and the actual direction of the RF tag (θ). Trigonometric laws 3.12-3.13 are applied to find the coordinates of the RF tag. The distance between the reference node and the target is estimated by measuring the RSSI. The higher the RSSI value, the closer is the target. In Figure 3.12, the RSSI value which represents the estimated distance is indicated by the rho (ρ) symbol.

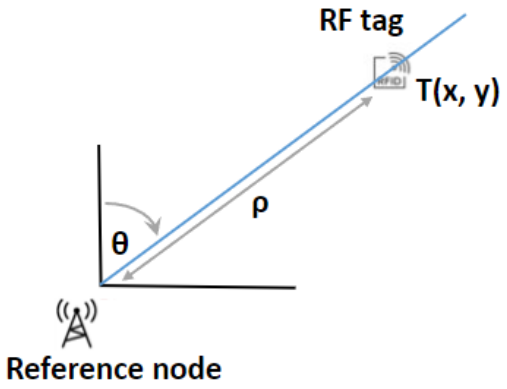

Figure 3.12: Unilateration

Assuming that the reference node and the RF tag are on the same elevation, trigonometric laws are applied to find the coordinates x, y of the RF tag, knowing the coordinates of the reference node and the relevant theta (θ), and rho (ρ). The following equations 3.12-3.13 are used to find the coordinates of the RF tag.

$$y = \rho \cdot \cos(\theta) \tag{3.12}$$

$$x = \rho \cdot \sin(\theta) \tag{3.13}$$

3.6.2 Proposed System Architecture

Figure 3.13 shows the block diagram of the developed system. The system uses the localization methods described earlier. The system includes:

- RF tag
- Baseboard and AoA antenna
- Raspberry Pi
- Data Management Cloud Architecture

The Raspberry Pi collects the localization data coming from the RF tag and computed by the AoA antenna and its mainboard. Then, the collected data are sent to an online dataset that visualizes the rescue vessels and RF tags on an online dynamic map.

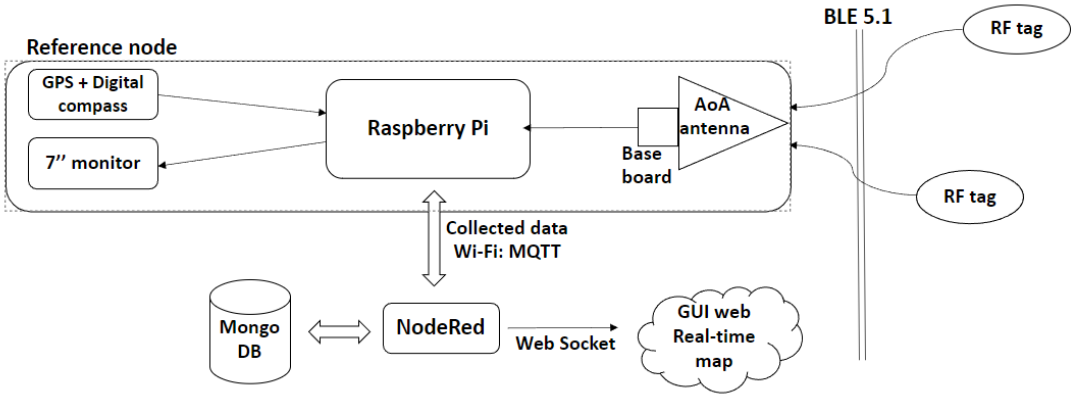

Figure 3.13: Block Diagram of the Proposed System

RF Tag

The RF tag is a multi-band CC1352R wireless MCU Launchpad Sensor Tag kit (LPSTK-CC1352R) (Texas Instruments, US) [150]. The kit offers integrated environmental and motion sensors, multi-band wireless connectivity, and easy-to-use software for prototyping connected applications. Using the kit, it is possible to create connected applications featuring BLE 5.1. The RF tag represents the target (wearable).

Baseboard and AoA Antenna

The localization system uses an antenna and a baseboard to determine the direction (AoA) and distance (RSSI) from its location to the target (RF tag). The hardware uses the AoA Booster Pack (BOOSTXL-AOA) [148; 149] as the antenna (Texas Instruments, US). The BOOSTXL-AoA board contains two orthogonal arrays, each with three dipole antennas. Each antenna array can theoretically cover an angle on the incoming signal up to $\pm 90^{\circ}$. When using both arrays, coverage of $\pm 135^{\circ}$ is achievable (the two antenna arrays overlap 45° on each side). The antenna is mounted on top of the baseboard CC26X2R (Texas Instruments, US) [149]. This board manages the data transfer from the antenna to the USB port. Both localization methods are developed and implemented in the CC26X2R board using C language.

Raspberry Pi

The Raspberry Pi is the heart of the system. It has many functionalities, and it has Raspbian OS installed on it. The Raspberry Pi reads and collects two incoming data streams from USB ports. The first is the AoA and RSSI data coming from the CC26X2R board (mounted by the AoA antenna). The second stream is the reference localization data coming from the attached BN-880 model.

This model has an embedded GPS and digital compass. This is needed in the system to locate the rescue boats and every moving rescue station. The GPS only exists on moving reference nodes. These data are then saved on the Raspberry Pi. This procedure is monitored by a seven inches monitor attached to the system. The collected data is then filtered, cleaned, saved, and sent using MQTT protocol to the cloud database using the Python 3.9 custom-developed firmware.

Data Cloud Piepline and Map

The process of sending the acquired data is done through the MQTT protocol. This protocol requires messages published on a hierarchical and free topic. The used topics nomenclature is: $username/ClientID$. The payload represents an update of the device's status. Two main types of payloads are defined. The first one is the payload of messages related to the localization data. This type of message is sent to the platform when an RF tag signal is detected. The second type of payload is the messages related to the position of the boat. This message is sent to the platform periodically by the boat to update its current position and bearing even if no RF tag is detected.

When a boat sends a message, it is registered on the database (MongoDB) in the collection of logged messages. If the localization message is from a previously logged RF tag, its situation will be updated. Otherwise, it will be added as a new RF tag that has been discovered. The database then subscribes to all messages received from the message broker (topic). A workflow implemented in NodeRed historicizes the message on the DB. Another workflow extracts some information from the received message, namely the ClientID of the device and the status update. The NodeRed platform then searches the DB for the registered device. If it already exists, it updates its status by integrating the new information received in the last message.

A management GUI that represents a dynamic map visualization for the registered devices is implemented to monitor the status and the messages received in real time. The GUI is updated in real time via WebSocket whose operating logic is implemented in a separate NodeRed workflow. The GUI was used to monitor the position of the boats and the RF tags.

3.6.3 Experimental Validation

A series of experiments is conducted to demonstrate the functionality of the system and the complete data pipeline. The experiments are divided into two parts. The first part is testing the functionality of the localization methods. The second part is an outdoor on-site experiment that is conducted in order to prove the functionality of the data pipeline from the RF tag to the visualization on the map. Testing scenarios are explained below.

Localization Method Validation

In this part, experiments using the AoA antenna, and one RF tag are presented. The target is to measure the accuracy of the AoA and RSSI values, which are the most important metrics for this system, to ensure localization quality. The testing protocol is presented in this part whereas the results are presented in the following section. Figure 3.8 shows the experimental setup where all the blocks are deployed on a common base structure.

Figure 3.14: Experimental setup: Indoor Scenario

In order to accurately assess the performance of the localization method, the experiments are divided into two parts. The first part is the assessment of the AoA localization. The second is the accuracy of the RSSI distance estimation. For each of the aforementioned parts, the antenna and target are in the line of sight without any obstacles in between. Both nodes operated with a full battery.

During the RSSI experiment, a user moves away from the testing platform to test the maximum indoor radio transmission range of the node. In addition, the RSSI value is measured every one meter along a thirty meters long hallway. RSSI data is collected for thirty seconds period. By averaging all the values obtained during this time, the valid RSSI at each testing location is calculated.

The experiment is carried out in a long corridor made up of two concrete walls as shown in Fig. 3.14. The RF tag was mounted for three different elevations with reference to the reference node. Elevation between the antenna and the target is an important factor that certainly affects the performance of the RSSI measurement. Thereafter, three scenarios were tested. For each scenario, several measurements are taken for each distance from one to thirty meters: Antenna higher than the target (1.5 meters difference) - Antenna lower than the target (1.5 meters difference) - Antenna and target on the same level.

The performance of AoA is tested in an indoor situation. These tests are conducted in a large empty closed room where the AoA antenna is positioned on a table, and a set of different angles orientations of the RF tag is tested. Those tests covered the 135 degrees range of the antenna. During the experiment, the AoA value was regulated every ten degrees for a five meters distance, each test lasting for 30 seconds. The valid AoA at each testing position was calculated by averaging all the values obtained during the 30 seconds. Each time the user changes the location of the RF target the system records and saves the measured data.

Pipeline Validation

In this part, the pipeline of the proposed system is validated by an experiment that is conducted in a similar environment to the real deployment scenario. The experiment was performed at the coast side of Chiavari, Italy. Two testing platforms were placed on the coast. The platforms should locate two RF tags that are in water. The data is then transmitted using MQTT to the database. Finally, it was presented on the dynamic GUI map. Both localization methods were tested. First the AoA and RSSI localization method was experimented using a single testing platform and a single RF tag. Then two testing platforms performed a

triangulation mesh to locate two RF tags.

Figure 3.15: Experimental setup: Outdoor Scenario 1

Figure 3.16: Experimental setup: Outdoor Scenario 2

Figure 3.17: Experimental setup: Outdoor Scenario 3

3.6.4 Experimental Results

The results of the experiments are presented in this section. The results are divided into two parts. The first one shows the results of localization methods experiments. These experiments happened indoors, as described in the previous Section. The accuracy of the AoA and RSSI values are the most important metrics for this system, to ensure localization quality. The second part presents the concluded evaluation metrics that were collected during the different experiments including the ones that happened outdoors in Chiavari, Northwest Italian Rivera. These experiments concluded the evaluation metrics thus the system specifications.

Localization Method Experimental Results

Figure 3.9 shows the average RSSI received along thirty meters of the indoor range. It shows three different lines, each represents an elevation value between the antenna and the target. The overall pattern of the three lines is decedent, as expected. Because the RSSI measures the received power level, and as the

distance goes higher, the RSSI decreases [157]. With reference to the AoA calculation, Figure 8 shows the AoA measured with comparison to the real angle. Red line is the one measured while the black line is the real angle. The RF tag was placed on the same elevation as the antenna. Each triangular point in Fig. 3.10 represents one of the twenty-one trials that was done for a certain angle; the incoming stream of data was collected for thirty seconds and averaged. The figure also shows a minimal error between the real and measured values of AoA for the 200 degrees measured range (AoA accuracy: 87%). This shows that the implemented AoA localization method is effective under the presented circumstances.

Evaluation Metrics Experimental Results

The accuracy of the localization methods in the outdoor scenario is calculated using a GPS (as a reference) that is close to the RF tag. Therefore, the measured accuracy error is the difference between the value given by the GPS and the one measured during the experiments (using either of the localization methods) in meters. The system uses around 1.4A of power with a 5V input (using a power bank). The price of one standalone system is around 112$. In addition, the duty cycle (i.e., the number of localization messages that are sent per minute) is measured. The measured latency is the time needed by the system to detect a new target that enters the coverage area. Finally, the coverage area of the system is measured in meters for both indoor and outdoor scenarios. These values have been measured for outdoor scenario and indoor scenarios. Table 3.2 summarizes the specifications of the developed system.

Table 3.2: Concluded System Specifications

	Accuracy(m)	Power(W)	Range(m)	Latency(s)	DutyCycle
Indoor	1.1	7	56	7	18
Outdoor	3.4	7	152	11	18

3.6.5 Conclusion

An indoor and outdoor maritime localization system is presented in this chapter. The system is based on Bluetooth 5.1 and uses the incident AoA and RSSI to locate a target equipped with a RF tag. The system uses the new BLE 5.1 localization feature based on AoA and RSSI methods. The system has been tested during different experiments that covered the indoor and outdoor scenarios. The results showed that the proposed system is reliable and capable of localizing multiple moving targets with 87% accuracy and an acceptable latency (9 seconds). The concluded system, with its relevant specifications, paves the way for interesting perspectives for an efficient localization system. Furthermore, this work will be extended by conducting more experiments in the goal of achieving a compact system design.

3.7 Patent and Proof of Concept Product

After the previous testing phases, a patent has been submitted and was granted. As a summary, the patent consists of the following points:

- Device for locating one of more targets in an environment
- Comprises a RF receiver
- Configured to detect RF signal emitted by beacon
- The receiver is configured to provide an assessment of:
  - Direction of reception of RF signal with respect to the main device
  - Distance to RF signal source with respect to the main device

3.7.1 Description of the Industrial Invention

Title: Device for locating one or more targets in an environment

The present invention relates to a device for locating one or more targets in an environment comprising a RF receiver configured to detect a RF signal emitted by said target. Advantageously, the device object of the present patent application provides the possibility of evaluating, preferably in combination:

- The direction of reception of the RF signal with respect to said device, said direction being established by evaluation of the Arrival Angle (AoA) of said RF signal
- The distance of said target with respect to said device, said distance being established by evaluation of the Received Signal Power Indicator (RSSI) of said RF signal

Advantageously, the said device object of the present patent application exploits the new Bluetooth 5.1 specifications. According to an embodiment, the said RF receiver is configured to receive / detect the RF signal emitted by the tag placed on the moving target; in particular, the RF signal is detected by the RF receiver when the RF signal passes over the at least two antennas of said antenna array.

Consequently, in the present patent application, with the term "evaluation of the arrival angle of said RF signal and power indicator of the received signal of said RF signal" or with the term "evaluation of arrival angle and power indicator Reference is preferably made to the data relating to the phase difference of the RF signal detected by the antennas of said receiver and to the power value (s) of the RF signal detected by the antennas of said receiver.

The power value of the signal detected by the antennas is variable according to the distance of the said target with respect to the said device; consequently, by means of a first calibration of the device, prior to the measurement aimed at locating the target, it is possible to proceed to correlate the possible distance values that may exist between target and device to determined values of received signal power. Said first calibration therefore consists in:

- Evaluate, in a phase prior to the actual localization, the maximum radio transmission range of the signal
- Progressively approach and / or move away a target to / from the device which is the subject of the patent application

CLAIMS OF THE PATENT:

Device (1) according to one or more of the preceding claims, comprising a processing unit (5) configured to provide a localization of target (2) with respect

to device (1) on the basis of the evaluation of the angle of arrival and of power indicator of signal detected by radio frequency receiver (3).

Device (1) according to one or more of the preceding claims in which processing unit (5) provides localization of target (2) following a previous first calibration of device (1), first calibration being configured to correlate the power value of the signal received by receiver (3) to a distance value of target (2) with respect to device (1).

Device (1) according to one or more of the preceding claims comprising first wireless or wired connection means (M '), means (M') being configured to provide a sharing of arrival angle evaluation and power indicator of the RF signal from the receiver (3) towards the processing unit (5).

Device (1) according to one or more of the preceding claims comprising a display (6) and second wireless or wired connection means (M "), display (6) being configured to provide a graphical representation in real time of the location of the target (2) with respect to device (1), location being shared to display (6) by processing unit (5) by means of second connection means (M ").

Device (1) according to one or more of the preceding claims comprising at least one hardware and / or software neural network (7) configured to evaluate the influence of external parameters in the localization of target (2).

Device (1) according to claim 7, wherein hardware and / or software neural network (7) is configured to perform evaluation on the basis of a previous second calibration by localization with GPS signal and / or triangulation system indoor.

Device (1) according to any one of the preceding claims of the portable type, being housed on a single frame provided with a handle (8) that can be gripped by a user.

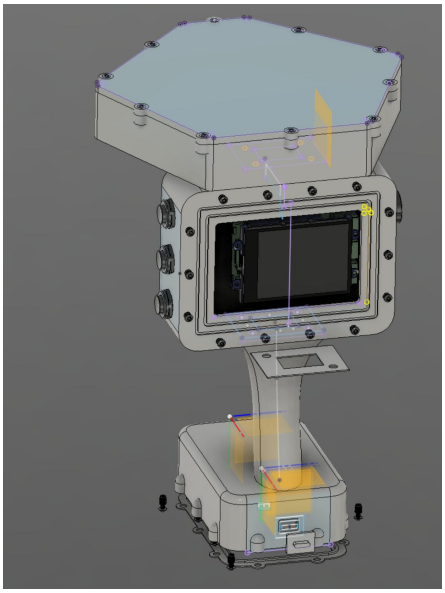

Figure 3.18: Proof of Concept Product 1

Figure 3.19: Proof of Concept Product 2

Figure 3.20: Proof of Concept Product 3

3.8 Summary and Conclusions

In-depth analysis of location-based services has been provided in this chapter. It is employed in both the public and private sectors to provide services. These include, among others, tracking services for the elderly and disabled, patient health monitoring, airport navigational services, traffic telematics, fleet management, inquiry and information services, crime fighting, toll systems, marketing, geographic mark-up, and community services.

In this chapter, a detailed approach to assess the feasibility of implementation of AoA and RSSI localization methods in real-world situations is implemented. Two proposed systems were detailed and discussed. These systems were tested in different environments (e.g., indoor, outdoor, in water...). Results showed that the localization capability is there but this method is limited to around 150 meters of distance for the antenna that we had, which is cheap. Therefore, depending on the use-case this method could or could not be beneficial.

I proposed a device (1) for locating one or more targets (2) in an environment comprising a RF receiver (3) configured to detect a RF signal emitted by target (2) characterized by the fact that receiver is configured to provide an evaluation of:

- Direction of reception of RF signal with respect to device
- Distance of target with respect to device

The receiver device, RF receiver, comprises at least one array comprising at least two antennas connected to each other, array being configured to provide an evaluation of the Arrival Angle (AoA) of signal at radio frequency and Indicator Power of the Received Signal (RSSI) of radio frequency signal.

Chapter 4

Real-time Target Monitoring using FMCW Radar

4.1 Summary

In this chapter, the use of the low-cost Frequency-Modulated Continuous-Wave (FMCW) radar is investigated. The goal of this application is to localize and monitor the real-time movement of a target in an indoor environment. The use of Deep Learning (DL) techniques is also taken into consideration to increase the performance of the proposed system. Two approaches were considered during this phase:

- Discriminating shadowed targets using FMCW radar

The radar shadow effect prevents reliable target discrimination when a target lies in the shadow region of another target. In this work, this issue is addressed in the case of FMCW radars, which are low-cost and small-sized devices with an increasing number of applications. A novel method is proposed. It is based on Convolutional Neural Networks (CNNs) that take as input the spectrograms

obtained after a Short-Time Fourier Transform (STFT) analysis of the radar-received signal. The method discerns whether a target is or is not in the shadow region of another target. The proposed method achieves test accuracy of 92% with a standard deviation of 2.86%.

- Multi-Class Action Recognition System Based on Deep Learning

In this work, we propose a low-cost edge radar-based action recognition system that uses Deep Neural Networks (DNNs), capable of recognizing falls among daily life actions in real-time. Range-Doppler maps, derived from five everyday actions performed in the Field of View (FoV) of the radar, are fed into a novel Neural Network (NN) architecture that is deployed on an edge device. The results show that the proposed system can recognize the five actions with an accuracy of 93.2% with real-time edge inference. Concerning the problem of binary classification, i.e. falls vs non-falls, our method achieves an accuracy of 96.8% while maintaining a low false-negative rate. The Energy Precision Ratio (EPR) is a guideline for both accurate and energy-efficient models for edge deployment. The best trade-off achieves a 1.04 EPR

4.2 FMCW Radar Use Cases

In the recent years, the radar technology, once used predominantly in the military, has started to emerge in numerous civilian applications. One of the areas that this technology appeared is the Real-Time Localization Services (RTLS).

On construction and industrial sites, technology for estimating the placement of targets in enclosed spaces has been researched for ease and accident avoidance. As part of the fourth industrial revolution, indoor localisation systems are also being developed [162; 163; 164]. An indoor localization system, for instance, can avoid mishaps by determining the worker's location and alerting them if they attempt to enter a hazardous area. Additionally, a new manufacturing trend identified human-robot collaboration, in which human employees and robots combine their expertise for flexible manufacturing [165]. However, it is believed that the implementation of safe human-robot collaboration requires the use of an indoor localization system.

Indoor localization systems employing radio signals, such as Wi-Fi, Zigbee, RFID, Bluetooth, Ultra-Wide Bandwidth (UWB) radar, and frequency-modulated continuous wave (FMCW) radar, have been developed because a global navigation satellite system is not accessible indoors [166; 167; 168; 169; 170; 171; 172]. The multilateration approach and the fingerprint method, which employ radio signals like Wi-Fi, Zigbee, RFID, and Bluetooth, are both well-known localization strategies. The effectiveness of the multilateration method's localization depends on how well the target's distance is measured because it is reliant on range estimation [173]. The fingerprint approach, on the other hand, collects the received signal intensity of radio signals at all places of interest, and then correlates the real-time data at a particular spot with the precollected data to estimate its location [174]. The range and localization accuracy of Wi-Fi, ZigBee, and Bluetooth-based multilateration and fingerprint localization techniques

are known to be less accurate than those that employ radars, which offer high temporal resolution for calculating distances and positions [172; 175; 176; 177]. It is also known that the UWB radar has less coverage than the FMCW radar, which determines the target's distance by computing the difference between the transmission and reception frequencies caused by the time delay [178]. Indoor localization using FMCW radars is introduced with various bandwidths (e.g., 24 GHz, 77 GHz, etc.), and the performance varies depending on the frequency band. The hardware is often adjusted to improve target detection accuracy with high bandwidth.

4.3 Hardware Components

The hardware components utilized in the creation of the suggested systems are described in this section. The hardware elements and the means of connecting them are discussed first. The generated software's operational logic and the specifics of each of its processing units are then illustrated.

The proposed system are mainly based on the FMCW radar: Position2Go by Infineon [179]. The radar device is based on a demo board developed by Infineon, which is composed of two parts:

- Radar main board
- Debugger board

The transmitting and receiving arrays of microstrip patch antennas on the radar main board each have a 12 dBi gain with 20° 40° beamwidths. The radar transceiver is a BGT24MTR11 device (defining in this way the Field of View, FOV). On the same PCB are integrated the antennas that are used for electromagnetic field transmission and reception (dedicated to the two channels). These antennas, in particular, are planar arrays made up of 4 2 elements (rectangular patch antennas).

A frequency control component is also included on the board to regulate the timing and quantity of sent chirps. A quadrature down-conversion mixer and an analog amplification component for signal filtering and amplification are also present in the receiving stage. Last but not least, it includes an XMC4200 microcontroller that manages every aspect of the radar board's operational functioning. In particular, it controls data transmission between the board and the computer and may be used to carry out basic online signal processing operations (provided that a proper firmware is adopted).

The developed solution makes advantage of the board's default firmware, which allows it to just record raw radar data without performing any extra processing. On the control PC, MATLAB has been used to implement each processing chain, including the FMCW radar processing. Through a USB connection, serial communication is used to communicate between the PC and the radar board. The XMC microcontroller may be programmed using the debugging board.

4.3.0.1 Radar Module Configuration Parameters

The following radar module settings have been predetermined by the manufacturer and cannot be changed (except for changes to the XMC software and/or board circuits):

$$\begin{aligned} T_{rd} &= 200\mu\text{s} \\ T_{pll\_s} &= 400\mu\text{s} \\ M &= 6144 \text{ byte} \\ P_{\text{out,max}} &= 10\text{dBm} \end{aligned} \tag{4.1}$$

T_{rd} is the interval between the transmitted up-chirp and the down-chirp (an abrupt transition from the maximum frequency of the up-chirp to the minimum frequency of the subsequent up-chirp can cause various problems including the generation of spurious signals). T_{pll_s} is the recovery time (steady-state time) required by the PLL before generating the next up-chirp. M is the memory available to the microcontroller ADCs to digitally store the radar echo. $P_{\text{out,max}}$ is the maximum transmitted power. It is important to note that no data samples are collected during the T_{rd} and T_{pll_s} periods.

The following parameters, in contrast to the values shown above, may be changed by sending commands to the board via the serial interface; however,

if they are set to values other than those reported and deemed optimal by the manufacturer, they may cause a significant deviation of the digitized signal from what is suggested by the theoretical models relating to the operation of FMCW radars:

$$\begin{aligned} T_c &= 1500\mu\text{s} \\ B &= 200\text{MHz} \end{aligned} \tag{4.2}$$

Where, T_c is the duration of the up-chirp and B is the relative band. In particular, the frequency modulation covers the frequency range $[f_0,\ f_0 + B]$ with f_0 = 24.025 GHz. The theoretical resolution that can be achieved for measurements of the radar-target distance (range) may be calculated using the band value:

$$\Delta R = \frac{c}{2B} = 75 \text{ cm} \tag{4.3}$$

where c is the speed of light in vacuum.

In addition, to have a maximum unambiguous detection distance of the targets equal to R_{max} = 25 m, an appropriate number of samples N_s equally spaced over time must be selected with which to digitize the radar echo based on the following relationship:

$$N_s \geq \frac{4BR_{\max}}{c} = 67 \tag{4.4}$$

The decision was made to adopt a number of samples equal to a power of two, or $N_s = 64$, while accepting a minor reduction in the maximum achievable distance. This was done in order to optimize the execution of the FFTs that are required for the processing of the received signal. In fact, it is not feasible to adopt the next two power (128) since this would result in issues with the constrained memory on the XMC, such as the drastic reduction in chirps per frame (N_c)

between 24 and 12, which would impair the Doppler spectrum resolution.

Additionally, adopting $N_s = 128$ would suggest an unreasonably large upper bound on the energy range (also known as the instrumental range) [180], i.e., bigger than the greatest distance actually detectable by the radar given the emitted power and that reflected by the target.

The numbers shown above meet the crucial requirement that:

$$T_c \geq \frac{2R_{\max}}{c} \tag{4.5}$$

In order to prevent ambiguity in the interpretation of the demodulated signal, it is necessary that the duration of the up-chirp be longer than the maximum round-trip time, or the time it takes the electromagnetic wave to travel to a target placed at the maximum distance before returning to the antenna.

Due to the limited memory availability of the microcontroller, the number of chirps transmitted and collected in a single frame is equal to $N_c = 24$. In the first implementation of the system, due to some limitations in the interface of the Raspberry mini-PC with the control PC, this number was reduced to $N_{c,eff} = 21$. This value implies the following performances relating to the radial velocities directly observable by the Doppler component of the radar echo:

$$\begin{aligned} |v_{r,\max}| &= \frac{\lambda_0}{4T_{PRT}} \cong 5.3\frac{\text{km}}{\text{h}} \\ \Delta v_r &= \frac{\lambda_0}{2T_{CPI,eff}} \cong 0.53\frac{\text{km}}{\text{h}} \end{aligned} \tag{4.6}$$

where $|v_{r,\max}|$ is the maximum absolute value of the detectable radial speed. $T_{PRT} = T_c + T_{rd} + T_{pll\_s}$ is the Pulse Repetition Time (PRT). λ_0 is the wavelength in vacuum. The complete set of radar sensor parameters are presented in Table 4.1

Symbol	Description	Value
B	Sweep Bandwidth	200MHz
f_0	Center Frequency	24.025GHz
f_s	Sampling Frequency	42667 Hz
$R_{\max}$	Maximum Range	25 m
$V_{\max}$	Maximum Velocity	5.4Km/hr
ΔR	Range Resolution	0.75 m
ΔV	Velocity Resolution	0.4Km/hr
N_s	Number of Samples/Chirp	64
N_c	Number of Chirps/Frame	21
T_c	Up-Chirp Time	1.5 ms
a	Chirp Slope	133MHz/s
T_{PRT}	Pulse Repetition Time	2100μs

Table 4.1: Radar Sensor Parameters

4.4 A CNN-Based Method for Discriminating Shadowed Targets in FMCW Radar Systems

Up to now, the bi-static radars (with at least one transmitting antenna and at least one receiving antenna) have resolved the detection and localization of a single stationary target, yet the problem of multi-stationary target detection has been less addressed. The bi-static radars are able to accurately detect targets that are closer to the radar antennas, whereas the greater the distance of the targets from the radar, the lower the accuracy of the detection [70]. This is mainly attributed to two factors. Firstly, as the transmission distance increases, the energy of the electromagnetic wave is attenuated; hence, the energy of electromagnetic waves reaching farther targets is inevitably smaller than that reaching the closest target.

Secondly, some targets, named recessive targets, can lie in the shadowed region of a dominant target (i.e., the closest to the radar). Thus, because the highest energy of the electromagnetic waves is reflected from the dominant target to the radar, the electromagnetic illumination of the recessive targets could decrease to the point where they are not detected [71]. Therefore, radar systems suffer from what is called the shadowing effect. This effect occurs when two targets stand in front of the antenna, one in the shadowing region of the other. The radar is usually not reliably capable of detecting the target that is standing in the shadow region [70]. This problem is common for most radar technologies, particularly, Ultra-Wide-Band (UWB) radar [74] and Frequency-Modulated Continuous-Wave (FMCW) radar [90]. Unlike pulse and Ultra-Wide-Band (UWB) radars, FMCW systems require lower sampling rates and lower peak-to-average power ratios to detect the distance and speed of multiple moving targets [30; 31]. Accordingly, the FMCW radar is a good solution for detection and localization purposes but

performs poorly whenever the shadow effect occurs. The shadow effect is more relevant in low-cost radars. This is due to their lower resolution compared to the high-end radars (higher range and velocity resolution) [91].

This section is organized as follows: In Section 4.4, the problem statement is explained. Section 4.4.2 presents and discusses the methodology adopted to identify and solve the shadowing effect. The experimental setup is considered in Section 4.4.3, explaining the data acquisition process, time frequency analysis, and training process. The experimental results and discussion are presented in Section 4.4.4. Finally, the conclusions and some proposals for future work are provided in Section 4.4.5.

4.4.1 Problem statement

4.4.1.1 FMCW radar device

Multi-chirp FMCW algorithm is considered the standard for detecting and measuring range and speed of multiple targets [28]. The concept of multi-chirp is to send a frame containing multiple number of chirps (Nc) in saw-tooth modulation and in a short period, with a chirp time (Tc) being very small (in μs), where Tf is the time of the data frame (Tf is in ms). In the current scenario, the "Position2Go" [181] cheap radar is used. It is an FMCW radar board developed by Infineon technologies. This development kit allows the user to implement and test several sensing applications at the 24 GHz ISM band such as tracking and collision avoidance. This is possible by using fast chirp FMCW and two receive antennas to get the angle, distance, speed, and direction of motion. The radar is equipped with a pair of arrays of microstrip patch antennas (one transmitting and two for receiving) characterized by a 12 dBi gain and 19 $\times$ 76 degrees beamwidths, defining the Field of View (FoV). The kit consists of the BGT24MTR12 transceiver MMIC and a XMC4700 32-bit ARM® Cortex®-M4 for signal pro-

cessing and communication via USB. The radar is connected via USB to a PC that is running MATLAB. A MATLAB script sends the order to the radar to initiate the data acquisition procedure through USB port. Table 4.6 shows the radar sensor parameters.

Table 4.2: Position2Go radar specifications.

Parameters	**Value**
Sweep Bandwidth	200 MHz
Center Frequency	24 GHz
Up-Chirp Time	300 μs
Number of samples/chirp (Ns)	128
Number of chirps/frame (Nc)	32
Maximum Range	50 m
Maximum Velocity	5.4 km/h
Range Resolution	0.75 m
Velocity Resolution	0.4 km/h
Sampling rate	42 KHz

4.4.1.2 Shadow effect

Figure 4.1 shows different cases of targets detection using a radar. In particular, Figure 4.1(a) illustrates the case of a single target standing in the range of the radar, Figure 4.1(b) depicts two targets both detectable by the radar, while Figure 4.1(c) represents the shadowing effect where the target B is masked by the target A, thus target B is not visible to the radar. Figure 4.2 shows a photograph of the measured setup where one target is in the range of the radar.

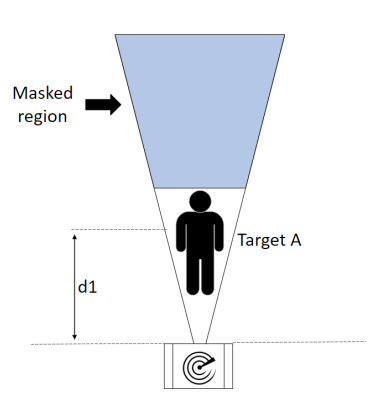

(a) One target in range of the radar

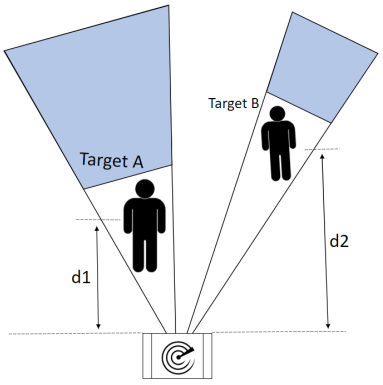

(b) Two targets in range of radar, both visible to the radar

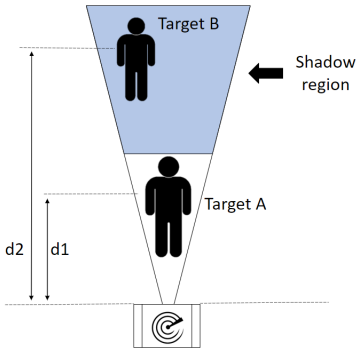

(c) Two targets in range of radar, only one visible to the radar

Figure 4.1: Illustration of the data collection setup

Figure 4.2: Photograph of measured setup - One target in range of the radar

The shadowing effect creates a region behind the target (Target A in Figure 4.1(c)) where the electromagnetic waves emitted by the radar transmitting antenna or reflected by another object are not able to propagate. In fact, computing the power spectrum on the multi-chirp data acquired by the FMCW radar, it is possible to detect the masked target, but the detection is accompanied with a lot of variability in the measurements. The reason of such variability is that a few radar waves penetrate and slips through the shadowing target to the masked one, reflecting to the radar with a very low intensity. These waves in particular cause a huge variability that can affect the detection parameters of both targets in the Field of View (FoV) of the radar. Figure 4.3 shows three examples of the range

representation obtained after the fast time FFT (range-FFT) on multi-chirp signals [28], positioning the radar 1.5m from the floor. Each target on the spectrum is represented by a peak. A fixed target detection threshold (red horizontal line), is used to determine the valid target identifications, i.e., each target passing in the FoV of the radar with a peak higher than the fixed threshold is considered a valid detection by the radar. The threshold is a user-defined parameter that affects radar performance directly by causing a trade-off between detection accuracy and false alarm probability. If it is chosen to be too high, the algorithm will fail to identify some targets. If it is too low, the algorithm will detect many artifacts as targets. Figure 4.3(a) shows only one peak at a distance of 7m, this situation is illustrated in Figure 4.1(a) where only one target is in front of the radar ($d1 = 7m$). In Figure 4.3(b), two peaks appear at distances of 7m and 10m, respectively; this spectrum is the result of a trial where two people were standing in different positions (i.e., $d1 = 7m$ and $d2 = 10m$) with no shadow effect on each other, as illustrated in Figure 4.1(b). The magnitude of the peak at a 10m is smaller than that at 7m because of the attenuation of the electromagnetic wave of the radar as the distance increases. In Figure 4.3(c), the maximum peak appears at a distance of 7m, which corresponds to the location of target A ($d1 = 7m$). However, target B ($d2 = 10m$) cannot be detected, since he stood in the shadowing region. An example is illustrated in Figure 4.1(c).

Therefore, the traditional spectrum method is not reliable for detecting multiple targets where the shadow effect occurs. The shadowed targets are hardly detected. This fact is dependent on the chosen power threshold, Radar Cross Section (RCS) of the shadowing target [182], and the environmental clutters.

In the case when target B is not fully shadowed by target A, target B is expected to be detected with a weak signal, based on how much it is shadowed by target A. However, this detection is also relative to the chosen detection threshold.

The radar is capable of discontinuously detect Target B when it is not completely aligned with Target A [70]. Although, the detection of Target B is not reliable, the partial shadow effect was excluded from our testing campaign because it represents a simplified version of the full shadow effect illustrated in Figure 4.1(c).

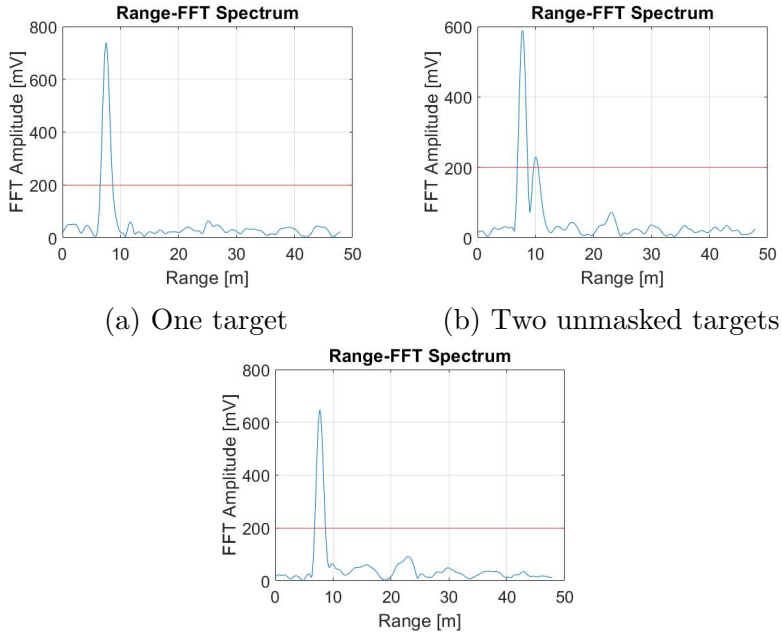

(a) One target (b) Two unmasked targets

(c) Two targets, one masked

Figure 4.3: Range-FFT power spectrum

The horizontal red line is the target detection threshold. Radar is positioned 1.5m from the floor. (a) Only Target A ($d1 = 7m$), (b) Two targets A ($d1 = 7m$) and B ($d2 = 10m$) without shadowing effect, (c) Target B ($d2 = 10m$) is shadowed by Target A ($d1 = 7m$)

4.4.2 Methodology

To address the shadow effect, a novel approach is proposed. The idea is that a slight portion of the waves are slipped through or around the shadowing target (Target A in Figure 4.1(c)) towards the shadowed target (Target B in Figure

4.1(c)). The masked target is receiving and reflecting those slithered electromagnetic waves, thus making a slight but noticeable variation in the waves received by the radar. Those reflections are used to identify whether there is a masked target or not. This goal could be achieved using time frequency analysis to construct images (i.e. spectrograms) that feed CNNs, addressing a two class image classification problem (One Target vs Two Targets).

4.4.2.1 Time frequency analysis

Spectrograms are a popular signal processing tool used to reveal the instantaneous spectral contents of the time-domain signal. They also show the variations of the spectral content over time. A spectrogram is obtained by applying the squared magnitude of the STFT computed over a discrete input signal. The STFT can be formalized as:

$$STFT\{x[n]\} = X(m,k) = \sum_{n=-\infty}^{\infty} x[n]w[n-m]e^{-j2\pi kn/N} \tag{4.7}$$

where $x[n]$ is the discrete signal, $w[n]$ is the discrete window function, which is non-zero in $[0...N]$ and zero elsewhere, N is the number of samples in the window, and k is the discrete frequency. The window's location is indicated by the index m. The spectrogram can be generated by continuously computing the STFT with increasing m by a step size Δm. The step size Δm can be used to achieve an overlap between two consecutive analysis windows, resulting in a smoother time dimension output. Eventually, to use the computationally quicker Fast Fourier Transform (FFT), a power of 2 must be selected for N, or N can be zero padded to a power of 2. As a rule of thumb, large window size indicates a high resolution in the time domain and low resolution in the frequency and vice versa.

4.4.2.2 Deep Neural Network Models

To address the shadowing effect problem in its most simplified form, only two classes were considered in this study (One Target and Two Targets). To address the two class classification problem, we employed CNNs trained over the spectrogram images. The CNNs proved to be very efficient in images classification. In particular, MobileNet models are suitable for the deployment on embedded systems since they achieve similar accuracies in the object classification problem, while requiring less parameters than ResNets and VGGs. The peculiarity of the MobileNets is the adoption of the depth-wise separable convolution [183], i.e., the standard convolution operator is replaced by two separate layers: the first layer involves one convolutional filter per input channel, while the second is a point-wise convolution. For an input of size $H \times W \times D$, and a 2-D convolutional layer presenting N_k kernels of size $K \times K$, the computational cost C_{SC} of the standard convolution is:

$$C_{SC} = H \times W \times D \times N_k \times K \times K \tag{4.8}$$

while using the depth-wise separable convolution, the cost C_{DSC} is:

$$C_{DSC} = H \times W \times D \times (K^2 + N_k) \tag{4.9}$$

which is significantly smaller than (4.8).

Table 4.3 shows a comparison of some state-of-the-art MobileNet models (i.e., V2 and Small V3) with ResNet50 and VGG19 networks [184], all trained on the Imagenet dataset. The first column reports the models, the second represents the number of parameters, the third shows the generalization accuracy on the Imagenet dataset, the fourth displays the model sizes in megabytes, while the last column presents the average inference time of the models running on GPU Tesla

A100. The table demonstrates that the MobileNets can achieve similar generalization performances, employing few parameters with respect to more complex models.

Table 4.3: Sample of the available models.

Model	Num of params (Million)	Top-1 accuracy (%)	Size (MB)	Inference Time (ms) on GPU
ResNet50	25.6	74.9	98	4.55
VGG19	143.6	71.3	549	4.38
MobileNet_V2	3.53	71.3	14	3.83
Small MobileNet_V3	2.0	73.8	12	3.57

Following the results of Table 4.3, four different MobileNet-based architectures were compared. The four models were pre-trained on the Imagenet dataset, thus the weights and biases have been statically loaded, before eventually fine-tuning the last trainable Dense layer using the collected dataset. Hence, the convolutional layers of the MobileNets provide the filters, learned on the Imagenet dataset, to process the input image. Eventually, the features extracted by the convolutional layers are fed to the Dense layer that classifies the data among the two possible classes (One target vs Two targets). The data collection procedure is presented in Section 4.4.3.1.

4.4.3 Experimental setup

Four persons were involved in a series of experiments with the aim of collecting data to validate the proposed solution. In the following section, the data retrieval process is described. In addition, the spectrograms hyperparameters choice is explained. Finally, the CNN training phase is spelled out. The block diagram of the proposed system is illustrated in Figure 4.4.

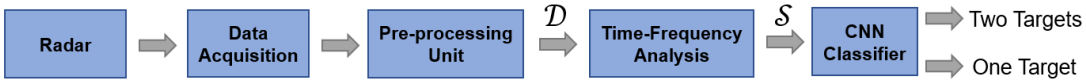

Figure 4.4: Block diagram of the proposed system

4.4.3.1 Data acquisition

In order to overcome the possible problem of multi-path effect, a clutter removal technique proposed in [92] was used to cancel the environmental clutters (i.e., the potential ghost effect) from the source.

Two sets of experiments were carried out for this study. Measurements took place in thirty meters long and three meters wide corridor. The corridor environment was chosen because it maximizes the clutter, thus makes it harder for the radar to detect the shadowed target. The goal of the experiments is to detect all human targets standing in range of the radar. The radar was placed one and a half meters from the ground. Figure 4.5 schematizes the experimental environment.

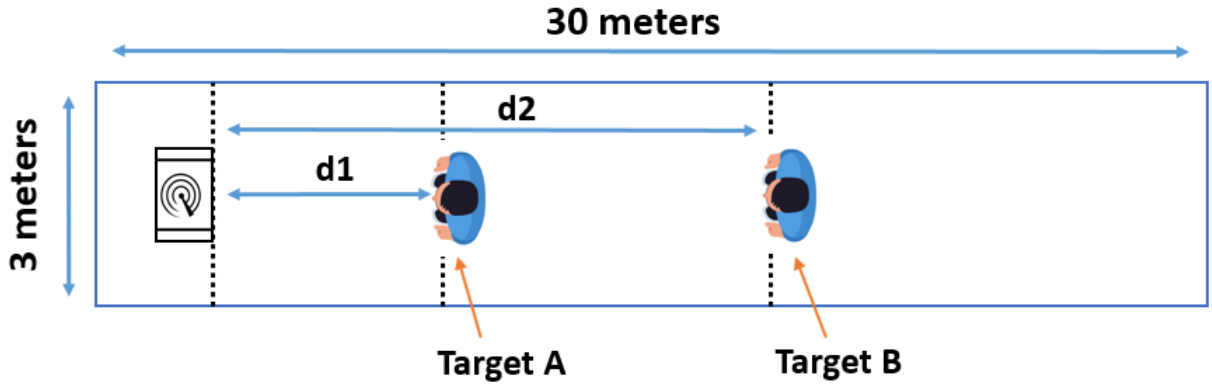

Figure 4.5: Illustration of the corridor data collection environment

As illustrated in Figure 4.4, data is collected and pre-processed to reach a spectrogram format (i.e., image). These spectrograms are then fed to the CNN classifier. Figure 4.6 shows the data processing pipeline from the raw radar out-

come towards the spectrogram format. The data corresponding to chirps are stored as the rows of a matrix of dimension $Nc \times Ns$ (i.e, Nc is number of chirps and Ns is the number of samples of each chirp). To convert the data type, an Analog to Digital Converter (ADC) was used. Range FFT is then applied on each row, it results in a range representation. Multiple slices ($Slices = 50$ in this study) of this matrix are then collected to form a tensor ($Nc \times Range \times Slices$). The slices are collected consecutively: as soon as the $n-th$ slice is collected, the radar immediately starts to collected the slice $n-th+1$. Finally, STFT is applied on this 3D tensor to obtain the spectrogram.

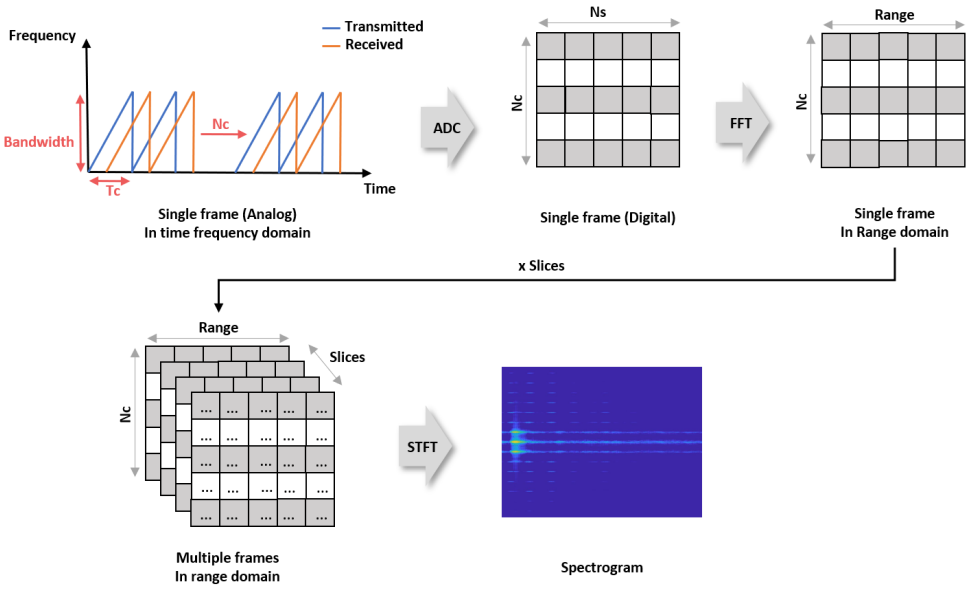

Figure 4.6: Data processing pipeline

For the first experiment, illustrated in Figures 4.1(a), a single target (Target A) stood in the range of the radar. The target was standing in different positions gradually through all reference positions $d1$ along eleven meters range. Four different human targets were involved in this experiment to increase the data diversity. One hundred and fifty measurements were collected for each target. Therefore, for the first experiment, six hundred measurements were collected.

This dataset is called: One Target (OT) class.

For the second experiment, illustrated in Figure 4.1(c), two targets A and B stood in the range of the radar. Target A, who was closer to the radar antennas, was standing gradually through all reference positions $d1$ along eleven meters range in front of the antennas, and target B who was farther away from the antennas stood in the shadowing region of target A (setup is illustrated in Figure 4.1(c)), two meters behind him. Three persons were involved in this experiment, exchanging their mutual positions. Six hundred measurements were collected during this experiment; this dataset is called: Two Targets (TT) class. To sum up, the complete collected dataset consists of one thousand and two hundred samples. Divided in half among the two classes. The extracted dataset is formalized in:

$$\mathcal{D} = \{(\mathcal{X}, y)_i;\ \mathcal{X}_i \in \mathbb{R}^{Nc \times Ns \times Slices},\ y_i \in \{OT, TT\}; i = 1, ..., Z = 1200\} \quad (4.10)$$

where $Nc = 32$, $Ns = 128$, and $Slices = 50$.

Table 4.4 summarizes the data collection setup. The first column represents the class (One Target vs. Two Targets). The second and the third columns presents the distances from each target to the radar (i.e., Target A and Target B respectively). The last column displays the number of measurements acquired for each combination of the targets involved in the experiments. In case of the One Target class, 4 persons have been involved (i.e., four combinations for each $d1$ distance), thus 30 acquisitions per combination. For the Two Targets class, measurements have been obtained on 3 persons exchanging their mutual position (i.e., 6 possible combinations for each pair $[d1, d2]$), hence 20 acquisitions per combination.

Table 4.4: Data collection Setup

Class	Distance of Target A ($d1$) [m]	Distance of Target B ($d2$) [m]	Num of meas. per comb.
One Target	3	-	30
	5	-	30
	7	-	30
	9	-	30
	11	-	30
Two Targets	3	5	20
	5	7	20
	7	9	20
	9	11	20
	11	13	20

4.4.3.2 Spectrogram

Accordingly to Section 4.4.2.1, a time-frequency analysis is carried out on $\mathcal{D}$ to extract spectrograms in order to feed CNNs. To obtain a continuous spectrogram, a large window size was chosen with N = 2048, with a 50% overlapping ($\Delta m = 1024$). Two samples of the obtained results are illustrated in Figure 4.7.

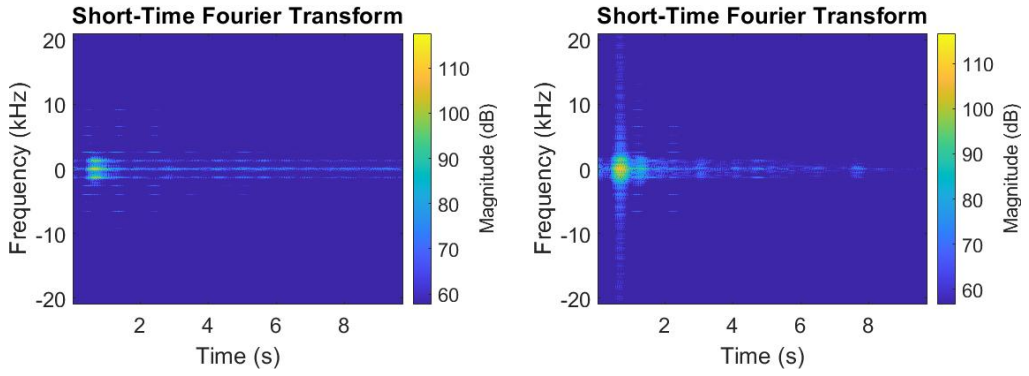

(a) One Target. (b) Two Targets.

Figure 4.7: Spectrogram examples

The spectrograms of the 1200 collected samples are generated. The original dimensions of each spectrogram was (875, 656, 3); each down-sampled and zero

padded to fit the input size of our CNN, with the dimension (224, 224, 3). The dataset containing spectrograms can be formalized as:

$$\mathcal{S} = \{(\hat{\mathcal{X}}, y)_i; \hat{\mathcal{X}}_i \in \mathbb{N}^{224\times224\times3},\ y_i \in \{OT, TT\}, i = 1, ..., Z = 1200\}. \quad (4.11)$$

Figure 4.7(a) shows an example of the generated spectrogram for the One Target class as illustrated in Figure 4.1(a). In this example, the target was standing five meters away from the radar. Figure 4.7(b) shows an example for the Two Targets class as illustrated in Figure 4.1(c). In this example, the Target A was five meters away from the radar while Target B was two meters behind target A, so seven meters away from the radar. If inspected carefully, a difference is visible between Figure 4.7(a) and 4.7(b), this difference represents the passive electromagnetic waves reflected from the Target B and received by the radar antenna.

4.4.3.3 Training

In line with the outcomes shown in Table 4.3, MobileNet-based architectures delivered outcomes on par with those of other neural networks with significantly more parameters. Therefore, the author adopted the four most common implementations of the MobileNets architectures. The number of neurons in the trainable Dense layer is set to 128 for each network, using the ReLU as non-linear activation function. Moreover, Stratified K-Fold technique was adopted to ensure fair results. Stratified sampling consists of splitting the data of the original labeled dataset (i.e., the population) in subsets, having the same proportion of data as in the population. The subgroups are called 'strata'. Thus, by adopting the stratified method in cross-validation guarantees that the training and test sets contain the same proportion of labeled dataset in each fold, leading to a close approximation of the generalization error on the test set. In each of 'K' iterations

of the K-fold cross-validation technique, where the data have been split into 'K' groups, one portion is used as the test set, while the remaining portions are used for training. In the current situation, 'K' was chosen to be equal to five. Therefore, five folds were generated, and results will be presented in the next section as an average of the five results from each of the folds. In this way, 80% of the data have been used for training and 20% for test in each iteration run. Actually, the test data has been split into two parts (validation and test sets) having the same number of samples. An early stopping criterion was implemented during training over the validation set, fixing the patience parameter to 10. All the results have been averaged over the 5-folds. The Adam optimizer function is used with a learning rate of 1/2000. Regarding the loss function, categorical cross entropy is used. Models are trained for one hundred epochs for each split.

4.4.4 Experimental results and Discussion

The results achieved using the proposed approach are presented in Table 4.5. The first column provides the four adopted model architectures, the second shows the number of parameters, the third column reports the average accuracy computed on the test set of the 5-folds and the standard deviation for each model, the fourth column depicts the average inference time of the model running on a RTX-2080Ti GPU, while the last column presents the saved models sizes.

Table 4.5: Results over the four different models

Model	Num of params (Million)	Average test acc (%) ± STD	Inference Time (ms) on GPU	Size (MB)
MobileNet_V2	2.3	81.5 ± 4.36	2.35	7.2
MobileNet_V3 Large	3.2	92.2 ± 2.86	2.23	18.2
MobileNet_V3 Small	1.6	90.9 ± 1.4	1.91	6.8
MobileNet_V3 Small Minimalistic	1.06	88.7 ± 2.39	1.64	5.0

The table shows that all the MobileNet_V3 based networks generally perform better than MobileNet_V2. It could be explained by the introduction of the hard-swish activation function and the implementation of a squeeze-and-excitation module [183]. Among the three MobileNet_V3 versions (Large, Small, and Small Minimalistic), testing accuracy results are directly proportional to the number of parameters used in the architecture: the higher the number of parameters, the higher testing accuracy is achieved.

A compromise should be taken when choosing the model. This compromise would be highly dependent on the application scenario. If the application scenario is critical and the accuracy is the main interest, Large MobileNet_V3 would be chosen. If the goal is to deploy on the edge, then memory and inference time would be the main goal, Small Minimalistic MobileNet_V3 would be chosen. Usually, the main interest of using a low-cost radar is the possibility of edge deployment, and the main constraint of edge deployment is the number of parameters, thus the model size. Therefore, the Small Minimalistic MobileNet_V3 best suits the proposed use-case.

Under the proposed circumstances, where either one or two targets are in the detection range of the radar, the model's choice (i.e., number of parameters,

architecture, etc.) affects the performance of the proposed algorithm. In addition, the radar parameters and hardware specifications (i.e., Number of chirps, memory capacity, etc.) influence the performance of the algorithm; those parameters were chosen according to [181].

As introduced in the Section 4.4, authors in [74] proposed an algorithm based on the wavelet entropy for shadowing effect removal of human targets using UWB radars. This method proved to be effective in detecting two stationary human targets despite one person being in the shadowing region of the other. Hence, static filters (i.e., wavelet) are used. For each new possible deployment environment, an on-site adjustment is required: the number of filter levels and the wavelet function need to be tuned to accurately fit the application scenario. Therefore, the solution is not easily scalable because it needs an expert intervention whenever a new context occurs. On the other hand, our proposal uses filters (i.e., weights of the Convolutional layers) learned on a massive dataset (i.e., Imagenet dataset). This guarantees a high level of scalability and ease of deployment for different environments. Particularly it is not required to retrain the filters for new problems: only one Dense layer needs to be fine-tuned for the incoming dataset, preserving the same structure of the pre-trained architecture, without requiring any expert intervention.

4.4.5 Conclusion and Future works

In the case of multi-target detection using an FMCW radar, the target closest to radar antennas partially reflects the energy of the electromagnetic wave, the person farther from the radar antennas is not detected continuously, especially when in the shadowing region of the closest person. In this chapter, a novel solution for the radar shadowing effect has been proposed. The solution is based on a CNN model that classifies the spectrogram images, obtained after a time-

frequency analysis of the radar data, among one of two classes: One Target vs. Two Targets. The model is based on MobileNet and is loaded with the Imagenet weights. The best solution in terms of testing accuracy achieved 92.2% with a standard deviation of 2.86%. Whilst the lightest (i.e., 1.06 million parameters) model attained 88.7% with a standard deviation of 2.39% over five splits of input data. The latter model uses 1.06 million parameters only and having a size of 5 MB. The inference time using a GPU is 1.64ms. In future research, the authors plan to deploy the proposed solution on a Raspberry Pi and test the model in a real scenario. In addition, the distance between the visible target and the masked target should be assessed using a regression model. The proposed solution could be extended to different types of targets (e.g. cars, robots, pedestrians...). This novel solution uses a supervised learning method, in other words, it already knows all the possible classes (One Target or Two Targets). If the situation of multiple shadowed targets needs to be addressed, it is theoretically possible by collecting enough data for every possible class. This method might not be practical because the number of classes could not be predicted beforehand. Therefore the recommended procedure would be to shift the problem into an unsupervised problem.

4.5 On Edge Human Action Recognition Using Radar-Based Sensing and Deep Learning

This section proposes a system for human action recognition based on deep learning (DL). The blocks of the system are designed for edge deployment. The data are collected using a low-cost FMCW radar connected to the edge device. The device transforms the signals into range-Doppler maps, treated as a series of images by the DNN. The performance of the system is evaluated both in terms of generalization accuracy and computational cost measured on the edge device. This evaluation covered the multi-class classification (i.e., 5 human action classes) and binary classification (i.e., fall vs non-fall classes).

The following are the novel contributions of this chapter:

- The system is low-cost and deployed on the edge.
- The proposed DNN classifies a series of range-Doppler maps through the medium of a time distributed layer (TDL).
- The DNN size achieves real-time edge inference.

The remainder of this section is organized as follows. In Section 4.5.1, the multi-class human action recognition method is described. In Section 4.5.2, the radar specifications, data collection, training procedure, and edge deployment procedure are detailed. In Section 4.5.3, experimental results including both model and edge system assessment are presented. Finally, Section 4.5.4 concludes this section.

4.5.1 Methodology

In this section, the author present the multi-class action recognition system. Figure 4.8 presents the block diagram of the action elaboration since signals are

acquired until the classification. The block diagram consists of four stages after that the radar receives the signals. In the following, all the stages are detailed.

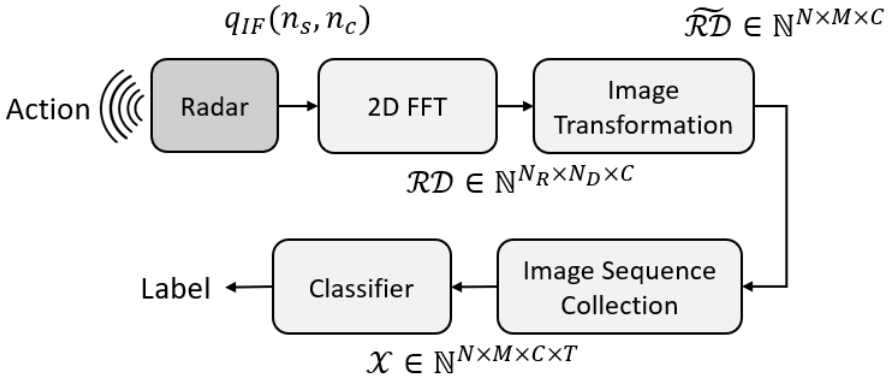

Figure 4.8: Block diagram of the action elaboration

During the online inference, all the stages are deployed on an edge device. Thus, a trade-off between generalization accuracy and the time for retrieving the action label gets crucial.

4.5.1.1 2D FFT

In the 2D FFT stage, the signals received by the Position2Go FMCW radar [185] are processed by edge device (i.e., the Raspberry Pi 4) to obtain range-Doppler matrices, also known as range-Doppler maps [28]. The radar receiver antenna receives a delayed and attenuated copy of the transmitted wave. An I/Q mixer demodulates the received wave and returns an intermediate frequency (IF) signal. The signal is sampled by an analog-to-digital converter (ADC) and organized in a 2D matrix. Following the notation adopted in [186], the matrix can be represented as:

$$\begin{aligned} q_{IF}(n_s, n_c) = A_{IF} e^{j2\pi(f_b T_s n_s - f_D n_c T_{PRI})} \text{ with} \\ n_s = 0, ..., N_s - 1;\ n_c = 0, ..., N_c - 1 \end{aligned} \tag{4.12}$$

where A_{IF} is proportional to the strength of the received echo, T_s is the sampling period, f_D is the Doppler frequency shift, f_b is the beat frequency, T_{PRI} is the pulse repetition interval, N_c is the number of chirps with N_s samples per chirp. According to equation 4.12 in [186], the signals in q_{IF} are filtered producing a filtered matrix $u(n_s, n_c)$. The range-Doppler (RD) map is computed as:

$$\begin{aligned} &RD^{(K_{sf})}(n_b, n_D) \\ &= \mathcal{F}_D^{N_D}\left\{\mathcal{F}_r^{N_R}\left\{u \times \omega_r^{(K_{sf})}\right\} \times \omega_D^{(K_{sf})}\right\}(n_b, n_D) \end{aligned} \tag{4.13}$$

where u is the filtered matrix after removing the clutters [28], $\omega_r^{K_{sf}}$ and $\omega_D^{K_{sf}}$ are Kaiser windows to be applied on the beat frequency and Doppler dimensions with a shape factor K_{sf}, and $\mathcal{F}_r^{N_R}$ and $\mathcal{F}_D^{N_D}$ are the range-FFT and Doppler-FFT outputting sequences of length N_R and N_D, respectively. After the processing, the RD map has dimension $N_R \times N_D$. In this work, $N_R = N_D = 256$.

Since a RD map is a 3D tensor, it can be considered as an image and can be formalized as $\mathcal{RD} \in \mathbb{N}^{N_R \times N_D \times C}$ as in Fig. 4.8, where N_R and N_D represent the height and width of the image, while C represents the number of channels (e.g., $C = 1$ in a gray-scale image and $C = 3$ in a RGB format).

4.5.1.2 Image Transformation Stage

A transformation can be applied to an image to convert it from one domain to another. Viewing an image in different domains enables the identification of features that may not be as easily detected in the initial domain. Among the image transformation techniques, edge detectors proved to increase accuracy in deep learning applications [187]. In this chapter, five transformations have been applied to the RD maps ($\mathcal{RD}$ in Fig. 4.8), three of which are based on edge detectors (i.e., Canny, Sobel, and Roberts). During the transformation, the

RD maps are also resized to cope with the dimension of the input tensor of the classifier. Figure 4.9 shows the different transformations applied on an exemplary RD map. The RD map format is a RGB image (Fig. 4.9(a)). As aforesaid, this image is a 3D tensor of dimension $N_R \times N_D \times C$. The applied transformations are the following:

- **Gray** (Fig. 4.9(b)) decreases the number of channels C to 1, reducing also the color dependency.
- **Canny** (Fig. 4.9(c)) uses a multi-stage algorithm to detect a wide range of edges in images.
- **Sobel** (Fig. 4.9(d)) convolves the image with a small, separable, and integer-valued filter in the horizontal and vertical directions.
- **Roberts** (Fig. 4.9(e)) approximates the gradient of an image through discrete differentiation which is achieved by computing the sum of the squares of the differences between diagonally adjacent pixels.
- **Binary** (Fig. 4.9(f)) image is obtained by first applying the k-means clustering algorithm to a RD map, obtaining a gray-scale image. The clusters of pixels are then passed through a median filter to remove the outliers and setting the non-outlier pixels to white.

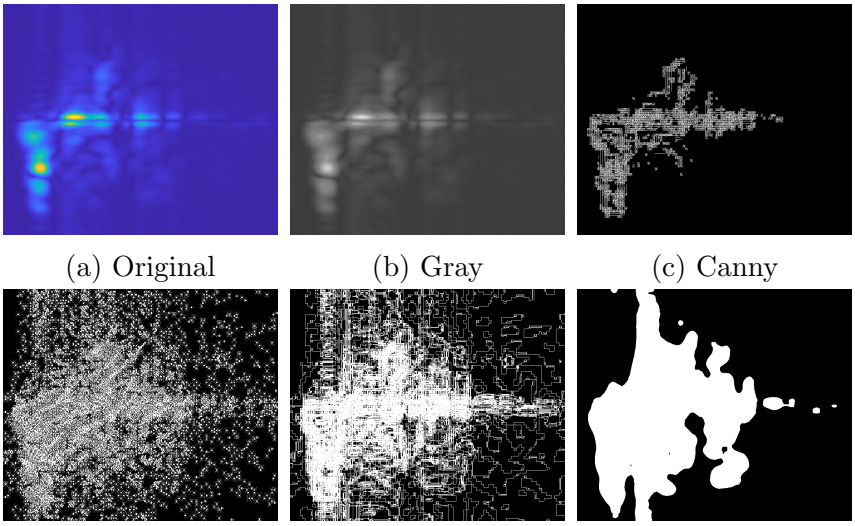

(a) Original (b) Gray (c) Canny

(d) Sobel (e) Roberts (f) Binary

Figure 4.9: Example of image transformations applied to the original image (a): (b) Gray scale, (c) Canny, (d) Roberts, (e) Sobel, and (f) Binary

A transformed and resized RD map can be formulated as $\widetilde{\mathcal{RD}} \in \mathbb{N}^{N \times M \times C}$ (Fig. 4.8).

4.5.1.3 Image Sequence Collection

RD maps vary in time. Therefore, the sequence of RD maps is time-dependent. To classify the action, T $\widetilde{RD}$ images of each action performed in the FoV are collected as a 4D tensor datum, as shown in Figure 4.10. The 4D tensor can be formalized as $\mathcal{X} \in \mathbb{N}^{N \times M \times C \times T}$.

The adoption of sequences of RD maps results in an advantage in terms of classification accuracy over the single-image one, as demonstrated for human actions recognition in [107]. By contrast, a image sequence classification approach would increase the computational cost of the classifier. Hence, the edge device's computational capacity needs to be taken into consideration during the development of the system. Thus, a trade-off between accuracy and computational cost of the elaboration system gets crucial.

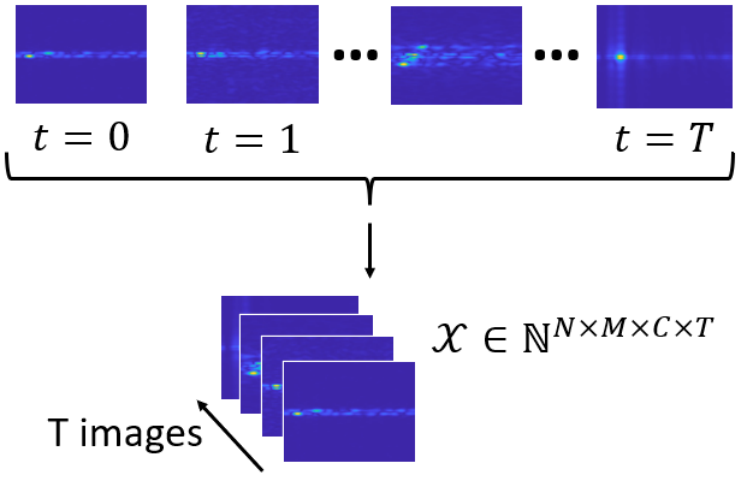

Figure 4.10: Example of a 4D tensor representing an action

4.5.1.4 Classifier

Figure 4.11 shows the proposed DNN (Classifier in Fig. 4.8) used to classify the sequence of images.

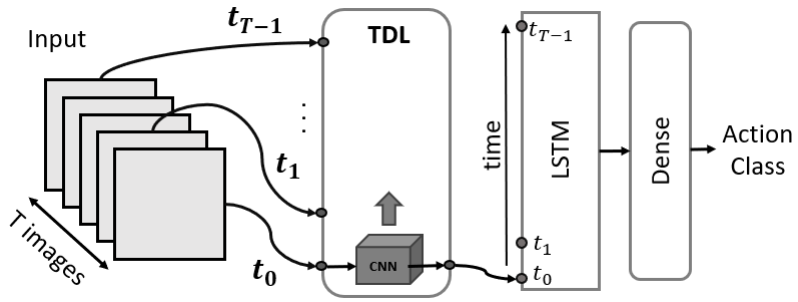

Figure 4.11: Proposed DNN

A Time Distributed Layer (TDL) applies the same layer(s) to every time step of the input. In this work, the TDL uses a CNN to extract T feature maps from the T images of the 4D input tensor. Thus, the output of the TDL is a sequence of feature maps. A LSTM layer learns the dependencies between the sequence of feature maps. Finally, two dense layers are the output layers of the DNN. The first one represents a fully connected network with a ReLU activation function.

The second is made of Neu neurons, where Neu is the number of classes involved in the training process with a Softmax activation function to assign the action label.

Three CNNs are designed to extract features from the 4D inputs. The use of CNNs aims to automatically extract features by learning the kernels (i.e. filters) that convolve with the data. This practice is adopted to topple the domain-specific feature extraction, which is usually crafted manually by subject-matter experts. The CNNs have been designed as a proof of concept for the feasibility of the action recognition system. Therefore, future works will address exhaustive benchmarks with state-of-the-art architectures.

Figure 4.12 shows the CNN basic architecture (called CNN2). The CNN2 comprises six main blocks: the first one, B1, consists of six 2D convolutional layers taking as input a 3D tensor of dimension $N \times M \times C$, where N and M represent the dimension of the frame and C is the number of channels. In this section, the range-Doppler maps (Fig. 4.9(a)) have number of channels $C = 3$, while all the transformed images (Fig. 4.9(b)-(f)) have $C = 1$. Each one of the five blocks (i.e., B2, B3, B4, B5, B6) consists of a Batch Normalization layer followed by a 2D Average Pooling and a dynamic number of 2D convolutional layers (the number of convolutional layers decreases by one along with the blocks). The last block, B6, contains only one convolutional layer. Following this block, a Batch Normalization and Global Average Pooling layers are added. In particular, the Global Pooling flattens the last feature map.

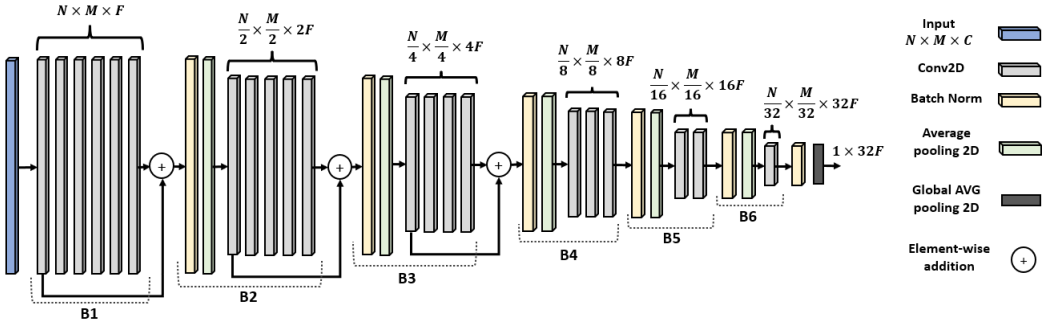

Figure 4.12: CNN2 architecture

Two different variations of the CNN2 architecture are also examined. CNN1 has an architecture similar to CNN2 but with a lower number of layers: it contains five blocks instead of six, each block has a convolutional layer less than CNN2, and the Global Pooling is applied to the output of the fifth block (the last one in this case). On the opposite, CNN3 has one more convolutional layer in each block with respect to CNN2, thus presenting seven main blocks. The results of the performances in terms of generalization accuracy and computational cost are presented in Section 4.5.3.

4.5.2 Experimental Setup

4.5.2.1 FMCW Radar Specifications

The radar used in the experiments is the Position2Go FMCW radar model operating on the 24 GHz ISM band, by Infineon Technologies [185]. The radar is equipped with a pair of arrays of micro-strip patch antennas (one for transmitting and two for receiving) characterized by a 12 dbi gain and 19×76 degree beam widths, defining the Field of View (FoV) in both elevation and azimuth axes respectively. The sampling rate used for the data collection is 213 kHz to detect the high-frequency components of the signal that appear when different actions occur (around 60 Hz) [107]. This development kit allows the user to implement

and test several sensing applications at the 24 GHz ISM bands, such as localizing, tracking, and collision avoidance [185]. Table 4.6 lists the radar parameters that are set for the data collection procedure.

Table 4.6: Position2Go radar specifications.

Parameters	Value
Sweep Bandwidth	200 MHz
Center Frequency	24 GHz
Up-Chirp Time	300 μs
Number of Samples/Chirp (Ns)	64
Number of Chirps/Frame (Nc)	64
Maximum Range	48 m
Maximum Velocity	10.5 km/h
Range Resolution	0.75 m
Velocity Resolution	0.4 km/h
Sampling Rate	213.33 KHz

4.5.2.2 DNNs Parameters

According to Fig. 4.12, the CNN input has dimensions $N \times M \times C$. We chose $N = M = 224$ and $C = 3$ in case of an RGB image (i.e., Fig. 4.9(a)) and $C = 1$ for all the other transformations (i.e., Fig. 4.9(b)-(f)). As mentioned in Sec. 4.5.1.2, since the original RD maps (i.e., $\mathcal{RD}$ in Fig. 4.8) have dimension $256 \times 256 \times 3$, all the images have been resized to $224 \times 224 \times 3$ before applying the transformations. In B1 block of all the models, the number of filters F is set equal to 8 while, in the further blocks, F is doubled while N and M are reduced by 50%. As a result, in the last block of CNN2 in Fig. 4.12 (i.e. $B6$ for CNN2) the output has dimension $7 \times 7 \times 256$. Consequently, the output of CNN1 has dimensions $14 \times 14 \times 128$, while the output of the CNN3 has dimensions $3 \times 3 \times 512$. The LSTM layer that follows the TDL layer in Fig. 4.11 has 128 neurons for all the models. The first dense layer has 64 neurons in all the models. The output layer has five neurons, corresponding to the five classes. Table 4.7 presents the

total number of parameters for each model. Model1 refers to the architecture of Fig. 4.11 using CNN1. Equally, Model2 and Model3 use CNN2 and CNN3, respectively.

Table 4.7: Number of parameters of the three models

Model	Number of parameters
Model1	304,117
Model2	862,509
Model3	2,962,533

4.5.2.3 Data Collection

The data have been collected in two different environments at the University of Genova, Italy. The environments contain clutters such as desks, PCs, and metal lockers, as shown in Fig. 4.13.

(a) Environment 1 (b) Environment 2

Figure 4.13: Environments for data collection

A data sample consists of 15 consecutive range-Doppler maps acquired during 3 seconds of an action performed in the FoV of the radar. The data samples are presented in RGB format as shown in Fig. 4.9(a). The dataset contains 5 classes:

- **Fall**: the subject falls from a walking or standing state on a mattress.
- **Bed-Fall (Bed)**: a couch (Fig. 4.13(b)) is used to represent a bed. It is moved around the environment to perform the 'fall from bed' action from different angles with respect to the radar's FoV.

- **Sit**: the subject sits down on the couch or chairs positioned in different locations of the environment.
- **Stand**: the subject stands up from the couch or chairs positioned in different locations of the environment.
- **Walk**: the subject walks in the FoV of the radar.

The goal of collecting data samples for the last three classes is to prove the ability to distinguish among actions. The actions have been performed by five healthy subjects aged between 25 and 30. Only one subject performed one action at time. To eliminate possible data-collection selection bias, the subject executed the same action in different ways (e.g., change the starting and/or ending positions with respect to the radar, perform the action faster/slower, etc.). In total, one hundred data samples, i.e. twenty per subject, have been collected for each class (50 for each environment). The dataset is formalized as:

$$\begin{aligned}\mathcal{D}_{Orig} = \Big\{ (\mathcal{X}, y)_i \,; \mathcal{X}_i \in \mathbb{N}^{224\times224\times3\times15}; y_i \in \{Fall, \\ Bed,\ Sit,\ Stand,\ Walk\}\,;\ i = 1, ..., 500 \Big\}\end{aligned} \tag{4.14}$$

Table 4.8 summarizes the collected data. The first column shows the performed actions, the second column depicts the class corresponding to each action, and the last column reports the number of data acquired in each environment per class.

Table 4.8: Collected Dataset Summary

Actions	Classes Names	Num of samples
Falling from a walking/ standing position	Fall	100
Falling from a laying on a couch position	Bed-Fall	100
Sitting down on a chair/couch	Sit	100
Standing up from a chair/couch	Stand	100
Walking	Walk	100

Five datasets have been generated from the $\mathcal{D}_{Orig}$ dataset by applying the transformation techniques described in Sec. 4.5.1.1. These datasets can be formalized as:

$$\mathcal{D}_d = \Big\{ (\mathcal{X}, y)_i \,;\, \mathcal{X}_i \in \mathbb{N}^{224\times224\times1\times15}; y_i \in \{Fall, \\ Bed,\ Sit,\ Stand,\ Walk\}\,;\ i = 1, ..., 500 \Big\} \tag{4.15}$$

with $d \in \{Gray,\ Canny,\ Sobel,\ Roberts,\ Binary\}$.

Each of the three models is trained using the six datasets (4.14) and (4.15). The generalization accuracies are evaluated and compared in Sec. 4.5.3.1.

4.5.2.4 Training Procedure

The training procedure has been hosted off-line by a desktop PC with a Nvidia GeForce RTX 2080Ti GPU. All the models are trained with the following parameters:

- Adam optimizer with a learning rate $lr_{start} = 7e^{-5}$;
- Number of epochs $ep = 200$;

- Batch size $bs = 10$;
- Loss function $lf = categorical\ cross\ entropy$;
- Early stop on validation accuracy with patience $p = 10$.

The stratified K-fold technique is adopted to provide fair results. According to the technique, a labeled dataset (*population*) is split into K parts containing the same proportion of data per class as in the population. This mechanism guarantees that the training and test sets contain the same proportion of data in each fold without affecting the approximation of the generalization accuracy. Each k-th part is used, in turn, as the test set. The remaining $K-1$ folds compose the training set. In our experiments, K is set to 5. In this way, each fold contains 100 data samples, 20 per class. The generalization accuracy results presented in the next section are averaged over the five folds.

Early stop criterion is adopted: from the $K-1$ folds used during the training, a validation set using a ratio of $1/4$ over the number of training data is extracted randomly. Eventually, a learning rate decay is adopted: during the training process, the learning rate is reduced every 10 epochs, multiplying it by 0.9. When the early stop criterion is satisfied (i.e. the validation accuracy decreases continuously for p epochs), the training procedure ends.

4.5.2.5 Edge Deployment Procedure

After the training procedure, the trained models need to be deployed on the edge device. Depending on the application requirements, a trade-off between model size, latency, and accuracy needs to be evaluated. Therefore, model optimization options must be considered during the conversion of the model for the edge deployment.

TensorFlow Lite (TF-Lite) is used to deploy deep learning models on mobile and edge devices (e.g., dev boards, micro-controller), offering optimization options for converting a TF model into the TF-Lite format. The adopted optimization option is quantization. It represents the model with lower precision (e.g., floating-point 16 (FP16) instead of the default floating-point 32 (FP32) representation), reducing the memory occupied by the model and the inference time. In this work, two quantization options have been used: no quantization, i.e. the model parameters are represented as FP32; FP16, the parameters are converted in FP16 cutting across the model size without affecting the inference time. The third possible option, i.e. integer 8 (INT8) quantization, is not adopted because the CPU of the edge device does not support the INT8 operations.

The device considered for this study is the Raspberry Pi4, including a high-performance 64-bit quad-core processor, and 4GB of RAM. The 4 GB version of the Raspberry Pi has indeed proved to be a reliable edge computing device for the elaboration of signals collected by an FMCW radar [186; 188].

4.5.3 Results and Discussion

When introducing Edge AI systems, it is crucial to assess two complementary aspects of it. The first side is the model effectiveness considering the goal of the activity, i.e. the classification accuracy of actions. The second side is the efficiency of the proposed Edge AI system (e.g., inference time, power consumption, energy precision ratio, etc).

4.5.3.1 Classification Accuracy

In this section, the results in terms of accuracy are presented. At first, the accuracy of the multi-class classification problem is assessed. Secondly, some performance metrics are evaluated in a binary classification problem. In this

case, the classes Fall and Bed-Fall are considered fall actions (i.e., harmful), and the other classes are considered non-fall actions. The performance is computed on the multi-class classification results, by grouping the predicted labels into harmful and non-harmful classes.

Multi-class classification

Table 4.9 shows the average accuracy on the test set computed over the K folds for each of the three DNNs. The first column indicates the datasets, the other three columns report the average accuracy with their standard deviation. The accuracies, computed on the test sets, are averaged over the five folds. The best accuracy for each DNN is emboldened. Concerning DNN1, which contains the lowest number of parameters accordingly to Table 4.7, $\mathcal{D}_{Canny}$ presents the highest accuracy. For both DNN2 and DNN3, the best accuracies are achieved on the $\mathcal{D}_{Gray}$ dataset. The overall best accuracy (i.e. 93.2%), is obtained by DNN3 which contains the largest number of parameters (Table 4.7), therefore the highest memory occupation and power consumption on an edge device.

Figure 4.14 shows the confusion matrices for the best DNNs, emboldened in Table 4.9, i.e, DNN1 trained with $\mathcal{D}_{Canny}$, DNN2 and DNN3 trained with $\mathcal{D}_{Gray}$. The predicted labels of the 5 folds have been merged, resulting in a hundred test samples for each class. The most reliable DNN for detecting falls, which coincides with the classes named Fall and Bed-Fall as described in Section 4.5.2.3, is DNN3. DNN2 shows a lower accuracy in detecting the Fall class. As one can notice from the first row in DNN3, the miss-classified samples are mostly classified as Sit. This is possibly due to the similarity between Fall and Sit actions.

Table 4.9: Average accuracy on the 5-Folds

Dataset	Average Accuracy ± Standard Deviation		
	DNN1	DNN2	DNN3
$\mathcal{D}_{Orig}$	.730 ± .044	.920 ± .026	.930 ± .028
$\mathcal{D}_{Gray}$	.768 ± .065	**.926 ± .022**	**.932 ± .029**
$\mathcal{D}_{Canny}$	**.828 ± .044**	.892 ± .037	.864 ± .022
$\mathcal{D}_{Sobel}$	.740 ± .054	.916 ± .038	.884 ± .026
$\mathcal{D}_{Roberts}$	.764 ± .071	.880 ± .021	.886 ± .037
$\mathcal{D}_{Binary}$	.700 ± .072	.860 ± .042	.858 ± .017

(a) Model1 trained on $\mathcal{D}_{Canny}$

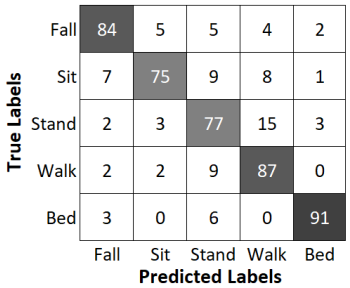

(b) Model2 trained on $\mathcal{D}_{Gray}$

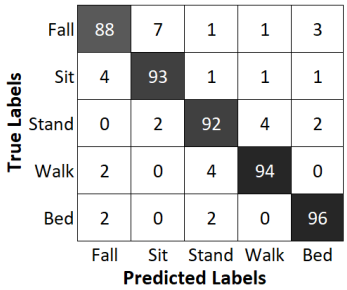

(c) Model3 trained on $\mathcal{D}_{Gray}$

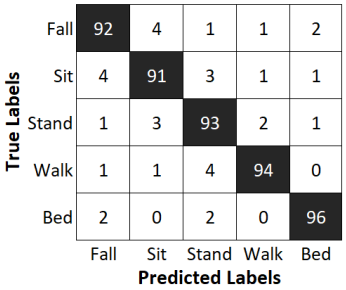

Figure 4.14: Confusion matrices of the three best models computed over the five folds

Binary Classification

Indoor safety can be addressed as a binary problem. It consists of generating a notification whenever a harmful action happens. Thus, the classes Fall and Bed-Fall are considered as Fall actions (i.e., harmful), and the other classes are considered as Non-Fall actions. The previously trained models are assessed in a binary approach, without retraining, by grouping the labels into two classes (i.e., Harmful and Non-Harmful).

The following notation is used: True Positives (TP) are fall actions correctly classified, False Positives (FP) are non-fall actions incorrectly classified as Fall, True Negatives (TN) are non-fall actions correctly classified, False Negatives (FN)

are fall actions incorrectly classified as Non-Fall.

The following metrics are then adopted:

- Precision (PR), $\text{PR} = \frac{\text{TP}}{\text{TP+FP}}$
- Recall or sensitivity (SE), $\text{SE} = \frac{\text{TP}}{\text{TP+FN}}$
- Specificity (SP), $\text{SP} = \frac{\text{TN}}{\text{TN+FP}}$
- False Positive Rate (FPR), $\text{FPR} = \frac{\text{FP}}{\text{FP+TN}}$
- False Negative Rate (FNR), $\text{FNR} = \frac{\text{FN}}{\text{FN+TP}}$
- F-score, $\text{F} = 2 \times \frac{\text{PRxSE}}{\text{PR+SE}}$

Table 4.10 presents the classification metrics obtained following the binary classification approach, assessed on the three best performing models of Table 4.9. The results presented in Table 4.10 prove that the proposed system is capable of distinguishing harmful from non-harmful actions. In particular, the FNR, which represents the percentage of harmful actions that do not activate the alarm since they are classified as non-harmful, is low, especially in DNN3. In general, DNN3 presents the best performance for all the metrics with respect to DNN1 and DNN2.

Table 4.10: Metrics computed for the best performing models

Models	**Acc**	**PR**	**SE**	**SP**	**FPR**	**FNR**	**F**
Model1 $\mathcal{D}_{Canny}$	.930	.927	.900	.950	.055	.100	.911
Model2 $\mathcal{D}_{Gray}$	.960	.956	.945	.970	.050	.100	.950
Model3 $\mathcal{D}_{Gray}$	.968	.962	.960	.973	.030	.055	.960

To further investigate the performance of the three best performing models (in terms of accuracy) the Receiver Operating Curves (ROC) and the Area Under Curves (AUC) are computed on each fold is plotted. The ROC curve plots the

True Positive Rate (TPR) against the False Positive Rate (FPR), varying the threshold for the score (i.e., the probability) computed on the output neurons. The AUC represents the area under the ROC curve. It is equivalent to the probability that a randomly chosen positive instance is ranked higher than a randomly chosen negative instance. The AUC can be considered as an indicator of the performance of a classifier: the higher the value the higher the prediction accuracy. Figure 4.15 reports the ROC and the AUC for the three best models. In each plot, we present seven lines: five colored lines refer to the ROC in each fold, the blue dotted line represents the average ROC curve, and the black dashed line corresponds to the baseline classifier where FPR is equal to TPR. In the legend, we report the AUC corresponding to each fold and the average.

(a) Model1 trained on $\mathcal{D}_{Canny}$ (b) Model2 trained on $\mathcal{D}_{Gray}$ (c) Model3 trained on $\mathcal{D}_{Gray}$

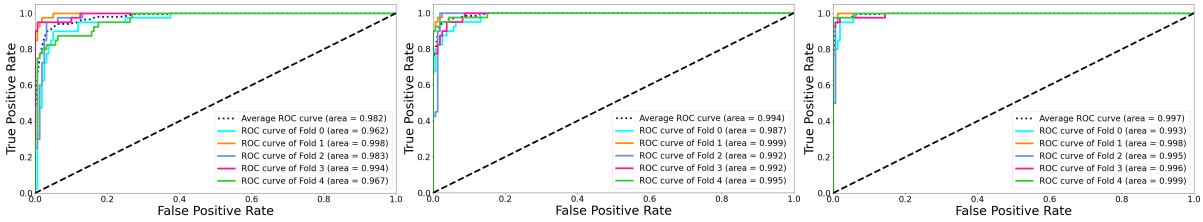

Figure 4.15: ROC and AUC computed over the folds of the best performing models

DNN3 presents the highest average AUC value. In general, DNN3 trained on $\mathcal{D}_{Gray}$ is a reliable model for detecting fall actions, achieving the highest accuracy in the multi-class classification problem, the lowest false negative rate in the binary classification problem, and the highest AUC value. Also, DNN2 could be a valuable option: despite it presenting slightly lower generalization performance with respect to DNN3, it contains less the one-third of the parameters than DNN3 (Table 4.7). Thus, it is expected that, when deploying the models on the edge device, the computational cost of DNN2 is lower than the DNN3 one. In fact, during the deployment not only the generalization performance is important, but

also the computational cost. In this chapter, the computational cost is measured keeping into consideration all the stages of data elaboration (Fig. 4.8).

4.5.3.2 Edge System Assessment

The computational cost is evaluated as the inference time, power consumption, size of the model, and energy-precision ratio. Power consumption is estimated using a USB multi-meter that is attached to the power supply of the edge device while running the inference. The Energy-Precision Ratio (EPR) can be computed as $EPR = Error \times EPI$, where $Error$ represents the classification error and EPI is the energy consumption per classified data item (Energy Per Item). According to Sec. 4.5.2.5, two TF-Lite optimization methods are applied during the conversion of the three best DNNs in TF-Lite models. These classifiers and the previous stages are deployed on the Raspberry Pi4.

Table 4.11 shows the computational cost and the classification accuracy of the quantized DNNs. All the results are averaged on the 500 test data used also to evaluate the classification performance in the previous section. The first column depicts the models, the second column reports the quantization applied to each model for the deployment, and from the third, to the last column, the table shows the five metrics averaged on 100 test samples over the 5 folds.

Table 4.11: Edge AI system assessment on Raspberry Pi4

Models	**Quant**	**Avg Acc**	**Time T (s)**	**Power (W)**	**Size (MB)**	**EPR (PoS)**
Model1	FP16	0.830	1.964	5.67	0.64	1.86
$\mathcal{D}_{Canny}$	FP32	0.828	1.967	5.80	1.2	1.96
Model2	FP16	0.928	2.415	6.03	1.8	1.04
$\mathcal{D}_{Gray}$	FP32	0.926	2.415	6.13	3.5	1.09
Model3	FP16	0.932	2.945	6.20	6.0	1.24
$\mathcal{D}_{Gray}$	FP32	0.932	2.948	6.16	11.9	1.23

As expected, the first model (i.e., DNN1) has the lowest inference time and

energy consumption, because of the lowest number of parameters that affect the model size. Straightforwardly, DNN3 presents the highest inference time and energy consumption. As can be noticed, the quantization to FP16 in DNN1 and DNN2 slightly improves the classification accuracy because it can act as a filter removing bits related to noise.

The best trade-off between generalization accuracy and inference time is achieved by DNN2, following EPR column of the table. The inference time of all the stages, with DNN2 as a classifier, is 2.4 seconds, thus guaranteeing to generate an alarm in less than 6 seconds also considering 3 seconds for data acquisition.

4.5.3.3 Discussion

In this section, the proposed system is compared with the SoA systems that concern human action (including fall) classification using radar-based sensing and machine learning [123; 124; 125; 126; 127; 128; 129; 130; 131]. Table 4.12 presents a comparison between the proposed system and the one proposed in [126] where the inference time is reported while running on a PC equipped with a GPU. The classification accuracies of the SoA systems are comparable with the proposed approach. None of the inference time nor the power consumption of the other SoA systems has been measured using an edge device: a model that achieves high accuracy, while requiring high computational power, might not be deployed on the edge. Moreover, the proposed system requires less time for acquiring the data with respect to the other ones, except in [127; 128]. In these two works, the data are acquired and classified continuously. In a real deployment scenario, the continuous elaboration of data is not efficient from the computational cost point of view, especially for edge deployment where the device is generally battery supplied.

Concluding, the proposed multi-class classification system presented encour-

Table 4.12: Comparing the proposed system with SoA

Ref	Number of Classes	Accuracy	Acquisition Time (s)	Inference Time (s)
[126]	2	0.958	15	2.36 (PC)
This work	5 2	0.932 0.968	3	2.95 (Edge)

aging results, it proved a high accuracy in classifying 5 human actions using a low-cost edge device with low inference time. The system also proved to be effective in generating an alarm whenever a harmful action occurs.

4.5.4 Conclusion

In this article, the deployment on the edge of a radar-based action recognition system using deep learning has been proposed. This system used sequences of range-Doppler maps extracted from a low-cost FMCW radar. A time distributed layer has been used to process the sequence of range-Doppler maps. The results showed that the model with the highest number of parameters (i.e., DNN3) achieved the best accuracy (93.2%) in the 5-class classification problem using grayscale data transformation. Moreover, the same model distinguished harmful from non-harmful actions with an accuracy of 96.8% and a false-negative rate of 4%. Using a radar that has higher performance would certainly help reduce the classification error and the false negative rate. The proposed system has been deployed on a Raspberry Pi4 to assess the performance in terms of accuracy and computational cost. The results showed that the system that uses DNN2 achieved the best trade-off, with a small drop in accuracy, i.e., lower than 1%, with respect to DNN3 and an inference time lower than 2.5s.

Future works will address the multi-target classification problem, the assessment of the performances while training the model in one environment and testing

it in different environments, and the deployment of the system on other edge devices that endorse accelerators for deep learning (e.g., Coral Dev Board).

4.6 Summary and Conclusion

Target classification systems occasionally put the welfare of the general public first. Such technologies, for instance, are employed in autonomous vehicles to guarantee the security of pedestrians. In this application, the two main rivals are radars and vision sensors. Radar sensors, on the other hand, have shown to be more durable in inclement weather and poor lighting. FMCW radars are the most frequently employed among the several types of radar technologies for these kinds of applications. In fact, this is due to their capacity to deliver range and Doppler data simultaneously. In comparison to pulse and UWB radar sensors, they also need a lower sampling rate and a lower peak to average ratio.

In this chapter, two systems were proposed.

- Method for discriminating shadowed targets
- Edge cost-efficient multi-action classification system

The system utilizes a cutting-edge surveillance method based on affordable FMCW radar technology. The data processing method is based on an ad-hoc chain made up of various blocks that remove clutter and leakage using a frame subtraction technique, apply DL algorithms to Range-Doppler maps, introduce a peak to cluster assignment step before tracking targets, transform data, extract features, and finally make a classification decision.

To conclude, the use of an FMCW radar along with a DL approach for the RD maps proved to be effective for indoor use-cases. The aforementioned tests used the Position2Go FMCW radar toolkit by Infineon Technologies along with an edge device (i.e., Raspberry Pi 4).

Chapter 5

Conclusions and Future Works

5.1 Conclusions

Real-time geodata is used by location-based services (LBS) to offer information, entertainment, or security. LBS is the primary enabling technology in the wireless communication sector and is growing exponentially. LBS encompasses a wide range of techniques, tools, and strategies. The basic objective of all these techniques is to precisely pinpoint a specific target in real time. This target could be a robot, a person, or anything else that moves.

Two potential methods for subject monitoring are examined in-depth in the presentation. This kind of activity is very important for military applications, medical tracking, industrial workers, and for offering location-based services to the community of mobile users, which is constantly expanding.

Estimation problems, and particularly parameter estimation, have drawn a lot of interest because of their applicability and the consumer's ongoing demand for higher performance. As applications expanded, a lot of interest was generated in the accurate assessment of temporal and spatial properties. In-depth analyses of the two most promising subject monitoring strategies were reported in this article. Considering the performance, intrusiveness, and low cost constraints. The suggested systems underwent extensive testing in various settings.

The practicality of implementing the AoA and RSSI localization algorithms in practical settings is evaluated in depth. We discussed and provided details for two potential systems. These systems underwent testing in various settings (e.g., indoor, outdoor, in water...). The localization capacity was demonstrated by the results, but this method is only effective up to a distance of about 150 meters due to the low-cost antenna we used. Therefore, this strategy may or may not be advantageous depending on the use-case.

In this investigation, a different strategy was taken into account. Radar sensors have proven to be resilient in bad weather and dim light. Among the several types of radar technologies, FMCW radars are the most frequently used for these kinds of applications. In actuality, this is because of their ability to concurrently give range and Doppler data. They also require a lower sample rate and a lower peak to average ratio than pulse and UWB radar sensors. The system makes use of an advanced surveillance technique based on easily accessible FMCW radar technology. The data processing method is based on an ad-hoc chain of various blocks that transform data, extract features, and make a classification decision before clearing clutter and leakage using a frame subtraction technique, applying DL algorithms to Range-Doppler maps, introducing a peak to cluster assignment step before tracking targets. Conclusion: For interior use-cases, the combination of an FMCW radar with a DL method for the RD maps worked well. The aforementioned tests made use of an edge device and the Position2Go FMCW radar toolkit from Infineon Technologies (i.e., Raspberry Pi 4).

5.2 Future Works

There is always room for improvement because subject monitoring is such a broad topic and because market expectations are constantly rising. The following is a list of some of the subjects that might be worth more investigation.

- The suggested angle of arrival estimation technique can be improved to incorporate 3D angle of arrival estimation and used to assess the effectiveness of angle of arrival estimation with more antenna designs.

- Future improvements to the FMCW radar technique can be researched with the intention of including more sophisticated processing blocks, such as tracking schemes based on probabilistic models of relationships.

- Additionally, efforts will be made to integrate improved radar boards, tackling the multi-target classification problem. The improved radar boards can provide target positions through the directions of arrival of reflected signals or operate at higher frequencies, in order to improve classification capabilities, particularly when there are numerous targets nearby.

- A key consideration whenever Deep Learning solutions are employed is the evaluation of the performances of trained systems when the model is being trained in one environment and tested in another.

- Last but not least, the system's implementation on various edge devices that support deep learning accelerators is also an interesting point to look into. This strategy should incorporate edge devices that are less expensive (e.g., Raspberry Pi Pico), more sophisticated (e.g., Coral Dev Board), and comparable to those employed in this work.

References

[1] J. E. Bardram and H. B. Christensen, "Pervasive computing support for hospitals: An overview of the activity-based computing project," *IEEE Pervasive Computing*, vol. 6, no. 1, pp. 44–51, 2007. 1

[2] J. E. Bardram, "Applications of context-aware computing in hospital work: examples and design principles," in *Proceedings of the 2004 ACM symposium on Applied computing*, pp. 1574–1579, 2004. 1

[3] R. Zekavat and R. M. Buehrer, *Handbook of position location: Theory, practice and advances*, vol. 27. John Wiley & Sons, 2011. 1

[4] P. Steggles and S. Gschwind, "The ubisense smart space platform," 2005. 1

[5] B. Simon, Z. Miklós, W. Nejdl, M. Sintek, and J. Salvachua, "Smart space for learning: A mediation infrastructure for learning services," in *Proceedings of the twelfth international conference on world wide web*, pp. 20–24, 2003. 1

[6] S. Helal, W. Mann, H. El-Zabadani, J. King, Y. Kaddoura, and E. Jansen, "The gator tech smart house: A programmable pervasive space," *Computer*, vol. 38, no. 3, pp. 50–60, 2005. 1

[7] P. M. Singh and M. van Sinderen, "Interoperability challenges for context

aware logistics services-the case of synchromodal logistics.," in *IWEI Workshops*, 2015. 1

[8] I. Durazo-Cardenas, A. Starr, A. Tsourdos, M. Bevilacqua, and J. Morineau, "Precise vehicle location as a fundamental parameter for intelligent self-aware rail-track maintenance systems," *Procedia CIRP*, vol. 22, pp. 219–224, 2014. 1

[9] L. Evers, M. J. Bijl, M. Marin-Perianu, R. Marin-Perianu, and P. J. Havinga, "Wireless sensor networks and beyond: A case study on transport and logistics," in *International Workshop on Wireless Ad-Hoc Networks (IWWAN 2005), London, Uk*, 2005. 1

[10] K. Kuladinithi, O. Bergmann, T. Pötsch, M. Becker, and C. Görg, "Implementation of coap and its application in transport logistics," *Proc. IP+ SN, Chicago, IL, USA*, 2011. 1

[11] P. L. Smith, "Effects of imperfect storm reporting on the verification of weather warnings," *Bulletin of the American Meteorological Society*, vol. 80, no. 6, pp. 1099–1106, 1999. 1

[12] V. Lenders, E. Koukoumidis, P. Zhang, and M. Martonosi, "Location-based trust for mobile user-generated content: applications, challenges and implementations," in *Proceedings of the 9th workshop on Mobile computing systems and applications*, pp. 60–64, 2008. 1

[13] C. Xu, S. Jia, L. Zhong, and G.-M. Muntean, "Socially aware mobile peer-to-peer communications for community multimedia streaming services," *IEEE Communications Magazine*, vol. 53, no. 10, pp. 150–156, 2015. 1

[14] G. Gennarelli, I. Catapano, X. Dérobert, and F. Soldovieri, "A ground penetrating radar imaging approach for a heterogeneous subsoil with a ver-

tical permittivity gradient," *IEEE Transactions on Geoscience and Remote Sensing*, vol. 59, no. 7, pp. 5698–5710, 2020. 2, 8

[15] A. Benedetto and L. Pajewski, *Civil engineering applications of ground penetrating radar*. Springer, 2015. 2, 8

[16] S. Lambot and F. André, "Full-wave modeling of near-field radar data for planar layered media reconstruction," *IEEE Transactions on Geoscience and Remote Sensing*, vol. 52, no. 5, pp. 2295–2303, 2013. 2, 8

[17] M. Pastorino, A. Randazzo, A. Fedeli, A. Salvadè, S. Poretti, M. Maffongelli, R. Monleone, and M. Lanini, "A microwave tomographic system for wood characterization in the forest products industry," *Wood Material Science & Engineering*, vol. 10, no. 1, pp. 75–85, 2015. 2, 8

[18] T. Negishi, G. Gennarelli, F. Soldovieri, Y. Liu, and D. Erricolo, "Radio frequency tomography for nondestructive testing of pillars," *IEEE Transactions on Geoscience and Remote Sensing*, vol. 58, no. 6, pp. 3916–3926, 2020. 2, 8

[19] J. M. Munoz-Ferreras, F. Perez-Martinez, J. Calvo-Gallego, A. Asensio-Lopez, B.-P. Dorta-Naranjo, and A. Blanco-del Campo, "Traffic surveillance system based on a high-resolution radar," *IEEE transactions on geoscience and remote sensing*, vol. 46, no. 6, pp. 1624–1633, 2008. 2, 9

[20] R. Zhang and S. Cao, "Extending reliability of mmwave radar tracking and detection via fusion with camera," *IEEE Access*, vol. 7, pp. 137065–137079, 2019. 2, 9

[21] G. L. Charvat, *Small and short-range radar systems*. CRC Press, 2014. 3, 4, 13

[22] S. Saponara and B. Neri, "Radar sensor signal acquisition and multidimensional fft processing for surveillance applications in transport systems," *IEEE Transactions on Instrumentation and Measurement*, vol. 66, no. 4, pp. 604–615, 2017. 3, 4, 13

[23] A. Mukhtar, L. Xia, and T. B. Tang, "Vehicle detection techniques for collision avoidance systems: A review," *IEEE transactions on intelligent transportation systems*, vol. 16, no. 5, pp. 2318–2338, 2015. 3, 13, 14

[24] M. S. Bartlett, *An introduction to stochastic processes: with special reference to methods and applications*. CUP Archive, 1978. 3

[25] M. Chryssomallis, "Smart antennas," *IEEE Antennas and Propagation magazine*, vol. 42, no. 3, pp. 129–136, 2000. 3

[26] C. Li, Z. Peng, T.-Y. Huang, T. Fan, F.-K. Wang, T.-S. Horng, J.-M. Munoz-Ferreras, R. Gomez-Garcia, L. Ran, and J. Lin, "A review on recent progress of portable short-range noncontact microwave radar systems," *IEEE Transactions on Microwave Theory and Techniques*, vol. 65, no. 5, pp. 1692–1706, 2017. 4, 13

[27] P.-J. Wang, C.-M. Li, C.-Y. Wu, and H.-J. Li, "A channel awareness vehicle detector," *IEEE Transactions on intelligent transportation systems*, vol. 11, no. 2, pp. 339–347, 2010. 4, 13

[28] M. A. Richards, *Fundamentals of radar signal processing*. McGraw-Hill, second edition ed., 2014. 4, 75, 79, 94, 95

[29] M. Kronauge and H. Rohling, "New chirp sequence radar waveform," *IEEE Transactions on Aerospace and Electronic Systems*, vol. 50, no. 4, pp. 2870–2877, 2014. 4, 13

[30] J. Lin Jr, Y.-P. Li, W.-C. Hsu, and T.-S. Lee, "Design of an fmcw radar baseband signal processing system for automotive application," *SpringerPlus*, vol. 5, no. 1, pp. 1–16, 2016. 4, 15, 74

[31] T. Mitomo, N. Ono, H. Hoshino, Y. Yoshihara, O. Watanabe, and I. Seto, "A 77 ghz 90 nm cmos transceiver for fmcw radar applications," *IEEE journal of solid-state circuits*, vol. 45, no. 4, pp. 928–937, 2010. 4, 13, 15, 74

[32] P. Withington, H. Fluhler, and S. Nag, "Enhancing homeland security with advanced uwb sensors," *IEEE Microwave magazine*, vol. 4, no. 3, pp. 51–58, 2003. 8

[33] F. Colone, D. Pastina, P. Falcone, and P. Lombardo, "Wifi-based passive isar for high-resolution cross-range profiling of moving targets," *IEEE Transactions on Geoscience and Remote Sensing*, vol. 52, no. 6, pp. 3486–3501, 2013. 8

[34] G. Gennarelli, G. Vivone, P. Braca, F. Soldovieri, and M. G. Amin, "Multiple extended target tracking for through-wall radars," *IEEE Transactions on Geoscience and Remote Sensing*, vol. 53, no. 12, pp. 6482–6494, 2015. 8

[35] A. Randazzo, C. Ponti, A. Fedeli, C. Estatico, P. D'Atanasio, M. Pastorino, and G. Schettini, "A two-step inverse-scattering technique in variable-exponent lebesgue spaces for through-the-wall microwave imaging: Experimental results," *IEEE Transactions on Geoscience and Remote Sensing*, vol. 59, no. 9, pp. 7189–7200, 2021. 8

[36] B. Pottier, L. Rasolofondraibe, and S. Kerroumi, "Pedestrian detection strategy in urban area: Capacitance probes and pedestrians' signature," *IEEE Sensors Journal*, vol. 17, no. 17, pp. 5663–5668, 2017. 8

[37] X. Zhao, P. Sun, Z. Xu, H. Min, and H. Yu, "Fusion of 3d lidar and camera data for object detection in autonomous vehicle applications," *IEEE Sensors Journal*, vol. 20, no. 9, pp. 4901–4913, 2020. 8

[38] T. Gandhi and M. M. Trivedi, "Pedestrian protection systems: Issues, survey, and challenges," *IEEE Transactions on intelligent Transportation systems*, vol. 8, no. 3, pp. 413–430, 2007. 8

[39] A. Rasouli and J. K. Tsotsos, "Autonomous vehicles that interact with pedestrians: A survey of theory and practice," *IEEE transactions on intelligent transportation systems*, vol. 21, no. 3, pp. 900–918, 2019. 8

[40] S. Saponara, M. S. Greco, and F. Gini, "Radar-on-chip/in-package in autonomous driving vehicles and intelligent transport systems: Opportunities and challenges," *IEEE Signal Processing Magazine*, vol. 36, no. 5, pp. 71–84, 2019. 9

[41] S. Fontul, A. Paixão, M. Solla, and L. Pajewski, "Railway track condition assessment at network level by frequency domain analysis of gpr data," *Remote Sensing*, vol. 10, no. 4, p. 559, 2018. 9

[42] P. Kułakowski, J. Vales-Alonso, E. Egea-López, W. Ludwin, and J. García-Haro, "Angle-of-arrival localization based on antenna arrays for wireless sensor networks," *Computers & Electrical Engineering*, vol. 36, no. 6, pp. 1181–1186, 2010. 9

[43] J. Graefenstein, A. Albert, P. Biber, and A. Schilling, "Wireless node localization based on rssi using a rotating antenna on a mobile robot," in *2009 6th Workshop on Positioning, Navigation and Communication*, pp. 253–259, IEEE, 2009. 9, 11

[44] J.-R. Jiang, C.-M. Lin, F.-Y. Lin, and S.-T. Huang, "Alrd: Aoa localization with rssi differences of directional antennas for wireless sensor networks," *International Journal of Distributed Sensor Networks*, vol. 9, no. 3, p. 529489, 2013. 10

[45] R. Peng and M. L. Sichitiu, "Angle of arrival localization for wireless sensor networks," in *2006 3rd annual IEEE communications society on sensor and ad hoc communications and networks*, vol. 1, pp. 374–382, Ieee, 2006. 10, 11

[46] M. R. Kamarudin, Y. I. Nechayev, and P. S. Hall, "Onbody diversity and angle-of-arrival measurement using a pattern switching antenna," *IEEE Transactions on Antennas and Propagation*, vol. 57, no. 4, pp. 964–971, 2009. 10

[47] M. F. B. Jamlos, T. B. A. Rahman, M. R. Kamarudin, P. Saad, O. A. Aziz, and M. A. Shamsudin, "Adaptive beam steering of rlsa antenna with rfid technology," *Progress In Electromagnetics Research*, vol. 108, pp. 65–80, 2010. 11

[48] M. F. B. Jamlos, T. B. A. Rahman, M. R. Kamarudin, P. Saad, M. A. Shamsudin, and A. Dahlan, "A novel adaptive wi-fi system with rfid technology," *Progress In Electromagnetics Research*, vol. 108, pp. 417–432, 2010. 11

[49] M. Malajner, Ž. Čučej, and D. Gleich, "Angle of arrival estimation using a single omnidirectional rotatable antenna," in *2012 IEEE International Conference on Wireless Information Technology and Systems (ICWITS)*, pp. 1–4, IEEE, 2012. 11

[50] B. N. Hood and P. Barooah, "Estimating doa from radio-frequency rssi measurements using an actuated reflector," *IEEE Sensors Journal*, vol. 11, no. 2, pp. 413–417, 2010. 11

[51] P. Xu, B. Yan, and S. Hu, "Angle of arrival (aoa)-based cross-localization algorithm using orientation angle for improved target estimation in far-field environments," *International Jounal of Simulation Systems, Science & Technology*, vol. 17, pp. 20–1, 2016. 11

[52] Y. Norouzi, E. S. Kashani, and A. Ajorloo, "Angle of arrival-based target localisation with low earth orbit satellite observer," *IET Radar, Sonar & Navigation*, vol. 10, no. 7, pp. 1186–1190, 2016. 11

[53] A. Badawy, T. Khattab, D. Trinchero, T. M. Elfouly, and A. Mohamed, "A simple cross correlation switched beam system (xsbs) for angle of arrival estimation," *IEEE Access*, vol. 5, pp. 3340–3352, 2017. 11

[54] A. Chamseddine, O. Akhrif, F. Gagnon, and D. Couillard, "Communication relay for multi-ground units using unmanned aircraft," in *2016 14th International Conference on Control, Automation, Robotics and Vision (ICARCV)*, pp. 1–6, IEEE, 2016. 11

[55] M. Dirix and D. Heberling, "Full-sphere angle of arrival detection using cmrclean," *IEEE Transactions on Antennas and Propagation*, vol. 65, no. 5, pp. 2769–2772, 2017. 11

[56] J. Moghaddasi, T. Djerafi, and K. Wu, "Multiport interferometer-enabled 2-d angle of arrival (aoa) estimation system," *IEEE Transactions on Microwave Theory and Techniques*, vol. 65, no. 5, pp. 1767–1779, 2017. 11

[57] L. Zimmermann, A. Goetz, G. Fischer, and R. Weigel, "Performance analysis of time difference of arrival and angle of arrival estimation methods

for gsm mobile phone localization," *Communication, Signal Processing & Information Technology*, vol. 4, p. 17, 2017. 12

[58] A. Dempster, "Dilution of precision in angle-of-arrival positioning systems," *Electronics Letters*, vol. 42, no. 5, pp. 291–292, 2006. 12

[59] A. H. Sayed, A. Tarighat, and N. Khajehnouri, "Network-based wireless location: challenges faced in developing techniques for accurate wireless location information," *IEEE signal processing magazine*, vol. 22, no. 4, pp. 24–40, 2005. 12

[60] J. Uren and B. Price, *Surveying for engineers*. Bloomsbury Publishing, 2018. 12

[61] C. Wong, R. Klukas, and G. G. Messier, "Using wlan infrastructure for angle-of-arrival indoor user location," in *2008 IEEE 68th Vehicular Technology Conference*, pp. 1–5, IEEE, 2008. 12

[62] D.-H. Jung, H.-S. Kang, C.-K. Kim, J. Park, and S.-O. Park, "Sparse scene recovery for high-resolution automobile fmcw sar via scaled compressed sensing," *IEEE Transactions on Geoscience and Remote Sensing*, vol. 57, no. 12, pp. 10136–10146, 2019. 13

[63] C. Ding, H. Hong, Y. Zou, H. Chu, X. Zhu, F. Fioranelli, J. Le Kernec, and C. Li, "Continuous human motion recognition with a dynamic range-doppler trajectory method based on fmcw radar," *IEEE Transactions on Geoscience and Remote Sensing*, vol. 57, no. 9, pp. 6821–6831, 2019. 13

[64] Y. Nan, X. Huang, and Y. J. Guo, "A millimeter-wave gcw-sar based on deramp-on-receive and piecewise constant doppler imaging," *IEEE Transactions on Geoscience and Remote Sensing*, vol. 58, no. 1, pp. 680–690, 2019. 13

[65] C. Q. Mayoral, C. G. González, J. C. I. Galarregui, D. Marín, D. Gastón, C. Miranda, R. Gonzalo, I. Maestrojuán, L. G. Santesteban, and I. Ederra, "Water content continuous monitoring of grapevine xylem tissue using a portable low-power cost-effective fmcw radar," *IEEE Transactions on Geoscience and Remote Sensing*, vol. 57, no. 8, pp. 5595–5605, 2019. 13

[66] B. Vandersmissen, N. Knudde, A. Jalalvand, I. Couckuyt, A. Bourdoux, W. De Neve, and T. Dhaene, "Indoor person identification using a low-power fmcw radar," *IEEE Transactions on Geoscience and Remote Sensing*, vol. 56, no. 7, pp. 3941–3952, 2018. 13

[67] M. A. Richards, *Fundamentals of radar signal processing*. McGraw-Hill Education, 2014. 13

[68] J. Lin Jr, Y.-P. Li, W.-C. Hsu, and T.-S. Lee, "Design of an fmcw radar baseband signal processing system for automotive application," *SpringerPlus*, vol. 5, no. 1, pp. 1–16, 2016. 13

[69] K. Kulpa and Z. Czekała, "Masking effect and its removal in pcl radar," *IEE Proceedings-Radar, Sonar and Navigation*, vol. 152, no. 3, pp. 174–178, 2005. 13, 16

[70] D. Kocur, J. Rovňáková, and D. Urdzík, "Experimental analyses of mutual shadowing effect for multiple target tracking by uwb radar," in *2011 IEEE 7th International Symposium on Intelligent Signal Processing*, pp. 1–4, IEEE, 2011. 13, 15, 16, 74, 80

[71] D. Kocur, J. Rovňáková, and D. Urdzík, "Mutual shadowing effect of people tracked by the short-range uwb radar," in *2011 34th International Conference on Telecommunications and Signal Processing (TSP)*, pp. 302–306, IEEE, 2011. 13, 15, 16, 74

[72] D. Urdzík, R. Zetík, D. Kocur, and J. Rovnáková, "Shadowing effect investigation for the purposes of person detection and tracking by uwb radars," in *2012 The 7th German Microwave Conference*, pp. 1–4, IEEE, 2012. 13, 16

[73] H. Xue, M. Liu, H. Lv, T. Jiao, Z. Li, F. Qi, P. Wang, J. Wang, and Y. Zhang, "A dynamic clutter interference suppression method for multiple static human targets detection using ultra-wideband radar," *Microwave and Optical Technology Letters*, vol. 61, no. 12, pp. 2854–2865, 2019. 13, 16

[74] H. Xue, M. Liu, Y. Zhang, F. Liang, F. Qi, F. Chen, H. Lv, and J. Wang, "An algorithm based wavelet entropy for shadowing effect of human detection using ultra-wideband bio-radar," *Sensors*, vol. 17, no. 10, p. 2255, 2017. 13, 14, 15, 16, 74, 91

[75] L. Claudepierre, R. Douvenot, A. Chabory, and C. Morlaas, "Assessment of the shadowing effect between windturbines at vor and radar frequencies.," 01 2016. 13, 16

[76] F. Perez Fontan and P. Espiñeira, *Shadowing Effects*, pp. 29–60. 08 2008. 13, 16

[77] J. Fortes and D. Kocur, "Solutions of mutual shadowing effect between people tracked by uwb radar," pp. 1–5, 10 2013. 13, 16

[78] *radar shadow*, pp. 1069–1069. Berlin, Heidelberg: Springer Berlin Heidelberg, 2014. 13, 16

[79] N. O'Mahony, S. Campbell, A. Carvalho, S. Harapanahalli, G. V. Hernandez, L. Krpalkova, D. Riordan, and J. Walsh, "Deep learning vs. traditional computer vision," in *Science and Information Conference*, pp. 128–144, Springer, 2019. 14

[80] S. Heuel and H. Rohling, "Pedestrian classification in automotive radar systems," in *2012 13th international radar symposium*, pp. 39–44, IEEE, 2012. 14

[81] Z. Zhang, Z. Tian, and M. Zhou, "Latern: Dynamic continuous hand gesture recognition using fmcw radar sensor," *IEEE Sensors Journal*, vol. 18, no. 8, pp. 3278–3289, 2018. 14, 17

[82] M. Hussain, J. J. Bird, and D. R. Faria, "A study on cnn transfer learning for image classification," in *UK Workshop on computational Intelligence*, pp. 191–202, Springer, 2018. 14

[83] H. Lee and H. Kwon, "Going deeper with contextual cnn for hyperspectral image classification," *IEEE Transactions on Image Processing*, vol. 26, no. 10, pp. 4843–4855, 2017. 14

[84] M. Huh, P. Agrawal, and A. A. Efros, "What makes imagenet good for transfer learning?," *arXiv preprint arXiv:1608.08614*, 2016. 14

[85] N. Thi Phuoc Van, L. Tang, V. Demir, S. F. Hasan, N. Duc Minh, and S. Mukhopadhyay, "Microwave radar sensing systems for search and rescue purposes," *Sensors*, vol. 19, no. 13, p. 2879, 2019. 14

[86] K. Huang, J. Zhong, J. Zhu, X. Zhang, F. Zhao, H. Xie, F. Gu, B. Zhou, and M. Wu, "The method of forest fires recognition by using doppler weather radar," in *Proc. 8th Symp. Fire Forest Meteorol.*, pp. 1–7, 2007. 14

[87] A. Capria, E. Giusti, C. Moscardini, M. Conti, D. Petri, M. Martorella, and F. Berizzi, "Multifunction imaging passive radar for harbour protection and navigation safety," *IEEE Aerospace and Electronic Systems Magazine*, vol. 32, no. 2, pp. 30–38, 2017. 15

[88] F. Lemaitre and J.-C. Poussieres, "Method and system for sensing and locating a person, eg under an avalanche," 2000. US Patent 6,031,482. 15

[89] A. Rizik, A. Randazzo, R. Vio, A. Delucchi, H. Chible, and D. D. Caviglia, "Low-cost fmcw radar human-vehicle classification based on transfer learning," in *2020 32nd International Conference on Microelectronics (ICM)*, pp. 1–4, IEEE, 2020. 15

[90] N. Maaref, P. Millot, C. Pichot, and O. Picon, "Fmcw ultra-wideband radar for through-the-wall detection of human beings," in *2009 International Radar Conference" Surveillance for a Safer World"(RADAR 2009)*, pp. 1–5, IEEE, 2009. 15, 17, 74

[91] H. Zhou, B. Wen, Z. Ma, and S. Wu, "Range/doppler ambiguity elimination in high-frequency chirp radars," *IEE Proceedings-Radar, Sonar and Navigation*, vol. 153, no. 6, pp. 467–472, 2006. 16, 75

[92] A. Rizik, E. Tavanti, H. Chible, D. D. Caviglia, and A. Randazzo, "Cost-efficient fmcw radar for multi-target classification in security gate monitoring," *IEEE Sensors Journal*, vol. 21, no. 18, pp. 20447–20461, 2021. 17, 84

[93] G. Sacco, E. Piuzzi, E. Pittella, and S. Pisa, "An fmcw radar for localization and vital signs measurement for different chest orientations," *Sensors*, vol. 20, no. 12, p. 3489, 2020. 17

[94] Z. Peng, L. Ran, and C. Li, "A k-band portable fmcw radar with beamforming array for short-range localization and vital-doppler targets discrimination," *IEEE Transactions on Microwave Theory and Techniques*, vol. 65, no. 9, pp. 3443–3452, 2017. 17

[95] K. Han and S. Hong, "Vocal signal detection and speaking-human localization with mimo fmcw radar," *IEEE Transactions on Microwave Theory and Techniques*, vol. 69, no. 11, pp. 4791–4802, 2021. 17

[96] J. Cong, X. Wang, X. Lan, M. Huang, and L. Wan, "Fast target localization method for fmcw mimo radar via vdsr neural network," *Remote Sensing*, vol. 13, no. 10, p. 1956, 2021. 17

[97] M. Stephan, S. Hazra, A. Santra, R. Weigel, and G. Fischer, "People counting solution using an fmcw radar with knowledge distillation from camera data," 11 2021. 17

[98] C. Will, P. Vaishnav, A. Chakraborty, and A. Santra, "Human target detection, tracking, and classification using 24-ghz fmcw radar," *IEEE Sensors Journal*, vol. 19, no. 17, pp. 7283–7299, 2019. 17

[99] P. Vaishnav and A. Santra, "Continuous human activity classification with unscented kalman filter tracking using fmcw radar," *IEEE Sensors Letters*, vol. 4, no. 5, pp. 1–4, 2020. 17

[100] G. Wang, C. Gu, T. Inoue, and C. Li, "A hybrid fmcw-interferometry radar for indoor precise positioning and versatile life activity monitoring," *IEEE Transactions on Microwave Theory and Techniques*, vol. 62, no. 11, pp. 2812–2822, 2014. 17

[101] A. Angelov, A. Robertson, R. Murray-Smith, and F. Fioranelli, "Practical classification of different moving targets using automotive radar and deep neural networks," *IET Radar, Sonar & Navigation*, vol. 12, no. 10, pp. 1082–1089, 2018. 17

[102] S. Abdulatif, Q. Wei, F. Aziz, B. Kleiner, and U. Schneider, "Micro-doppler based human-robot classification using ensemble and deep learning ap-

proaches," in *2018 IEEE Radar Conference (RadarConf18)*, pp. 1043–1048, IEEE, 2018. 17

[103] R. Khanna, D. Oh, and Y. Kim, "Through-wall remote human voice recognition using doppler radar with transfer learning," *IEEE Sensors Journal*, vol. 19, no. 12, pp. 4571–4576, 2019. 17

[104] A. Bhattacharya and R. Vaughan, "Deep learning radar design for breathing and fall detection," *IEEE Sensors Journal*, vol. 20, no. 9, pp. 5072–5085, 2020. 17

[105] X. Huang, J. Ding, D. Liang, and L. Wen, "Multi-person recognition using separated micro-doppler signatures," *IEEE Sensors Journal*, vol. 20, no. 12, pp. 6605–6611, 2020. 17

[106] S. Kim, K. Lee, S. Doo, and B. Shim, "Automotive radar signal classification using bypass recurrent convolutional networks," in *2019 IEEE/CIC International Conference on Communications in China (ICCC)*, pp. 798–803, IEEE, 2019. 17

[107] Y. Kim, I. Alnujaim, S. You, and B. J. Jeong, "Human detection based on time-varying signature on range-doppler diagram using deep neural networks," *IEEE Geoscience and Remote Sensing Letters*, vol. 18, no. 3, pp. 426–430, 2020. 17, 97, 100

[108] M. Ronthal, "Gait disorders and falls in the elderly," *Medical Clinics*, vol. 103, no. 2, pp. 203–213, 2019. 17

[109] P. Pace, G. Aloi, R. Gravina, G. Caliciuri, G. Fortino, and A. Liotta, "An edge-based architecture to support efficient applications for healthcare industry 4.0," *IEEE Transactions on Industrial Informatics*, vol. 15, no. 1, pp. 481–489, 2019. 17

[110] A. Shahzad and K. Kim, "Falldroid: An automated smart-phone-based fall detection system using multiple kernel learning," *IEEE Transactions on Industrial Informatics*, vol. 15, no. 1, pp. 35–44, 2018. 17

[111] C. Wang, W. Lu, M. R. Narayanan, D. C. W. Chang, S. R. Lord, S. J. Redmond, and N. H. Lovell, "Low-power fall detector using triaxial accelerometry and barometric pressure sensing," *IEEE Transactions on Industrial Informatics*, vol. 12, no. 6, pp. 2302–2311, 2016. 17

[112] W. Saadeh, S. A. Butt, and M. A. B. Altaf, "A patient-specific single sensor iot-based wearable fall prediction and detection system," *IEEE transactions on neural systems and rehabilitation engineering*, vol. 27, no. 5, pp. 995–1003, 2019. 17

[113] A. B. Mesanza, I. D'Ascanio, A. Zubizarreta, L. Palmerini, L. Chiari, and I. Cabanes, "Machine learning based fall detector with a sensorized tip," *IEEE Access*, vol. 9, pp. 164106–164117, 2021. 17

[114] M. Yu, A. Rhuma, S. M. Naqvi, L. Wang, and J. Chambers, "A posture recognition-based fall detection system for monitoring an elderly person in a smart home environment," *IEEE transactions on information technology in biomedicine*, vol. 16, no. 6, pp. 1274–1286, 2012. 18

[115] E. Akagündüz, M. Aslan, A. Şengür, H. Wang, and M. C. Ince, "Silhouette orientation volumes for efficient fall detection in depth videos," *IEEE journal of biomedical and health informatics*, vol. 21, no. 3, pp. 756–763, 2016. 18

[116] G. Chen, S. Qu, Z. Li, H. Zhu, J. Dong, M. Liu, and J. Conradt, "Neuromorphic vision-based fall localization in event streams with temporal-spatial attention weighted network," *IEEE transactions on cybernetics*, 2022. 18

[117] K. Krishnapriya, V. Albiero, K. Vangara, M. C. King, and K. W. Bowyer, "Issues related to face recognition accuracy varying based on race and skin tone," *IEEE Transactions on Technology and Society*, vol. 1, no. 1, pp. 8–20, 2020. 18

[118] S. Moulik and S. Majumdar, "Fallsense: An automatic fall detection and alarm generation system in iot-enabled environment," *IEEE Sensors Journal*, vol. 19, no. 19, pp. 8452–8459, 2018. 18

[119] H. Wang, D. Zhang, Y. Wang, J. Ma, Y. Wang, and S. Li, "Rt-fall: A real-time and contactless fall detection system with commodity wifi devices," *IEEE Transactions on Mobile Computing*, vol. 16, no. 2, pp. 511–526, 2016. 18

[120] S. Z. Gurbuz and M. G. Amin, "Radar-based human-motion recognition with deep learning: Promising applications for indoor monitoring," *IEEE Signal Processing Magazine*, vol. 36, no. 4, pp. 16–28, 2019. 18

[121] M. G. Amin, Y. D. Zhang, F. Ahmad, and K. D. Ho, "Radar signal processing for elderly fall detection: The future for in-home monitoring," *IEEE Signal Processing Magazine*, vol. 33, no. 2, pp. 71–80, 2016. 18

[122] M. Forouzanfar, M. Mabrouk, S. Rajan, M. Bolic, H. R. Dajani, and V. Z. Groza, "Event recognition for contactless activity monitoring using phase-modulated continuous wave radar," *IEEE transactions on biomedical engineering*, vol. 64, no. 2, pp. 479–491, 2016. 18

[123] C. Ding, L. Zhang, C. Gu, L. Bai, Z. Liao, H. Hong, Y. Li, and X. Zhu, "Non-contact human motion recognition based on uwb radar," *IEEE Journal on Emerging and Selected Topics in Circuits and Systems*, vol. 8, no. 2, pp. 306–315, 2018. 18, 112

[124] B. Jokanović and M. Amin, "Fall detection using deep learning in range-doppler radars," *IEEE Transactions on Aerospace and Electronic Systems*, vol. 54, no. 1, pp. 180–189, 2017. 18, 112

[125] M. S. Seyfioğlu, A. M. Özbayoğlu, and S. Z. Gürbüz, "Deep convolutional autoencoder for radar-based classification of similar aided and unaided human activities," *IEEE Transactions on Aerospace and Electronic Systems*, vol. 54, no. 4, pp. 1709–1723, 2018. 18, 112

[126] H. Sadreazami, M. Bolic, and S. Rajan, "Fall detection using standoff radar-based sensing and deep convolutional neural network," *IEEE Transactions on Circuits and Systems II: Express Briefs*, vol. 67, no. 1, pp. 197–201, 2019. 19, 112, 113

[127] H. Li, A. Shrestha, H. Heidari, J. Le Kernec, and F. Fioranelli, "Bi-lstm network for multimodal continuous human activity recognition and fall detection," *IEEE Sensors Journal*, vol. 20, no. 3, pp. 1191–1201, 2019. 19, 112

[128] A. Shrestha, H. Li, J. Le Kernec, and F. Fioranelli, "Continuous human activity classification from fmcw radar with bi-lstm networks," *IEEE Sensors Journal*, vol. 20, no. 22, pp. 13607–13619, 2020. 19, 112

[129] B. Erol, S. Z. Gurbuz, and M. G. Amin, "Motion classification using kinematically sifted acgan-synthesized radar micro-doppler signatures," *IEEE Transactions on Aerospace and Electronic Systems*, vol. 56, no. 4, pp. 3197–3213, 2020. 19, 112

[130] H. Sadreazami, M. Bolic, and S. Rajan, "Contactless fall detection using time-frequency analysis and convolutional neural networks," *IEEE Trans-*

actions on Industrial Informatics, vol. 17, no. 10, pp. 6842–6851, 2021. 19, 112

[131] M. He, Y. Yang, Q. Ping, R. Dai, B. Liu, Y. Nian, and Z. Zhang, "Optimum target range bin selection method for time-frequency analysis to detect falls using wideband radar and a lightweight network," *Biomedical Signal Processing and Control*, vol. 77, p. 103741, 2022. 19, 112

[132] P. Khomchuk, I. Stainvas, and I. Bilik, "Pedestrian motion direction estimation using simulated automotive mimo radar," *IEEE Transactions on Aerospace and Electronic Systems*, vol. 52, no. 3, pp. 1132–1145, 2016. 21

[133] G. Wang, J. Xin, J. Wang, N. Zheng, and A. Sano, "Subspace-based two-dimensional direction estimation and tracking of multiple targets," *IEEE Transactions on Aerospace and Electronic Systems*, vol. 51, no. 2, pp. 1386–1402, 2015. 21

[134] Z. Lu, Y. Li, and M. Gao, "Direction estimation for two steady targets in monopulse radar," *Journal of Systems Engineering and Electronics*, vol. 26, no. 1, pp. 61–68, 2015. 21

[135] N. Iliev and I. Paprotny, "Review and comparison of spatial localization methods for low-power wireless sensor networks," *IEEE Sensors Journal*, vol. 15, no. 10, pp. 5971–5987, 2015. 21

[136] T. D. Bui, B. H. Nguyen, Q. C. Nguyen, M. T. Le, *et al.*, "Design of beam steering antenna for localization applications," in *2016 International Symposium on Antennas and Propagation (ISAP)*, pp. 956–957, IEEE, 2016. 21

[137] R. Poisel, *Electronic warfare target location methods*. Artech House, 2012. 21

[138] F. Gross, "Smart antennas for wireless communications with matlab," *McGraw Hills*, 2005. 21

[139] W. Y. Yang, *MATLAB/Simulink for Digital Signal Processing*. Won Y. Yang, 2015. 21

[140] C. Siagian, C. K. Chang, and L. Itti, "Autonomous mobile robot localization and navigation using a hierarchical map representation primarily guided by vision," *Journal of Field Robotics*, vol. 31, no. 3, pp. 408–440, 2014. 21

[141] C.-H. Lin and K.-T. Song, "Probability-based location aware design and on-demand robotic intrusion detection system," *IEEE Transactions on Systems, Man, and Cybernetics: Systems*, vol. 44, no. 6, pp. 705–715, 2013. 21

[142] H. Cheng, H. Chen, and Y. Liu, "Topological indoor localization and navigation for autonomous mobile robot," *IEEE Transactions on Automation Science and Engineering*, vol. 12, no. 2, pp. 729–738, 2014. 21

[143] P. J. Costa, N. Moreira, D. Campos, J. Gonçalves, J. Lima, and P. L. Costa, "Localization and navigation of an omnidirectional mobile robot: the robot@ factory case study," *IEEE Revista Iberoamericana de Tecnologias del Aprendizaje*, vol. 11, no. 1, pp. 1–9, 2016. 21

[144] L. Paull, S. Saeedi, M. Seto, and H. Li, "Auv navigation and localization: A review," *IEEE Journal of oceanic engineering*, vol. 39, no. 1, pp. 131–149, 2013. 21

[145] M. Dredze, M. J. Paul, S. Bergsma, and H. Tran, "Carmen: A twitter geolocation system with applications to public health," in *Workshops at the twenty-seventh AAAI conference on artificial intelligence*, 2013. 21

[146] J. He, K. Pahlavan, S. Li, and Q. Wang, "A testbed for evaluation of the effects of multipath on performance of toa-based indoor geolocation," *IEEE transactions on instrumentation and measurement*, vol. 62, no. 8, pp. 2237–2247, 2013. 21

[147] A. Redondi, M. Chirico, L. Borsani, M. Cesana, and M. Tagliasacchi, "An integrated system based on wireless sensor networks for patient monitoring, localization and tracking," *Ad Hoc Networks*, vol. 11, no. 1, pp. 39–53, 2013. 21

[148] T. Instruments, "Boostxl-aoa antenna." Accessed 15-July-2022. 26, 50

[149] T. Instruments, "Cc2640r2f." Accessed 15-July-2022. 28, 50

[150] T. Instruments, "Cc1352r." Accessed 15-July-2022. 29, 50

[151] L. Yang, X. Feng, J. Zhang, and X. Shu, "Multi-ray modeling of ultrasonic sensors and application for micro-uav localization in indoor environments," *Sensors*, vol. 19, no. 8, p. 1770, 2019. 33

[152] C. Li, L. Mo, and D. Zhang, "Review on uhf rfid localization methods," *IEEE Journal of Radio Frequency Identification*, vol. 3, no. 4, pp. 205–215, 2019. 33

[153] R. Kimoto, T. Yamamoto, S. Ishida, S. Tagashira, and A. Fukuda, "Evaluation of multizigloc: Indoor zigbee localization system using inter-channel characteristics," in *2018 Eleventh International Conference on Mobile Computing and Ubiquitous Network (ICMU)*, pp. 1–6, IEEE, 2018. 33

[154] R. Giuliano, G. C. Cardarilli, C. Cesarini, L. Di Nunzio, F. Fallucchi, R. Fazzolari, F. Mazzenga, M. Re, and A. Vizzarri, "Indoor localization

system based on bluetooth low energy for museum applications," *Electronics*, vol. 9, no. 6, p. 1055, 2020. 33, 46

[155] A. Thaljaoui, T. Val, N. Nasri, and D. Brulin, "Ble localization using rssi measurements and iringla," in *2015 IEEE international conference on industrial technology (ICIT)*, pp. 2178–2183, IEEE, 2015. 33, 46

[156] C. M. Lamacchia, M. Gallo, L. Mescia, P. Bia, A. Manna, C. Canestri, and D. Gaetano, "Non-conventional cavity backed sinuous antenna for uwb radar applications," in *2020 IEEE International Symposium on Antennas and Propagation and North American Radio Science Meeting*, pp. 109–110, IEEE, 2020. 43

[157] N. El Agroudy, G. Georgiades, N. Joram, and F. Ellinger, "Rssi overboard localization system for safe evacuation of large passengers ships," in *2017 13th Conference on Ph. D. Research in Microelectronics and Electronics (PRIME)*, pp. 177–180, IEEE, 2017. 45, 46, 57

[158] A. H. Salamah, M. Tamazin, M. A. Sharkas, M. Khedr, and M. Mahmoud, "Comprehensive investigation on principle component large-scale wi-fi indoor localization," *Sensors*, vol. 19, no. 7, p. 1678, 2019. 45

[159] K. Y. Seok, J. Y. Ryu, and J. H. Lee, "Risk-aware wireless positioning in maritime environment," *Applied Sciences*, vol. 9, no. 10, p. 2107, 2019. 45, 46

[160] S. Aronica, F. Benvegna, M. Cossentino, S. Gaglio, A. Langiu, C. Lodato, S. Lopes, U. Maniscalco, and P. Sangiorgi, "An agent-based system for maritime search and rescue operations.," in *WOA*, 2010. 45, 46

[161] N. A. Alrajeh, M. Bashir, and B. Shams, "Localization techniques in wireless sensor networks," *International journal of distributed sensor networks*, vol. 9, no. 6, p. 304628, 2013. 45

[162] H. Obeidat, W. Shuaieb, O. Obeidat, and R. Abd-Alhameed, "A review of indoor localization techniques and wireless technologies," *Wireless Personal Communications*, vol. 119, no. 1, pp. 289–327, 2021. 67

[163] H. Li, J. Yu, and Q. Gao, "Patent analysis reveals the development route of the indoor high-accuracy positioning technology," in *China Satellite Navigation Conference*, pp. 587–594, Springer, 2020. 67

[164] F. Zafari, A. Gkelias, and K. K. Leung, "A survey of indoor localization systems and technologies," *IEEE Communications Surveys & Tutorials*, vol. 21, no. 3, pp. 2568–2599, 2019. 67

[165] E. Lee, H. Bae, H. Kim, H. Han, Y. Lee, and J. Son, "Trends in ai technology for smart manufacturing in the future," *Electronics and telecommunications trends*, vol. 35, no. 1, pp. 60–70, 2020. 67

[166] R. Kimoto, S. Ishida, T. Yamamoto, S. Tagashira, and A. Fukuda, "Muchloc: Indoor zigbee localization system utilizing inter-channel characteristics," *Sensors*, vol. 19, no. 7, p. 1645, 2019. 67

[167] Y. Tao, L. Wu, J. Sidén, and G. Wang, "Monte carlo-based indoor rfid positioning with dual-antenna joint rectification," *Electronics*, vol. 10, no. 13, p. 1548, 2021. 67

[168] S.-C. Kim, Y.-S. Jeong, and S.-O. Park, "Rfid-based indoor location tracking to ensure the safety of the elderly in smart home environments," *Personal and ubiquitous computing*, vol. 17, no. 8, pp. 1699–1707, 2013. 67

[169] Y. Yun, Y. Park, B. M. Lee, B. Hyun, and Y. Kim, "Distance estimation scheme exploiting ir-uwb radar with clutter suppressing algorithm in indoor environments," *Journal of Electrical Engineering & Technology*, vol. 14, no. 4, pp. 1759–1769, 2019. 67

[170] S. Kim, D. Oh, and J. Lee, "Joint dft-esprit estimation for toa and doa in vehicle fmcw radars," *IEEE Antennas and Wireless Propagation Letters*, vol. 14, pp. 1710–1713, 2015. 67

[171] S. Yang, C. Sun, and Y. Kim, "Indoor 3d localization scheme based on ble signal fingerprinting and 1d convolutional neural network," *Electronics*, vol. 10, no. 15, p. 1758, 2021. 67

[172] S. Yang, C. Sun, and Y. Kim, "A new rigid body localization scheme exploiting participatory search algorithm," *Journal of Electrical Engineering & Technology*, vol. 15, no. 6, pp. 2777–2784, 2020. 67, 68

[173] H. Jeon, U. Jo, M. Jo, N. Kim, and Y. Kim, "An adaptive ap selection scheme based on rss for enhancing positioning accuracy," *Wireless personal communications*, vol. 69, no. 4, pp. 1535–1550, 2013. 67

[174] V. K. Jain, S. Tapaswi, and A. Shukla, "Location estimation based on semi-supervised locally linear embedding (sslle) approach for indoor wireless networks," *Wireless Personal Communications*, vol. 67, no. 4, pp. 879–893, 2012. 67

[175] S. Lee, J.-Y. Lee, and S.-C. Kim, "Mutual interference suppression using wavelet denoising in automotive fmcw radar systems," *IEEE Transactions on Intelligent Transportation Systems*, vol. 22, no. 2, pp. 887–897, 2019. 68

[176] J. Han, "Study on 24 ghz short range radar system using delayed fmcw signal," 2014. 68

[177] N. Kim, M. Yu, and S. Lee, "A method for improving range estimation accuracy in narrowband indoor fmcw radar range sensors," in *Proc. Ann. Conf. IEIE*, vol. 26, pp. 345–348, 2019. 68

[178] B. Al-Qudsi, M. El-Shennawy, N. Joram, and F. Ellinger, "A coverage efficient fmcw positioning system," in *2016 International Conference on Localization and GNSS (ICL-GNSS)*, pp. 1–6, IEEE, 2016. 68

[179] I. Technologies, "Postiion2go." Accessed 15-July-2022. 69

[180] M. Jankiraman, *Design of multi-frequency CW radars*, vol. 2. SciTech Publishing, 2007. 72

[181] "Infenion position2go board." `https://www.infineon.com/cms/en/product/evaluation-boards/demo-position2go/`. Accessed: 2021-12-17. 75, 91

[182] L. Nicolaescu and T. Oroian, "Radar cross section," in *5th International Conference on Telecommunications in Modern Satellite, Cable and Broadcasting Service. TELSIKS 2001. Proceedings of Papers (Cat. No. 01EX517)*, vol. 1, pp. 65–68, IEEE, 2001. 79

[183] A. Howard, M. Sandler, G. Chu, L.-C. Chen, B. Chen, M. Tan, W. Wang, Y. Zhu, R. Pang, V. Vasudevan, *et al.*, "Searching for mobilenetv3," in *Proceedings of the IEEE/CVF International Conference on Computer Vision*, pp. 1314–1324, 2019. 82, 90

[184] "Deep neural networks." `https:/keras.io/api/applications/`. Accessed: 2021-12-17. 82

[185] Infenion, "Position2go radar." Accessed: 15-June-2022. 94, 100, 101

[186] E. Tavanti, A. Rizik, A. Fedeli, D. D. Caviglia, and A. Randazzo, "A short-range fmcw radar-based approach for multi-target human-vehicle detection," *IEEE Transactions on Geoscience and Remote Sensing*, vol. 60, pp. 1–16, 2022. 94, 95, 106

[187] C. Shorten and T. M. Khoshgoftaar, "A survey on image data augmentation for deep learning," *Journal of big data*, vol. 6, no. 1, pp. 1–48, 2019. 95

[188] A. Rizik, E. Tavanti, H. Chible, D. D. Caviglia, and A. Randazzo, "Cost-efficient fmcw radar for multi-target classification in security gate monitoring," *IEEE Sensors Journal*, vol. 21, no. 18, pp. 20447–20461, 2021. 106

[189] A. U. Ahmed, M. T. Islam, and M. Ismail, "Estimating doa from radio frequency rssi measurements using multi-element femtocell configuration," *IEEE sensors journal*, vol. 15, no. 4, pp. 2087–2092, 2014.

[190] M. Edrich, "Ultra-lightweight synthetic aperture radar based on a 35 ghz fmcw sensor concept and online raw data transmission," *IEE Proceedings-Radar, Sonar and Navigation*, vol. 153, no. 2, pp. 129–134, 2006.

[191] A. Rizik, E. Tavanti, R. Vio, A. Delucchi, H. Chible, A. Randazzo, and D. D. Caviglia, "Single target recognition using a low-cost fmcw radar based on spectrum analysis," in *2020 27th IEEE International Conference on Electronics, Circuits and Systems (ICECS)*, pp. 1–4, IEEE, 2020.

[192] Y. Wang, X. Yu, Y. Zhang, H. Lv, T. Jiao, G. Lu, W. Z. Li, Z. Li, X. Jing, and J. Wang, "Using wavelet entropy to distinguish between humans and dogs detected by uwb radar," *Progress In Electromagnetics Research*, vol. 139, pp. 335–352, 2013.

[193] V. Chernyak, "Signal processing in multisite uwb radar devices for searching

survivors in rubble," in *2006 European Radar Conference*, pp. 190–193, IEEE, 2006.

[194] J. Lei and C. Lu, "Target classification based on micro-doppler signatures," in *IEEE International Radar Conference, 2005.*, pp. 179–183, IEEE, 2005.

[195] *radar shadow*. 01 2014.

[196] S. Hazra and A. Santra, "Short-range radar-based gesture recognition system using 3d cnn with triplet loss," *IEEE Access*, vol. 7, pp. 125623–125633, 2019.

[197] Infenion, "Position2go radar applications." Accessed 15-June-2022.

[198] G. TensorFlow, "TF–Lite Clustering." Accessed 15-June-2022.

[199] S. Hochreiter and J. Schmidhuber, "Long short-term memory," *Neural computation*, vol. 9, no. 8, pp. 1735–1780, 1997.

[200] K. You, M. Long, J. Wang, and M. I. Jordan, "How does learning rate decay help modern neural networks?," *arXiv preprint arXiv:1908.01878*, 2019.

[201] L. Prechelt, "Early stopping-but when?," in *Neural Networks: Tricks of the trade*, pp. 55–69, Springer, 1998.

[202] D. P. Kingma and J. Ba, "Adam: A method for stochastic optimization," *arXiv preprint arXiv:1412.6980*, 2014.

[203] A. Agarwal, R. Singh, M. Vatsa, and N. Ratha, "Image transformation-based defense against adversarial perturbation on deep learning models," *IEEE Transactions on Dependable and Secure Computing*, vol. 18, no. 5, pp. 2106–2121, 2020.

[204] L. Zhang, X. Wang, D. Yang, T. Sanford, S. Harmon, B. Turkbey, B. J. Wood, H. Roth, A. Myronenko, D. Xu, *et al.*, "Generalizing deep learning for medical image segmentation to unseen domains via deep stacked transformation," *IEEE transactions on medical imaging*, vol. 39, no. 7, pp. 2531–2540, 2020.

[205] G. TensorFlow, "TF–Lite Pruning." Accessed 15-June-2022.

[206] G. TensorFlow, "Tf–lite." Accessed 15-June-2022.

[207] Google, "Coral dev board." Accessed 15-June-2022.

[208] R. Pi, "Raspberry pi4." Accessed 15-June-2022.

[209] A. Mohanna, C. Gianoglio, A. Rizik, and M. Valle, "A convolutional neural network-based method for discriminating shadowed targets in frequency-modulated continuous-wave radar systems," *Sensors*, vol. 22, no. 3, p. 1048, 2022.

[210] X. Du, H. Xu, and F. Zhu, "Understanding the effect of hyperparameter optimization on machine learning models for structure design problems," *Computer-Aided Design*, vol. 135, p. 103013, 2021.

[211] S. Yadav and S. Shukla, "Analysis of k-fold cross-validation over hold-out validation on colossal datasets for quality classification," in *2016 IEEE 6th International conference on advanced computing (IACC)*, pp. 78–83, IEEE, 2016.

[212] X. Yang, L. Shu, Y. Liu, G. P. Hancke, M. A. Ferrag, and K. Huang, "Physical security and safety of iot equipment: A survey of recent advances and opportunities," *IEEE Transactions on Industrial Informatics*, vol. 18, no. 7, pp. 4319–4330, 2022.

[213] F. Visin, K. Kastner, K. Cho, M. Matteucci, A. Courville, and Y. Bengio, "Renet: A recurrent neural network based alternative to convolutional networks," *arXiv preprint arXiv:1505.00393*, 2015.

[214] S. Krishnamurthy, M. Thoppian, S. Kuppa, R. Chandrasekaran, N. Mittal, S. Venkatesan, and R. Prakash, "Time-efficient distributed layer-2 auto-configuration for cognitive radio networks," *Computer Networks*, vol. 52, no. 4, pp. 831–849, 2008.

[215] N. Dhanachandra, K. Manglem, and Y. J. Chanu, "Image segmentation using k-means clustering algorithm and subtractive clustering algorithm," *Procedia Computer Science*, vol. 54, pp. 764–771, 2015.

[216] S. S. Al-Amri, N. Kalyankar, and S. Khamitkar, "Image segmentation by using edge detection," *International journal on computer science and engineering*, vol. 2, no. 3, pp. 804–807, 2010.

[217] O. R. Vincent, O. Folorunso, *et al.*, "A descriptive algorithm for sobel image edge detection," in *Proceedings of informing science & IT education conference (InSITE)*, vol. 40, pp. 97–107, 2009.

[218] C.-X. Deng, G.-B. Wang, and X.-R. Yang, "Image edge detection algorithm based on improved canny operator," in *2013 International Conference on Wavelet Analysis and Pattern Recognition*, pp. 168–172, IEEE, 2013.

[219] M. S. Louis, Z. Azad, L. Delshadtehrani, S. Gupta, P. Warden, V. J. Reddi, and A. Joshi, "Towards deep learning using tensorflow lite on risc-v," in *Third Workshop on Computer Architecture Research with RISC-V (CARRV)*, vol. 1, p. 6, 2019.

[220] Y. Gao, X. Xiang, N. Xiong, B. Huang, H. J. Lee, R. Alrifai, X. Jiang, and

Z. Fang, "Human action monitoring for healthcare based on deep learning," *IEEE Access*, vol. 6, pp. 52277–52285, 2018.

[221] A. Rizik, A. Randazzo, R. Vio, A. Delucchi, H. Chible, and D. D. Caviglia, "Feature extraction for human-vehicle classification in fmcw radar," in *2019 26th IEEE International Conference on Electronics, Circuits and Systems (ICECS)*, pp. 131–132, 2019.

[222] E. Burns and R. Kakara, "Deaths from falls among persons aged $\geq$ 65 years–united states, 2007–2016," *Morbidity and Mortality Weekly Report*, vol. 67, no. 18, p. 509, 2018.

[223] S. Björklund, H. Petersson, and G. Hendeby, "Features for micro-doppler based activity classification," *IET radar, sonar & navigation*, vol. 9, no. 9, pp. 1181–1187, 2015.

[224] Y.-W. Lee, E. Stuntebeck, *et al.*, "Merit: Mesh of rf sensors for indoor tracking," in *2006 3rd Annual IEEE Communications Society on Sensor and Ad Hoc Communications and Networks*, vol. 2, pp. 545–554, IEEE, 2006.

[225] F. Zhang, J. Chen, H. Li, Y. Sun, and X. S. Shen, "Distributed active sensor scheduling for target tracking in ultrasonic sensor networks," *Mobile Networks and Applications*, vol. 17, no. 5, pp. 582–593, 2012.

[226] D. Djenouri, R. Laidi, Y. Djenouri, and I. Balasingham, "Machine learning for smart building applications: Review and taxonomy," *ACM Computing Surveys (CSUR)*, vol. 52, no. 2, pp. 1–36, 2019.

[227] B. Dong, V. Prakash, F. Feng, and Z. O'Neill, "A review of smart building sensing system for better indoor environment control," *Energy and Buildings*, vol. 199, pp. 29–46, 2019.

[228] P. Corbishley and E. Rodriguez-Villegas, "Breathing detection: towards a miniaturized, wearable, battery-operated monitoring system," *IEEE Transactions on Biomedical Engineering*, vol. 55, no. 1, pp. 196–204, 2007.

[229] T. R. Mauldin, M. E. Canby, V. Metsis, A. H. Ngu, and C. C. Rivera, "Smartfall: A smartwatch-based fall detection system using deep learning," *Sensors*, vol. 18, no. 10, p. 3363, 2018.

[230] M. Ahmed, N. Mehmood, A. Nadeem, A. Mehmood, and K. Rizwan, "Fall detection system for the elderly based on the classification of shimmer sensor prototype data," *Healthcare informatics research*, vol. 23, no. 3, pp. 147–158, 2017.

[231] G. G. Torres, R. V. B. Henriques, C. E. Pereira, and I. Müller, "An enocean wearable device with fall detection algorithm integrated with a smart home system," *IFAC-PapersOnLine*, vol. 51, no. 10, pp. 9–14, 2018.

[232] M. Ko, S. Kim, M. Kim, and K. Kim, "A novel approach for outdoor fall detection using multidimensional features from a single camera," *Applied Sciences*, vol. 8, no. 6, p. 984, 2018.

[233] G. Mastorakis and D. Makris, "Fall detection system using kinect's infrared sensor," *Journal of Real-Time Image Processing*, vol. 9, no. 4, pp. 635–646, 2014.

[234] I. Charfi, J. Miteran, J. Dubois, M. Atri, and R. Tourki, "Definition and performance evaluation of a robust svm based fall detection solution," in *2012 eighth international conference on signal image technology and internet based systems*, pp. 218–224, IEEE, 2012.

[235] F. Wu, H. Zhao, Y. Zhao, and H. Zhong, "Development of a wearable-sensor-based fall detection system," *International journal of telemedicine and applications*, vol. 2015, 2015.

[236] S. Abdelhedi, R. Bourguiba, J. Mouine, and M. Baklouti, "Development of a two-threshold-based fall detection algorithm for elderly health monitoring," in *2016 IEEE Tenth International Conference on Research Challenges in Information Science (RCIS)*, pp. 1–5, IEEE, 2016.

[237] S. Palipana, D. Rojas, P. Agrawal, and D. Pesch, "Falldefi: Ubiquitous fall detection using commodity wi-fi devices," *Proceedings of the ACM on Interactive, Mobile, Wearable and Ubiquitous Technologies*, vol. 1, no. 4, pp. 1–25, 2018.

[238] Y. Tian, G.-H. Lee, H. He, C.-Y. Hsu, and D. Katabi, "Rf-based fall monitoring using convolutional neural networks," *Proceedings of the ACM on Interactive, Mobile, Wearable and Ubiquitous Technologies*, vol. 2, no. 3, pp. 1–24, 2018.

[239] A.-K. Seifert, M. G. Amin, and A. M. Zoubir, "New analysis of radar micro-doppler gait signatures for rehabilitation and assisted living," in *2017 IEEE International Conference on Acoustics, Speech and Signal Processing (ICASSP)*, pp. 4004–4008, IEEE, 2017.

[240] J. Bryan, J. Kwon, N. Lee, and Y. Kim, "Application of ultra-wide band radar for classification of human activities," *IET Radar, Sonar & Navigation*, vol. 6, no. 3, pp. 172–179, 2012.

[241] H. Sadreazami, M. Bolic, and S. Rajan, "On the use of ultra wideband radar and stacked lstm-rnn for at home fall detection," in *2018 IEEE Life Sciences Conference (LSC)*, pp. 255–258, IEEE, 2018.

[242] I. Nejadgholi, H. Sadreazami, S. Rajan, and M. Bolic, "Classification of doppler radar reflections as preprocessing for breathing rate monitoring," *IET Signal Processing*, vol. 13, no. 1, pp. 21–28, 2019.

[243] W.-C. Su, X.-X. Wu, T.-S. Horng, and M.-C. Tang, "Hybrid continuous-wave and self-injection-locking monopulse radar for posture and fall detection," *IEEE Transactions on Microwave Theory and Techniques*, vol. 70, no. 3, pp. 1686–1695, 2022.

[244] Q. Wu, Y. D. Zhang, W. Tao, and M. G. Amin, "Radar-based fall detection based on doppler time–frequency signatures for assisted living," *IET Radar, Sonar & Navigation*, vol. 9, no. 2, pp. 164–172, 2015.

[245] B. Jokanovic, M. Amin, and F. Ahmad, "Radar fall motion detection using deep learning," in *2016 IEEE radar conference (RadarConf)*, pp. 1–6, IEEE, 2016.

[246] M. Wang, Y. D. Zhang, and G. Cui, "Human motion recognition exploiting radar with stacked recurrent neural network," *Digital Signal Processing*, vol. 87, pp. 125–131, 2019.

[247] R. G. Guendel, F. Fioranelli, and A. Yarovoy, "Distributed radar fusion and recurrent networks for classification of continuous human activities," *IET Radar, Sonar & Navigation*, 2022.

[248] Z. Li, J. Le Kernec, F. Fioranelli, O. Romain, L. Zhang, and S. Yang, "An lstm approach to short-range personnel recognition using radar signals," in *2021 IEEE Radar Conference (RadarConf21)*, pp. 1–6, 2021.

[249] J. J. Heckman, "Sample selection bias as a specification error," *Econometrica: Journal of the econometric society*, pp. 153–161, 1979.

[250] M. I. Skolnik, *Radar handbook*. McGraw-Hill Education, 2008.

[251] M. Ash, M. Ritchie, and K. Chetty, "On the application of digital moving target indication techniques to short-range fmcw radar data," *IEEE Sensors Journal*, vol. 18, no. 10, pp. 4167–4175, 2018.